Araneiform terrain on Mars — spatial configuration and mechanism of formation

Araneiformes Gelände auf dem Mars — Räumliche Konfiguration und Bildungsmechanismen

Dissertation zur Erlangung des Grades
einer Doktorin der Naturwissenschaften

vorgelegt von

Jingyan Hao

Im Fachbereich Geowissenschaften
der Freie Universität Berlin

Berlin, 2020

The supervisor:	Prof. Dr. Ralf Jaumann Freie Universität Berlin Institute of Geological Sciences Planetary Sciences and Remote Sensing
The second examiner:	Prof. Dr. Frank Postberg Freie Universität Berlin Institute of Geological Sciences Planetary Sciences and Remote Sensing
Date of defense:	May 26, 2020

Acknowledgment

I sincerely thank my supervisor, Prof. Dr. Ralf Jaumann. Whatever difficulties and problems I meet, he always has nice ideas to sort out. He supported me in having German courses and has brought me support from Deutsches Zentrum für Luft–und Raumfahrt (DLR), I enjoy time here. Prof. Jaumann is always ready to offer help and answer questions, not limited to scientific ones, but whatever I ask. Without his consistent support, guidance, patience, motivation, scientific mind, and broad knowledge, I would not have been able to complete this research and have made it through my Ph.D. degree. Prof. Jaumann, Vielen Dank! I am deeply grateful for all of your help and support and feel so fortunate to have you as my supervisor.

One critical support from Prof. Jaumann is that he introduced Dr. Solmaz Adeli as my co-supervisor. I do not recall how many times I knocked her office door and asked for help. Countless time was used for discussion for papers, this thesis, each conference abstracts, posters, oral preparation and slides, funding applications, emails, response letters, etc. She reviews and comments these word by word and sentence by sentence. She teaches me how to do scientific writing and is so kind often spending hours to show me paper writing skills, e.g., why this sentence should be written like this, why this term is not proper, and how to respond to reviewers. Whatever problems, she always tries to help me out. Most importantly, her help is in not only research but also so many aspects. When I worked in DLR, she brings me to the "lunch group" and introduces colleagues to me, trying to help me "integrating" into here. She even knows where to acquire a Führungszeugnis without an appointment. Pages would not be enough to describe her superb supervision and help. I could not have imagined having a better supervisor and mentor. Thank you so much, Solmaz, از شما بسیار سپاسگزارم، سولماز!

I express my sincere gratitude to Dr. Gregory Michael, the other co-supervisor; I have been very fortunate to be doing my research with him. I sincerely thank his contributions to spatial randomness analysis and the model in my research. I greatly appreciate all abundant hours of discussions of scientific issues, reviewing of English writings, feedbacks of manuscripts, science advice, and everything. As a nice friend, he is always willing to help. My sincere thank also goes to Adrianna, Theresa, and Lisa. Thank you very much for all the wonderful moments we had together.

I express a thousand times thanks to Prof. Dr. Stephan van Gassselt. Without you, I could not have been in Germany and had the opportunity to study spiders. Stephan initiated my PhD research and led me to the gorgeous south pole of Mars, and suggested exotic spiders as my research topics. I sincerely

appreciate all of your help and support and had been so lucky to be your student and have you as my supervisor.

I sincerely thank Prof. Dr. Frank Postberg, who kindly accepted to be my second thesis reviewer. He has given valuable comments and suggestions to my work. I am very grateful to his excellent support, advice, and help during my study and work at Freie Universität Berlin (FUB).

I am also very thankful to Dr. Julia Lanz–Kröchert for her valuable discussions for the draft of my first paper. Especially, I am very grateful for her support of my participation in the 6th International Conference on Mars Polar Science and Exploration in Iceland.

I sincerely thank Prof. Dr. Lena Noack. She kindly accepted to be the committee member and the chair of my PhD defense. Everybody knows how challenging to organize a defense during this coronavirus pandemic, but she managed very well and did a wonderful job; she thought of and took care of many details and let me have a wonderful and memorable defense! Thank you, Lena. I also show thank to Prof. Dr. Kai Wuennemann. Thank you for being one committee member of my PhD defense and attended my defense with your crutch.

A big thank to Wilhelm Zuschneid and Anna. Their help is on almost every kind, e.g., helping to move, visiting a doctor, free German translation, and Germany culture, shopping. Wilhelm and Anna are the "encyclopedia" of Germany life to me. Wilhelm contributed to the permeability in my work, and often shares his broad geology knowledge with me. The German version of this thesis's abstract also includes Wilhelm's enormous contributions. I am lucky to share the same office with you, Wilhelm and Anna!

I show my warm thank to Dr. Christoph Gross and Dr. Muna Al–Samir for their help. I love the plant from you as my birthday present. I really appreciate the time we spent together in the office 223. Especially, to Christoph, thank you so much for being my reviewer and the committee member of my PhD defense.

I thank very much to Alicia Neesemann at FUB. She helps how to better process images and gives valuable comments on geology in my work. She often helped correct my German language homework. Thank you, Alicia.

Another thank is to Björn. As an expert in HRSC data, he contributes to Figure 1.8. Björn is the "encyclopedia" of food, often introduces good ones to me. He often teaches me how to pronounce German words better. Thank you, Björn.

I sincerely thank very much to Sebastian, he often helps slove problems for my computer both in software and hardware. I love his humor which makes me not only lauging but also improves my English humor sense. At the final working of FUB, I worked together with him, I hope he already forgets my delay. :)

A warm thank you also goes to Carolin Rabethge, especially for her suggestions on my funding application. Vielen Dank, Carolin.

A special thank you to the team of coordinators, Stefanie, Heike, and Dr. Stefanie Mikulla, for their support during my PhD study at FUB.

Here, I would like to especially thank those who contributed to my PhD hat, Sebastian, Wilhelm, tiantian, Christoph, Solmaz, etc., I really love this hat, these spiders and X83 bus and “Lost and Found” touched my heart! Thank you!!!

My sincere gratitude goes out to all current and former colleagues at Freie Universität Berlin, Jon, Zenghui, Fabian, Simon, Nozair, etc., especially to ones at Planetary Sciences and Remote Sensing team, Dr. Nico Schmedemann, Dr. Thomas Kneissl, Csilla, Christian, Tilmann, Dominik, Alexander, Dr. Patrick McGuire, etc. I will miss our Ping–Pong playing.

Tian is my best friend in Germany. All I can say is thank you, and thanks for being my friend. With her accompany, I have more happy times.

I also thank Prof Jan-Peter Muller as well as his team, e.g., Yu Tao and Kiki at University College London. They kindly provide CTX DTMs used in this thesis.

I have appreciated the fruitful collaboration with Ernst Hauber at DLR. His valuable and constructive comments and discussions significantly improve my PhD research, especially the second paper. He also kindly granted me the access to CaSSIS data which results in one critical chapter of my PhD thesis. Danke schön, Ernst.

I thank Dr. Ganna Portyankina at the University of Colorado at Boulder. She is a leading scientist in spider researches and has published many outstanding papers which have given me many inspirations. She contributed to my second paper which has thus been improved significantly. During several conferences, she gave valuable comments on my work. Ganna, Велике спасибі!

My sincere thanks also go to Cedric Millot at Claude Bernard University, especially for his contributions to the insolation calculation in this thesis and my second paper. He shared and discussed the details of his work which had not been published yet, to help improve my work. Merci beaucoup, Cedric.

I sincerely express my thanks to Dr. Stefan Schroeder at DLR for his help and advice, especially the constructive comments for my second paper. I enjoy being his neighbor at DLR. Dank je wel, Stefan.

I am also deeply grateful to Dr. Adrian Brown at NASA. He helped me with the research about water ice at the north pole of Mars. He shared his research experiences which have strong influences on my research career.

My special warm and sincere thanks go to Dr. Lauren McKeown. We met at one conference, and she shared her experiences which inspired me a lot and helped me out at a hard moment. All of the words I can say are "condensed" into Lauren, thank you so much!

I also thank colleagues in DLR, Ernst Hauber, Linda, Claudia Hauschid, Daniela Tirsch, Dr. Franziska Schulzeck, Dr. Martin Volker, Indhu Varatharajan, Katharina Otto, Hugo Hellard, Ana–Catalina Plesa, Jeremy Brossier, Dr. Manuel Sachse, etc., lucky to have met you in my PhD life.

How can I not thank my excellent supervisor Prof. Dr. Di and all my colleagues and friends at ‘Planetary Mapping and Remote Sensing’. Here is the starting point of my career as a planetary scientist, Prof. Dr. leads me to the planetary sciences and the amazing Mars. Those times we spent together will be always in my heart and I miss them.

I express my sincere gratitude to my wondeful supervisor Prof. Dr. Ma at ‘Remote Sensing and Geo-information Science’. With his supervision, I started to aim to be a scientist. My thanks to all my friends and colleagues in the team, especially Prof. Ma: with you, I shared unforgettable moments. I appreciate those days we spent together and they are one of my best memories!

Last but not least, I am very thankful to all my friends, especially my family. This thesis would not have been possible without your warm love, continued patience, and endless support.

Berlin

October 5, 2020

Contents

List of Figures

List of Tables

List of Abbreviations

CTX: Context Camera
CaSSIS: Colour and Stereo Surface Imaging System
DTM: Digital Terrain Model
GRS: Gamma–Ray Spectrometer
HEND: High Energy Neutron Detector
HiRISE: High Resolution Imaging Science Experiment
HRSC: High Resolution Stereo Camera
Ls: Solar Longitude
M2CND: Mean 2nd–Closest Neighbor Distance
MEx: Mars Express
MOC: Mars Orbiter Camera
MOLA: Mars Orbiter Laser Altimeter
MONS: Mars Odyssey Neutron Spectrometer
MRO: Mars Reconnaissance Orbiter
MGS: Mars Global Surveyor
MY: Mars Year
NPRC: North Polar Residual Cap
S (N) PLD: South (North) polar layered deposits
SPRC: South Residual CO_2 Polar Cap
SHARAD: Shallow Subsurface Radar
RSL: Recurring Slope Lineae
TES: Thermal Emission Spectrometer
THEMIS: Thermal Emission Imaging System
TI: Thermal Inertia
TGO: Trace Gas Orbiter
WEH: Equivalent Hydrogen Abundance

Abstract

The focus of this thesis is the investigation of the spatial configuration and formation mechanisms of a type of terrain known as araneiform terrain or "spiders" found in the south polar regions of Mars. Seasonal sublimation and condensation of CO_2 at the poles are an essential part of cycles of global volatiles (CO_2 and H_2O) and dust, e.g., up to 25% of the Martian atmosphere's CO_2 interacts annually with the polar surfaces. The seasonal CO_2 ice condenses on the poles of Mars each autumn/winter; it can form translucent slab ice which is transparent in the visible light and opaque in the infrared. This physical property allows basal sublimation of the seasonal CO_2 ice under insolation in spring. The resulting CO_2 accumulation and jetting leads to transitional features such as dark spots/fans and radial or dendritic troughs known as araneiform terrain (“spiders”). Thus, spider formation is linked to the global CO_2 cycle and the seasonal evolution of the Martian poles which are sensitive to the Mars climate. It is one of the most active current erosive processes on Mars which involves mobilization of material jetted from the substrate relocating a greater mass of dust than either dust storms or the cumulative effect of dust devils.

Observations at seven study regions in this work reveal diverse morphologies of spider forms, which suggest variability of araneiform formation processes. Based on my observations, a spider formation model is developed to explain the formation of spiders and their growth processes. I consider the migration of pressurized CO_2 through the porous substrate towards cracks in the overlying CO_2 ice layer, and the effect of the substrate's cohesive strength on the development of spider troughs. Thus, substrate properties (permeability, porosity, and cohesion) are significant parameters controlling the mechanism of spider growth. The major advantage of this model is that it explains the mechanism of the growth of central pits and radiating troughs, and parameters (e.g., trough length) of their morphologies, which have not been considered before. This model suggests that spider troughs are created from the developments of random protrusions of initial degradational forms. My trough orientation mappings and constructed rose diagrams are consistent with this theory showing that spider troughs do not have preferred orientations and appear randomly distributed. Due to rate differences between local pressure accumulation and lateral gas migration, the model reveals an inhibited zone existing around a newly formed spider that diminishes pressure accumulation preventing another CO_2 jet. This suggests the spatial distributions of spiders to be non–random. Spatial randomness analysis of the seven spider populations confirms this non–randomness and indicates a strong regional variation of spider average spacings. Regional differences in substrate properties (permeability, porosity, and cohesion) are the likely causes of the regional

variation. Other parameters, such as seasonal CO_2 ice thickness and grain size, local climate, obliquity, and latitude, also influence spider formation and spatial configurations.

This research improves the understanding of how CO_2 jetting and subsequent spider formation shaped and modified the south polar surface of Mars which may actively occur at the present time, and how volatiles (CO_2 and water) and dust play their roles in the polar processes and Mars global circulation. Furthermore, it provides insight into the recent climate conditions of Mars.

Zusammenfassung

Der Schwerpunkt dieser Arbeit liegt auf der Untersuchung der räumlichen Konfiguration und des Bildungsmechanismus eines polaren Geländetyps, der als araneiformes Gelände oder "Spinnen" am Südpol des Mars bekannt ist. Saisonale Sublimation und Kondensation von CO_2 an den Polen sind ein wesentlicher Bestandteil der globalen Zyklen von Volatilen (CO_2 und H_2O) und Staub, z. B. interagieren bis zu 25% des CO_2 der Marsatmosphäre jährlich mit den polaren Oberflächen des Mars. Das saisonale CO_2-Eis kondensiert jeden Herbst/Winter an den Polen des Mars. Es kann in Form von durchscheinendem Eisplatten vorliegen, die im sichtbaren Licht transparent und im Infrarot undurchsichtig sind. Diese physikalische Eigenschaft ermöglicht eine Sublimation des saisonalen CO_2-Eises an der Basis unter Sonneneinstrahlung in Quellen. Das dadurch verursachte Herausschießen von CO_2 führt zur Bildung vergänglicher Geländemerkmale wie dunklen Flecken / Fächern und radialen oder dendritischen Tälern, die als araneiformes Gelände (“Spinnen“) bekannt sind. Somit ist die Spinnenbildung mit dem globalen CO_2-Kreislauf und der saisonalen Entwicklung der Mars-Pole gekoppelt. Beide Prozesssysteme sind für das Mars-Klima empfindlich. Die Bildung von araineiformen Gelände ist einer der derzeit aktivsten erosiven Prozesse auf dem Mars, bei dem Material mobilisiert wird, welches aus dem Substrat ausgestoßen wird und so eine größere Staubmasse als Staubstürme oder die kumulative Wirkung von Staubteufeln verlagert.

In dieser Arbeit zeigen Beobachtungen in sieben Untersuchungsregionen verschiedene Morphologien von Araneiformen, die auf die Variabilität der Bildungsprozesse hindeuten. Basierend auf meinen Beobachtungen wird ein Modell zur Bildung von Spinnen entwickelt, um die Spinnenbildung und ihre Wachstumsprozesse zu erklären. Ich betrachte die Migration von unter Druck stehendem CO_2 durch das poröse Substrat zu Rissen in der darüber liegenden CO_2-Eisschicht und den Einfluss der Kohäsion des Substrats auf die Entwicklung von Spinnen-Hohlformen. Dabei sind Substrateigenschaften (Permeabilität, Porosität und Kohäsion) wichtige Parameter, die den Mechanismus des Spinnenwachstums steuern. Der Hauptvorteil dieses Modells besteht darin, dass es sowohl den Mechanismus des Wachstums von zentralen Trögen und davon radialen Rinnen als auch Parameter (z. B. Troglänge) ihrer Morphologie erklärt, die zuvor nicht berücksichtigt wurden. Dieses Modell legt nahe, dass sich die radialen Spinnentröge aus zufälligen Vorsprüngen anfänglicher Erosionsformen entwickeln. Meine Kartierung der Orientierung der einzelnen Rinnen und die konstruierten Rosendiagramme stimmen mit dieser Theorie überein und zeigen, dass Spinnentröge keine bevorzugten Orientierungen haben und zufällig verteilt erscheinen. Aufgrund von Geschwindigkeitsunterschieden zwischen lokaler Druckakkumulation und

lateraler Gasmigration zeigt das Modell eine verbotene Zone um eine neu gebildete Spinne, die die Druckakkumulation verringert und die Ausbildung eines weiteren CO_2-Strahls verhindert. Dies legt nahe, dass die räumlichen Verteilungen von Spinnen nicht zufällig sind. Die räumliche Zufallsanalyse der sieben Spinnenpopulationen bestätigt diese Nicht-Zufälligkeit und zeigt eine starke regionale Variation der durchschnittlichen Abstände der Araneiformen. Regionale Unterschiede in den Substrateigenschaften (Permeabilität, Porosität und Kohäsion) sind die wahrscheinlichen Ursachen für diese regionale Variation. Andere Parameter wie die Dicke des saisonalen CO_2-Eises und seine Korngröße, das lokale Klima, die Neigung und der Breitengrad beeinflussen ebenfalls die Bildung von Spinnen und die ihre räumlichen Konfigurationen.

Diese Forschung verbessert das Verständnis dafür, wie CO_2-Jets sowie die durch sie verursachte Spinnenbildung als derzeit aktiv auftretende Prozesse die Marsoberfläche im Bereich des Südpols geformt und modifiziert haben, und wie flüchtige Stoffe (CO_2 und Wasser) und Staub ihre Rolle bei den polaren Prozessen spielen und Mars globale Verbreitung. Darüber hinaus ermöglicht sie Einblicke in die rezenten Klimabedingungen des Mars.

Chapter I. Introduction

1.1 The scientific background

1.1.1 The Martian volatiles and their global cycles

Volatiles such as carbon dioxide (CO_2) and water (H_2O), along with dust, form three cycles that control the Mars climate (Smith, 2002). These cycles affect global energy balance and properties of the polar area. The Mars atmosphere is composed primarily of CO_2 (~96% by volume) (Leighton and Murray, 1966; Owen et al., 1977; Jakosky and Phillips, 2001; Mahaffy et al., 2013), thus the CO_2 cycle plays the dominant role in the Mars climate while H_2O and dust as well have effects despite their small quantity (Leighton and Murray, 1996; Owen et al., 1997; Jakosky and Phillips, 2001; Smith, 2002; Mahaffy et al., 2013). Martian volatiles and their exchanges are encompassed by various research fields (Figure 1.1). In this introduction, I focus on CO_2 and H_2O–which are stored in the atmosphere and surface/subsurface of Mars. Both CO_2 and H_2O are suggested to be essential geomorphic and geological agents and involved in formation of various phenomena from equatorial, low to middle latitudes to the polar area, e.g., recurring slope lineae (RSL) (McEwen et al., 2011; 2014; Ojha et al., 2015), slope streaks (Ferris et al., 2002; Miyamoto et al., 2004; Kreslavsky and Head, 2009; Bhardwaj et al., 2019a), gullies (Malin and Edgett, 2000), pitted rock surfaces (Head et al., 2011), dark spots/fans (Kieffer, 2000; Piqueux et al., 2003), and spiders (Kieffer, 2000; Piqueux et al., 2003; Hansen et al., 2010; Portyankina et al., 2017; Hao et al., 2019; 2020).

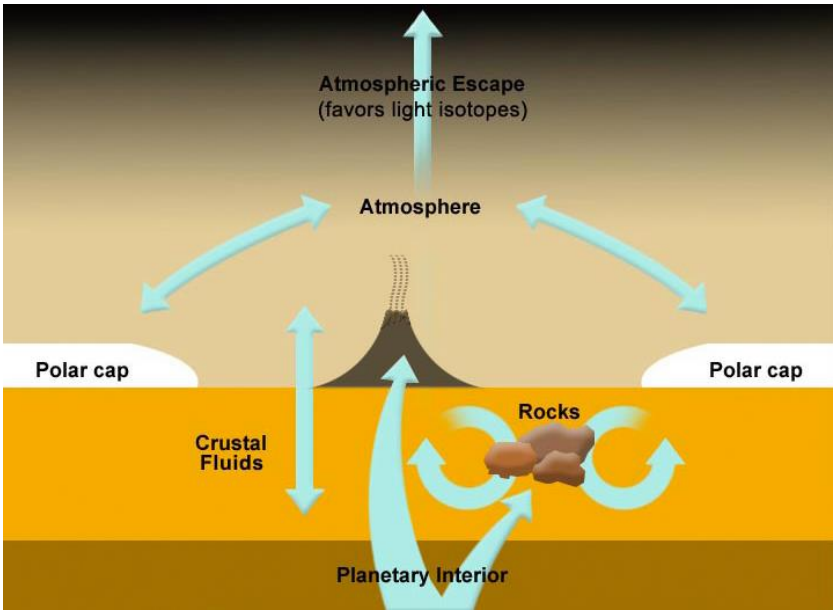

Figure 1.1 Volatiles on Mars: simplified reservoirs and interactions (Credit: NASA).

a. H_2O

Searching for water has motivated Mars science and exploration for decades. Water has an essential role in the Martian climatic and geological history. Various Martian geomorphological features have been suggested to be linked to liquid water, e.g., gullies (Malin et al., 2006) and slope streaks (Ferris et al., 2002; Kreslavsky and Head, 2009).

At the present Mars, water exists largely as ice due to low atmospheric temperature and pressure. Water is also present in hydrated minerals, potential liquid brines, ice clouds, and in the form of vapor in the atmosphere (Spinrad et al., 1963; Jakosky and Haberle, 1992; Carr, 1996; Martín–Torres et al., 2015; Ojha et al., 2015). Liquid surface water possibly exists very briefly in equatorial areas due to local warmth with temperatures above the water melting point: it, however, evaporates immediately and refreezes at the colder polar area later (Brass et al., 1980; Jakosky and Haberle, 1992; Haberle et al., 2001; Hecht, 2002; Bhardwaj et al., 2019b).

Martian water resides both in the atmosphere (Mellon et al., 1993; Carr, 1996; Bibring et al., 2004), the surface, and subsurface (Boynton et al., 2002; Mitrofanov et al., 2002; Tokar et al., 2002; Feldman et al., 2004). Compared with the minor water vapor content in the atmosphere (210 ppm by volume; Smith, 2002), the surface and subsurface water at the two poles are the major water reservoirs (Figure 1.2). The north polar residual ice cap (NPRC) consists of water ice (Kieffer et al., 1976; Kieffer and Titus, 2001; Langevin et al., 2005) and is the major location where water ice is visible (Carr, 1966). Other visible water ice contains seasonal surface water frost formed from atmospheric deposition (Brown et al., 2010; Carr and Head, 2015) and water ice on the mantled terrains surrounding the south polar area (Titus et al., 2003; Piqueux et al., 2008). In contrast, the south polar residual ice cap (SPRC) is composed of ~ 8 m thick CO_2 ice. Both NPRC and SPRC survive the southern summer and the whole Mars year, thus are named "residual" (Nye et al., 2000; Thomas et al., 2000; Titus et al., 2003; Byrne and Ingersoll, 2003; Bibring et al., 2004). In much of the literatures, "permanent", "residual" and "perennial" are interchangeably used to refer to the abovementioned water ice or CO_2 ice or their combination. Hereafter, this thesis uses "residual" to refer to the polar caps which remain through summer: it refers to predominantly water ice at the north pole and CO_2 ice at the south pole.

Polar layered deposits (PLD), which occur at both poles, are another inventories for water ice. They are ~2–3 km thick and in the form of layers with varying ratios of water ice and dust (Figure 1.3; Jakosky and Haberle, 1992; Carr, 1996; Bibring et al., 2004). Although exact ratios are poorly constrained, water ice is thought dominant from radar measurements (Picardi et al., 2005; Plaut et al., 2007). This layering structure is thought to be formed due to

variations of Martian astronomical parameters, e.g., obliquity and perihelion, and record climate history (Cutts et al., 1973; Murray et al., 1972; 1973; Cutts et al., 1973; Toon et al., 1980; Cutts and Lewis, 1982; Howard et al.,1982; Thomas et al., 1992; Malin et al., 2001; Laskar et al., 2002; Tanaka et al., 2007; Levrard et al., 2007; Hvidberg et al., 2012). SPLD (~400 km in diameter) and NPLD (~1100 in diameter) (Clifford et al., 2000) are overlain or "capped" by SPLC with a small portion and NPLC largely respectively (Figure 1.4 and 1.5), thus the two residual ice deposits are referred to as "caps".

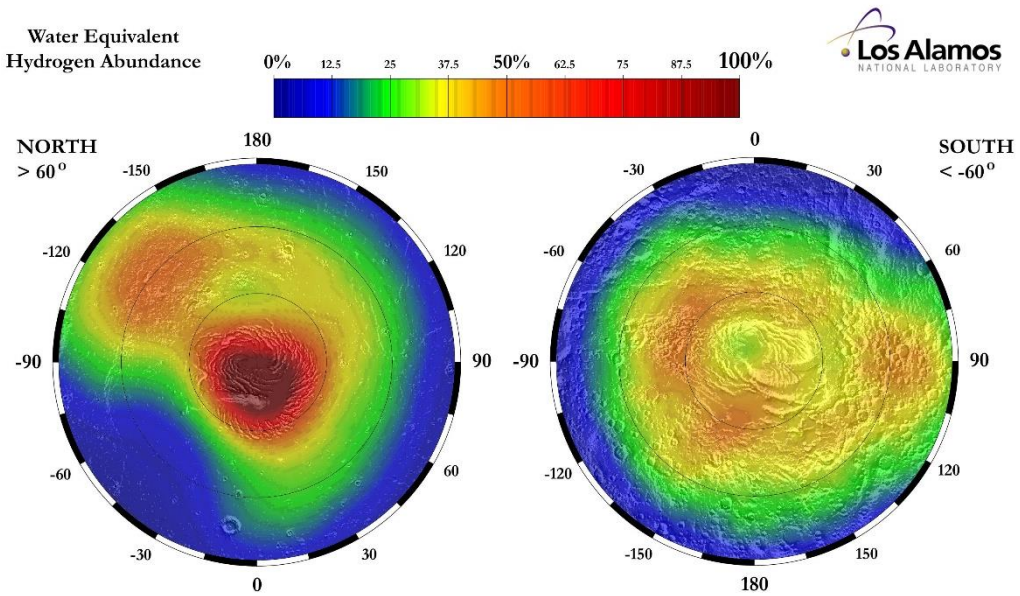

Figure 1.2 Water equivalent hydrogen abundance overlain a shaded relief map of Mars Orbiter Laser Altimeter (MOLA; Smith, 2001a) (Credit: Feldman, W. C., Prettyman, T. H., Maurice, S., et al., Los Alamos National Laboratory/JPL). Water presented in mass percent Wt.% were produced from neutron measurement using the Neutron Spectrometer onboard Mars Odyssey between 02.2002 and 04.2003 (Feldman et al., 2003). Note that due to the ambiguity of neutron measurements (Feldman et a., 2002), water equivalent hydrogen, a proxy of water ice, could also indicate hydrated minerals.

It is estimated that water ice from the two poles could, if melted, cover the entire surface of Mars with ~30 m depth (Carr, 1986; Smith et al., 1999) while the deposition from the atmosphere can only cover with ~10^{-5} m (Jakosky and Farmer, 1982). Recent radar observations indicate: liquid brine water may be trapped below the south polar layered deposits (SPLD) at relatively shallow depths (~1.5 km) with ~20 km across (Orosei et al., 2018); the mixture of water ice and soil (water ice fraction of 62–88% by volume) is possibly located beneath the north polar layered deposits (NPLD) (Nerozzi and Holt, 2019).

Mars scientists often use the terms "soil," "regolith," and "dust". "soil" is a terrestrial term to describe "the material on the surface of the ground in which plants grow" (*Cambridge Dictionary, dictionary.cambridge.org/us/*) which

emphasizes biological activity (Barlow, 2008), planetary researchers borrowed "regolith" from "soil" to refer to material generated mostly from impact or weathering processes (Barlow, 2008; Greeley, 2013). The two terms are often used interchangeably in planetary publications. In this thesis, I apply "soil" and "regolith" interchangeably to unconsolidated material distinguished from rocks. "dust" in the *International Standardization Organization (1994)* and *Glossary of Atmospheric Chemistry Terms (1990)* has strict particle size requirement from 1–100 μm in diameter. However, no precise measurement of particle sizes is available for the material of the substrate on Mars; only its thermal inertial provides a range of 50–200 μm as mentioned above. Thus, publications of Mars science often use "sand and dust" or "dust" to refer generally to the material with small particles which may settle slowly under gravity (*Glossary of Atmospheric Chemistry Terms, 1990*).

The depth of subsurface water ice at the poles is suggested possibly at centimeters (Mitrofanov et al., 2004; Mitrofanov et al., 2002; Demidov et al., 2015). The Phoenix lander exposed subsurface ice which sublimated soon after it was exposed to the atmosphere (Arvidson et al., 2010). At middle/low latitudes, the subsurface water ice is in greater depths and sometimes are exposed at cliff faces (Mellon et al., 1993; Bandfield, 2007; Dundas et al., 2018).

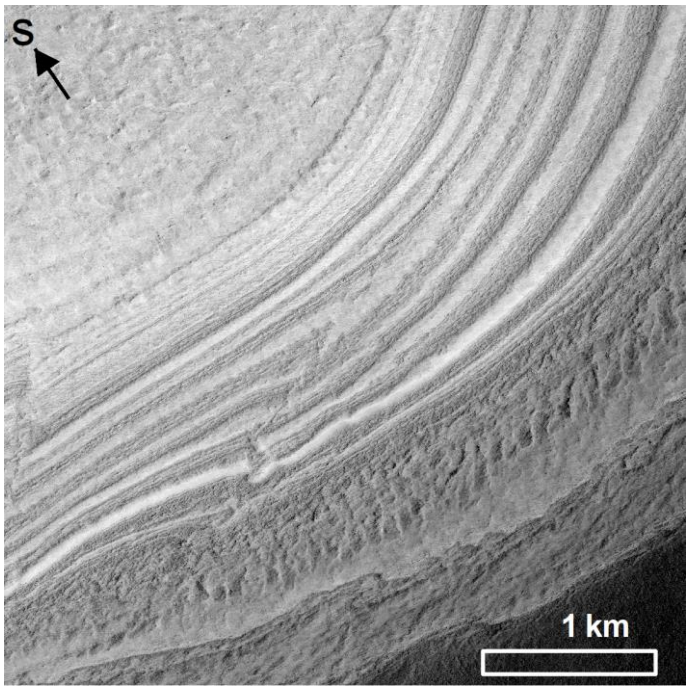

Figure 1.3 One area (centered at ~72.9°S, ~146.4°E) of the south polar layered deposits (SPLD). The image is HiRISE PSP_005194_1070 (McEwen et al., 2007). SPLD exhibits layers mixed with dust and water which were deposited during climate cycles.

Water in the atmosphere (water vapor) exchanges with the subsurface and surface (especially at the poles) annually and over longer timescales (e.g.,

obliquity driven), although the processes of this cycle are still in debate. Water ice in the north polar residual cap is exposed from the late spring after the top layer of seasonal CO_2 ice sublimates away (Haberle and Jakosky, 1990); therefore, the water there partially sublimates in spring/summer and deposits back in autumn/winter (Richardson and Wilson 2002; Hvidberg and Zwally, 2003; Montmessin et al. 2004). Thus, the north pole is suggested as the major

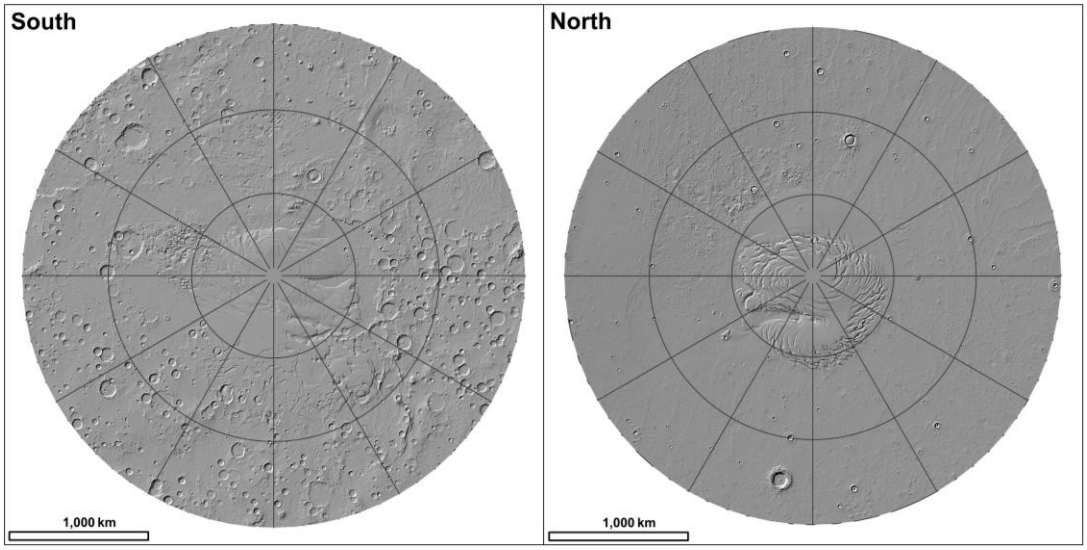

Figure 1.4 Mars poles seen from MOLA hillshade with 463 m/pix (Smith et al., 2001b), projected with Mars South/North Polar Stereographic. Intervals of latitude and longitude are 10° and 30 °.

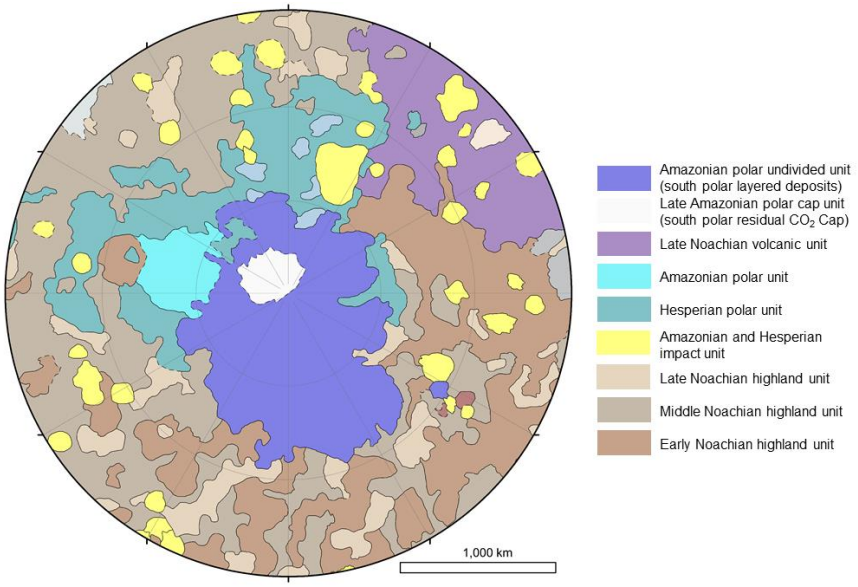

Figure 1.5 Geologic map of the south pole of Mars (Tanaka et al., 2014) projected with Mars South Polar Stereographic. Intervals of lines of latitude and longitude are 10° and 30°.

source of water vapor for the atmosphere which is transported to low latitudes and equatorial area at the end of summer (Farmer et al., 1976; Haberle and

Jakosky, 1990). At the present Mars, the south polar residual CO_2 ice cap serves as a cold trap for water, so that water is possibly transported from the north to the south pole (Jakosky and Farmer, 1982; Jakosky and Haberle, 1992; Houben et al., 1997; Kreslavsky and Head, 2002; Richardson and Wilson, 2002; Head et al., 2003; Madeleine et al., 2009; Pottier et al., 2017). A new study utilizing numerical simulations indicates a possible water cycle within the atmosphere: water vapor moves from the lower to upper atmosphere. This water cycle occurs each Mars year only at southern high latitudes ≥ 60°S (Shaposhnikov et al., 2019).

Knowledge of water inventories and the cycling processes across Mars is essential for understanding the current Mars climate and its history, which holds the key to the understanding of the evolution of Mars itself, e.g., how did Mars evolve from past wet to current dry conditions with CO_2 as its major atmosphere component? Information on the distribution of H_2O is also of enormous value to future human missions.

b. CO_2

CO_2 cannot exist as liquid on the surface; its phase transition occurs directly from the solid to the gas phase (sublimation) and vice versa (deposition) everywhere on the Martian surface. From poles to low latitudes, recent publications indicate that more processes likely involve CO_2 which increasingly becomes the alternative essential geomorphological agent to water. Typical examples are gullies and linear gullies which have been seen as evidence of liquid water (Malin and Edgett, 2000; Mangold et al., 2002), but an alternative formation mechanism was proposed to be linked to CO_2 ice (Diniega et al., 2013; Pilorget and Forget, 2015).

One major CO_2 reservoir on Mars is the south polar residual ice cap (SPRC). It may be not stagnant, sublimating in some places and accumulating in others (Thomas et al., 2013; 2016; Becerra et al., 2015). Radar observations suggest that several CO_2 ice inventories are possibly buried within the south polar layered deposits (Phillips et al., 2011; Bierson et al., 2016). It is estimated that the surface pressure would be increased by 65–85% (400 to 500 Pa) if this deposit sublimed (Phillips et al., 2011). This buried CO_2 is separated into three distinct layers by thinner (10–60 m) water ice bounding layers (Figure 1.6) which likely result from cycling obliquity or eccentricity (Bierson et al., 2016).

In addition to the abovementioned perennial CO_2, seasonal CO_2 ice occurs each winter from both poles to mid–latitudes. They are up to 2.5 m thick (Smith, 2001a; Aharonson et al., 2004) and are thought to thin away from the poles (Kieffer et al., 2000; Kieffer and Titus, 2001; Carr, 2006; Langevin et al., 2007; Titus et al., 2008). The seasonal CO_2 ice sublimates in spring/summer into the atmosphere and condenses back at autumn/winter, their spatial extent, thickness, and mass, exhibit seasonal variations (Giuranna et al., 2007; 2008;

Piqueux et al., 2015; Calvin et al., 2017). Up to 25% in mass of the atmosphere is involved in this annual CO_2 cycling, which drives climate and atmosphere circulation (Leighton and Murray, 1966; Hess et al., 1979; James et al., 1992; Tillman et al., 1993; Kelly et al., 2006). Under the current obliquity ~25°, the seasonal CO_2 ice can extend to ~45°S and ~55°N (Carr, 2006; Langevin et al., 2007; Schmidt et al., 2009; Brown et al., 2010; 2012; Appéré et al., 2011; Piqueux et al., 2015) which will be even lower at higher obliquities (Head et al., 2003; Madeleine et al., 2009).

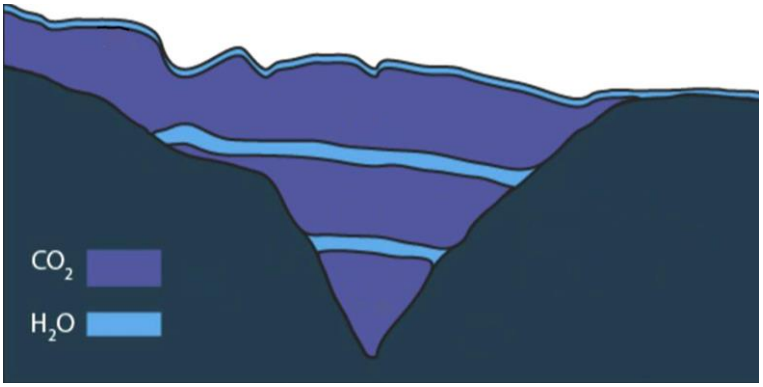

Figure 1.6 A cartoon profile of buried CO_2 ice separated by the radar–detected bounding water ice layer (adapted from Figure 4 in Bierson et al. 2016).

At low latitudes, CO_2 ice is suggested to occur possibly at high elevations, such as Olympus Mons (Piqueux et al., 2016), or locally, e.g., on and near the pole–facing crater walls at ~24 and 33°S reported by Schorghofer and Edgett (2006). Part of CO_2 ice at low latitudes possibly undergoes a diurnal cycle, i.e., sublimates away after sunset and condenses back in the night (Piqueux et a., 2016). This recurring sublimation and condensation of CO_2 may lead to higher porosity of substrate and yield a large surface reservoir of dust which can be mobilized and lifted into the atmosphere (Piqueux et al., 2016). Due to its low mass transport, this diurnal cycle may have little influence on the local/global pressure cycle, but may have a role in formation of some phenomena observed in these regions, e.g., slope streaks (Piqueux et al., 2016).

1.1.2. Physical properties of seasonal CO_2 ice on Mars

a. Translucency

Under current Mars conditions, the seasonal CO_2 ice is formed by condensation at the surface (frost) and in the atmosphere (snow; also termed as precipitation) (Forget et al., 1998; Wood, 1999; Titus et al., 2001; Ivanov and Muhleman, 2001). The relative proportions are uncertain. One publication suggested that snowfall may contribute 3%–20% by mass to the seasonal CO_2 deposits in latitudes between 70 and 90°S (Hayne et al., 2014).

Both depositions, i.e., snow and frost, can undergo rapid annealing which involves a microphysical process, i.e., pressureless sintering, to form translucent CO_2 ice (Clark et al., 1983; Kieffer, 1990 and 2007; Eluszkiewicz,

1993; Colbeck, 1997; Kieffer et al., 2000; 2007; Langevin et al., 2007). Researchers suggested the term "slab ice" to refer to "large–grained" (Kieffer, 2000; Langevin et al., 2007). Since the atmosphere is dusty, the seasonal CO_2 slab ice likely includes atmospheric dust grains during condensation (Kieffer, 2007). The dust concentration remains unclear; spectral observations have yielded an estimate that the content may be from 0 to 7 wt.% (in mass percent) in the surface CO_2 ice (Langevin et al., 2006; Kieffer, 2007). Possible mechanisms for self–cleaning have been proposed (Langevin et al., 2006; Kieffer et al., 2006; Kieffer, 2007; Portyankina et al., 2010): in spring, dust grains absorb most of solar energy since pure CO_2 ice is transparent to visible wavelength (Hansen, 1997; 1999); gas "pockets" are then formed surrounding dust grains which will burrow downward to the ground or be released through the upper ice surface, CO_2 slab ice thus becomes very clean (Portyankina et al., 2010; Kieffer, 2007).

Alternatively, the deposition from the atmosphere can directly form clean translucent CO_2 slab ice when no dust is in the atmosphere as indicated by laboratory measurements and spectral observations (Langevin et al., 2006; Portyankina et al., 2018), thus annealing and self–cleaning may not be necessary (Langevin et al., 2006; Portyankina et al., 2018).

b. Basal sublimation

The translucency of the seasonal CO_2 slab ice allows it to be transparent in visible light and opaque to the thermal infrared spectrum (Hansen, 1997 and 2005; Langevin et al., 2007; Portyankina et al., 2018; Andrieu et al., 2018). Thus, sunlight penetrates the CO_2 slab ice and directly heats the underlying substrate, triggering the sublimation of the base of the CO_2 ice (Kieffer, 2000; 2007). Thermal modelling confirms that basal sublimation occurs when the overlying CO_2 ice is in the form of large–grained translucent slab ice (Pilorget et al., 2011), e.g., a ~0.6 m thick CO_2 ice allows solar flux to pass through and reach the substrate when the grain size is larger than 1 mm, the substrate will be heated resulting in sublimation of the bottom part of the CO_2 ice. In the case of small–grained CO_2 ice, sublimation occurs at the ice surface (Pilorget et al., 2011).

c. Cryptic area

Observations of the Thermal Emission Spectrometer (TES; Christensen et al., 2001) indicate that one area at the south pole (for its location, please refer to the Figure 1 in Hansen et al., (2010) which is presented in this chapter as Figure 1.7) retains low surface temperature under low albedo during spring time (Paige and Keegan, 1995; Kieffer et al., 2000; 2006; Brown et al., 2010; Colaprete et al., 2005). This contradiction of low albedo and low temperature is termed as "cryptic behavior" (Piqueux et al., 2003) which is due to the translucent CO_2 slab ice covering this area (Kieffer, 2000; Kieffer et al., 2000; Langevin et al., 2007). Due to its sublimation, an asymmetric retreat of the south seasonal CO_2

ice occurs during spring (Colaprete et al., 2005; Giuranna et al., 2007). This cryptic area has a fairly consistent boundary (approximately at latitudes from 73 to 90; Figure 1.7) with small–scale variations in each year (Calvin et al., 2017). It was also observed to host dark spots/fans deposits in spring which are seen as evidences of CO_2 gas jetting (Kieffer, 2000; Piqueux et al., 2003).

The classic "cryptic area" (Figure 1.7) is characterized by TES observations (Paige and Keegan, 1995; Kieffer et al., 2000; Kieffer et al., 2006). However, some areas at the south pole are outside that region and still show cryptic behavior. This suggests that translucent CO_2 slab ice can also occur in small blocks that may be too small to be detected by TES (Hansen et al., 2010).

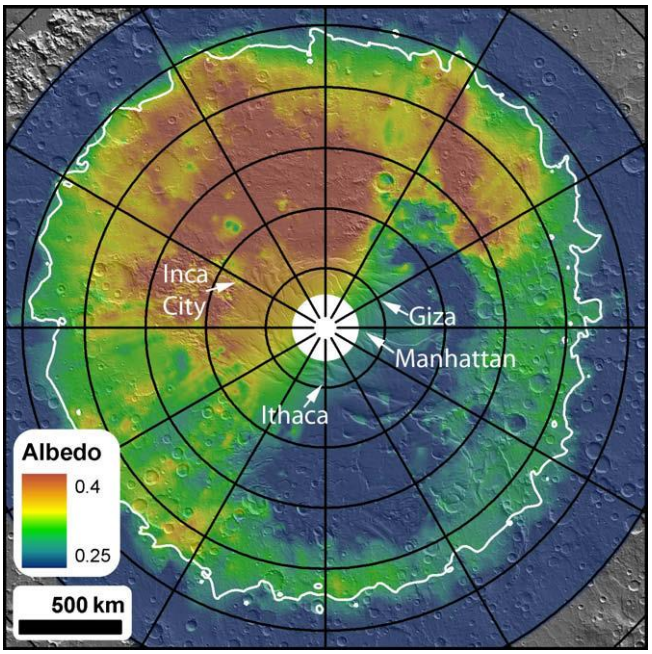

Figure 1.7 The approximate location of the cryptic area. This figure is shown as Figure 1 in Hansen et al. (2010). The colored albedo data (the seasonal range of Ls is 220–225) measured by Mars Odyssey Thermal Emission Spectrometer (TES; Christensen et al., 2001) is superimposed on the shaded relief map of Mars Odyssey Neutron Spectrometer (MOLA; Smith, 2001a). The white polygon delineates the extent of the seasonal CO_2 ice which is determined from thermal data. The bluish low–albedo region from 2 o'clock to 7 o'clock within the white polygon (at lower right) is the cryptic area. Intervals of lines of longitudes and latitudes are spaced 30° and 5° respectively. "Inca City", "Giza", "Ithaca", and "Manhattan" are informal names for the target of interest regions for repeated coverages throughout the spring by HiRISE (McEwen et al., 2007).

1.1.3 The south polar area of Mars

The south polar area (Figure 1.8) is among the most dynamic regions on Mars. It occurs in the southern highland and ~4 km above the surrounding cratered terrain (Barlow, 2008; Byrne, 2009). The south polar area is notably higher in elevation than its northern counterpart which rests on topographically low plains

(Figure 1.9, Carr, 2006; Zuber et al., 1998). The underlying topography of the south polar area is densely cratered, thus suggesting a relatively older age than that of the northern one (Herkenhoff and Plaut, 2000; Hartmann and Neukum, 2001; Fishbaugh and Head, 2001; Koutnik et al., 2002; Byrne and Ivanov, 2004; Milkovich and Plaut, 2008; Limaye et al., 2012; Tanaka et al., 2014). Due to the large eccentricity of the Martian orbit 0.1 (compared to the Earth 0.02) and the coincidence of its apocenter and southern winter, winters in the southern hemisphere are longer and colder which possibly lead to the south seasonal ice being more extensive (~45°S) than that of the north pole (~55°N) (Kieffer, 1979; Titus et al., 2003, Byrne, 2009; Carr, 2006; Langevin et al., 2007).

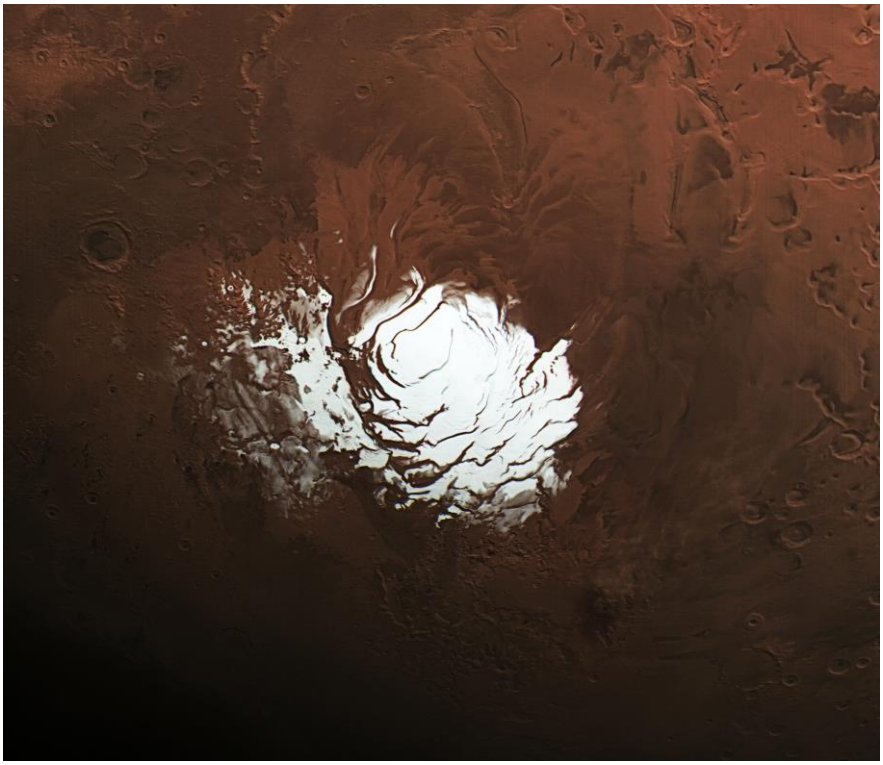

Figure 1.8 The south polar area in oblique view during summer imaged by the High Resolution Stereo Camera (HRSC; Jaumann et al., 2007; 2015; Gwinner et al., 2016) aboard Mars Express. The orbit number is 14150, and the image is ~2000 km across. The white area is CO_2 ice. The south polar area consists of the polar layered deposits (SPLD), the south residual CO_2 polar cap, and the seasonal CO_2 ice.

The south and north polar area consist of the south/north residual polar cap (SPLC/NPLC), the south/north polar layered deposits (SPLD/NPLD), and the south/north seasonal ice. As shown in Figure 1.4, SPLC is characterized by scarps and spiraling troughs with a clockwise pattern (Howard et al. 1982; Fisher 1993, 2000; Thomas et al., 2000; Schenk and Moore 2000). One possible formation mechanism for this clockwise pattern is they were created by aeolian erosion resulted from katabatic winds with katabatic jumps (Smith et al., 2013; Smith et al., 2015) which also applies to the counterclockwise pattern in the north counterpart (Figure 1.4).

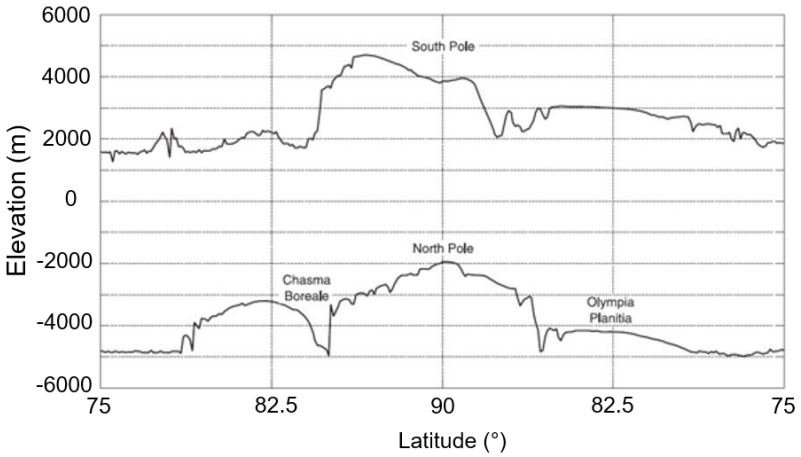

Figure 1.9 Profiles across the south and north polar area based on MOLA (Carr, 2006). The south polar area is ~ 6 km higher in elevation than the north one. Both layered deposits are ~3 km thick.

The NPLC's center has nearly no offset from the rotational pole (Zuber et al., 1998) while the SPLC is located within longitudes 220°E–50°E and latitudes 84°S–89°S which offsets from the geographic pole by ~3° (Figure 1.4 and 1.5). This asymmetry may be due to two distinct climate regimes caused by the Hellas and Argyre basin (Colaprete et al., 2005; Giuranna et al., 2007; 2008). The two topographies result in a planetary wave which produces longitudinal thermal asymmetries: a low–pressure and cold western hemisphere and high–pressure and warmer eastern hemisphere (Colaprete et al., 2005; Giuranna et al., 2007; 2008). Thus, atmospheric precipitation dominates in the western hemisphere leading to smaller grains and high albedo (Calvin and Martin, 1994; Warren et al., 1990), while direct vapor deposition primarily occurs in the eastern hemisphere creating larger grains and low albedo. High albedo gives rise to low ice sublimation rates, which possibly explains why the south residual cap is CO_2 and located in the western hemisphere and survives summers. This difference in deposition patterns possibly also results in the cryptic area in the western hemisphere.

The south polar residual ice cap (SPRC) hosts a large number of sublimation features which are flat floored, circular depressions embedded in the ice and dubbed "Swiss Cheese Terrain" (SCT) (Thomas et al. 2000; Malin and Edgett, 2001; Milkovich and Plaut, 2008). They eroded into the CO_2 ice ranging from ~1 to ~10 m deep (Bibring et al., 2004, Byrne and Ingersoll, 2003, Titus et al., 2003). They still undergo erosion and annual variability in depression boundaries today (Thomas et al., 2009; James et al., 2010).

Vast dunes are distributed on the NPLD, forming an encircling dune erg, while on the SPLD dunes are present primarily in craters. The cause of the dune distribution difference is not clearly; it may be caused by the presence of the south residual CO_2 cap (Carr, 2006).

The south polar area is basically composed of H_2O ice, CO_2 ice, and dust (Leighton and Murray, 1966; Kieffer et al., 1976; Kieffer, 1979; Bibring et al., 2004; Barlow, 2008). Interaction of these components with the atmosphere causes the polar area to undergo distinct changes over Martian seasons. While the south polar area is a result of conditions and changes of Mars climates, it plays an essential role in the global energy budget and balance of Mars.

1.1.4 The substrate material of the south polar area

Under the translucent seasonal CO_2 ice, thermal inertia measurements from Viking infrared thermal mapper (IRTM; Chase et al., 1978) by Paige and Keegan (1995), MGS Thermal Emission Spectrometer (TES; Christensen et al., 2001) by Putzig et al. (2005), and Mars Odyssey's Thermal Emission Imaging System (THEMIS; Christensen et al., 2004) by Fergason et al. (2006) suggest the south polar area ($\geqslant$65°) is dominated by fine–grained and loosely packed or porous material (Mellon et al., 2000; Mitrofanov et al., 2004; Putzig et al., 2005), and the particle size is estimated to be 50–200 μm in diameter (Kieffer et al.,1977; Paige and Keegan, 1995; Putzig et al., 2005; Fergason et al., 2006). Thickness of this easily erodible material (Piqueux et al., 2003) is poorly constrained due to the lack of drilling data. One indirect estimation method for this thickness is through calculating the hydrogen content in the substrate (Chapter 2.1.4): hydrogen has been detected at a depth of millimeters to meters in the substrate (Boyton et al., 2002; Mitrofanov et al., 2002; Feldman et al., 2002; Mitrofanov et al., 2004; Putzig et al., 2005); thus the thickness of this unconsolidated desiccated material should be up to meters (Mellon and Jakosky, 1995; Mellon et al., 2004; Mitrofanov et al., 2004). Based on this estimation principle, one dry porous surface layer of substrate with depths from millimeters to meters is thought to overlie a layer rich in water ice (Leighton and Murray, 1966; Mellon and Jakosky, 1993; 1995; Boynton et al., 2002; 2003; Feldman et al., 2002b; Mitrofanov et al., 2002; 2004; Tokar et al., 2002; Mellon et al., 2004; Titus et al., 2003; Aharonson and Schorghofer, 2006; Putzig et al., 2005; Demidov et al., 2015; Pathare et al., 2018) which is consistent with the abovementioned thermal measurements.

Such porous, fine, permeable, and unconsolidated properties of the substrate material at the south pole allow various surface processes, e.g., thermal contraction, and facilitate the formation of specific features, e.g., spiders.

So far, the south polar area hosts no lander or rover; thus information of permeability, porosity, and cohesion of the substrate are poorly constrained as well as the particle shapes.

1.1.5 Araneiform terrain (spider)

Spiders are characterized by radially–organized or dendritic troughs carved into the substrate, usually with central depressions or pits. They are so far observed only at the south pole with no terrestrial analogs and usually in groups (Figure

1.10). They have a spatial scale ranging from ~45 m to ~1 km, the depths and trough widths are up to meters (Kieffer, 2000; Malin and Edgett, 2001; Piqueux, et al., 2003; Hansen et al., 2010; Portyankina et al., 2013; Hargitai and Kereszturi, 2015).

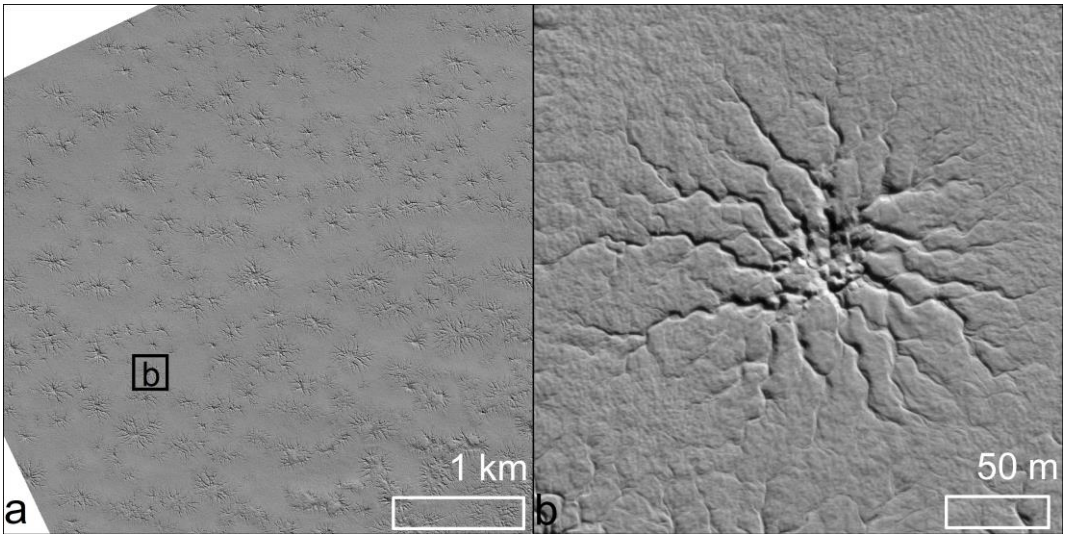

Figure 1.10 Spiders observed in a HiRISE (McEwen et al., 2007) image (ESP_014123_0930, centered at ~87.0°S, ~128.64°E). A group of spiders is shown in (a). Black square indicates the location of (b) which presents the morphology of one spider. Spider troughs are radially organized and have negative topography. In both (a) and (b), the sun comes from the upper right.

They were first identified by the team of Mars Orbiter Camera (MOC) onboard the Mars Global Surveyor (MGS) (Kieffer, 2000) and dubbed "spiders". Hansen et al. (2010) proposed the term "araneiform terrain". Current publications frequently use "araneiforms" as nouns. According to the earliest reference of 1847 (Figure 1.11), *araneiformia* is the suggested plural. In this work, I use "spider(s)" and the adjective form "araneiform terrain".

In view of spider's peculiar appearances, many ideas have been put forward to explain their origins (Kieffer, 2000; 2007; Piqueux et al., 2003; Hansen et al., 2010; Thomas et al., 2010, 2011a and 2011b; Chinnery et al., 2018; Hao et al., 2019). Kieffer (2000; 2007) proposed CO_2 gas jetting caused by basal sublimation of translucent CO_2 slab ice to be responsible for spider formation. Hereafter, I refer his model as Kieffer model (Figure 1.12). Literature uses the terms, cold CO_2 jets, dry venting of CO_2, solid–state greenhouse, cryo jets, and cryo–venting, to refer to the process proposed in Kieffer model. In this thesis, I used CO_2 gas jetting or CO_2 jets. Kieffer model had met few challenges since its publication, and later researchers refined it (Piqueux et al., 2003; Kieffer, 2007; Hansen et al., 2010; Pilorget and Forget, 2015; Portyankina et al., 2017).

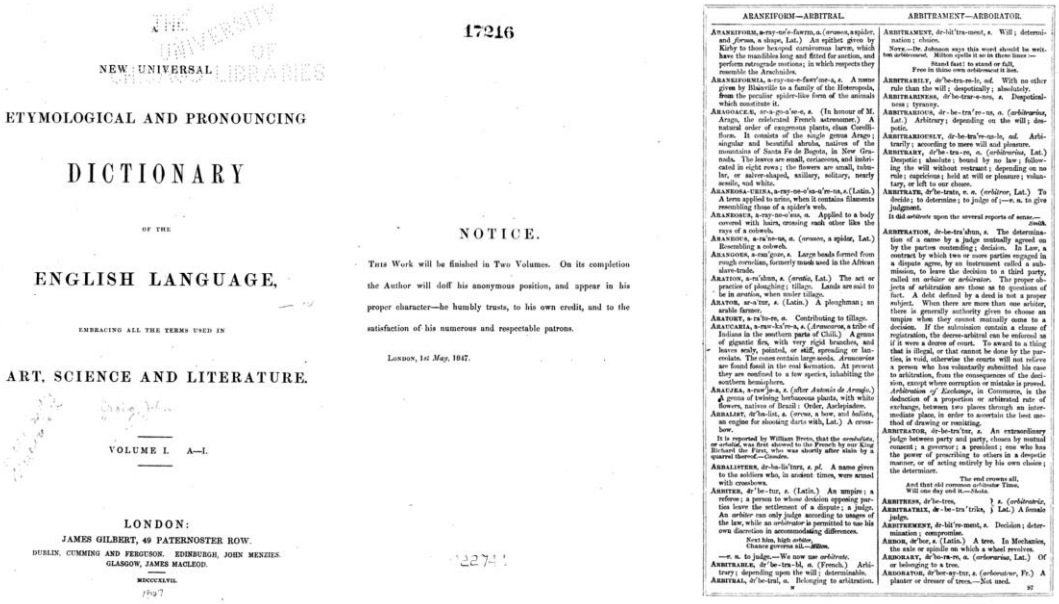

17216

NEW UNIVERSAL

ETYMOLOGICAL AND PRONOUNCING

DICTIONARY

OF THE

ENGLISH LANGUAGE,

EMBRACING ALL THE TERMS USED IN

ART, SCIENCE AND LITERATURE.

VOLUME I. A—I.

LONDON:
JAMES GILBERT, 49 PATERNOSTER ROW.
DUBLIN, CUMMING AND FERGUSON. EDINBURGH, JOHN MENZIES.
GLASGOW, JAMES MACLEOD.
MDCCCXLVII.

NOTICE.

THIS Work will be finished in Two Volumes. On its completion the Author will doff his anonymous position, and appear in his proper character—he humbly trusts, to his own credit, and to the satisfaction of his numerous and respectable patrons.

LONDON, 1st May, 1847.

ARANEIFORM—ARBITRAL.

ARANEIFORM, a-ray-ne'e-fawrm, a. (*aranea*, a spider, and *forma*, a shape, Lat.) An epithet given by Kirby to those hexapod curculionous larvæ, which have the mandibles long and fitted for suction, and perform retrograde motions; in which respects they resemble the Arachnides.

ARANEIFORMIA, a-ray-ne-e-fawr'me-a, s. A name given by Blainville to a family of the Heteropoda, from the peculiar spider-like form of the animals which constitute it.

ARAUCARIA, ar-a-ga-ri'a-a, s. (In honour of M. Arago, the celebrated French astronomer.) A natural order of exogenous plants, class Coniferæ. It consists of the single genus Arago; singular and beautiful shrubs, natives of the mountains of Santa Fe de Bogota, in New Granada. The leaves are small, cartaceous, and imbricated in eight rows; the flowers are small, tubular, or salver-shaped, axillary, solitary, nearly sessile, and white.

ARANEOLA-URINA, a-ray-ne-o'la-u'ri-na, s. (Latin.) A term applied to urine, when it contains filaments resembling those of a spider's web.

ARANEOUS, a-ray-ne-o'us, a. Applied to a body covered with hairs, crossing each other like the rays of a cobweb.

ARANEOUS, a-ra'ne-us, a. (*aranea*, a spider, Lat.) Resembling a cobweb.

ARANGOZIA, a-ran'gose, s. Large beads formed from rough cornelian, formerly much used in the African slave-trade.

ARATION, a-ra'shun, s. (*aratio*, Lat.) The act or practice of ploughing; tillage. Lands are said to be in aration, when under tillage.

ARATOR, ar-a'tur, s. (Latin.) A ploughman; an arable farmer.

ARATORY, a-ra'to-re, a. Contributing to tillage.

ARAUCARIA, a-raw-ka'ri-a, s. (*Araucanos*, a tribe of Indians in the southern parts of Chili.) A genus of gigantic firs, with very rigid branches, and leaves scaly, pointed, or stiff, spreading or lanceolate. The cones contain large seeds. *Araucarites* are found fossil in the coal formation. At present they are confined to a few species, inhabiting the southern hemisphere.

ARAUJIA, a-raw'je-a, s. (*after Antonio de Araujo.*) A genus of twining herbaceous plants, with white flowers, natives of Brazil: Order, Asclepiades.

ARBALIST, ár'ba-list, s. (*arcus*, a bow, and *ballista*, an engine for shooting darts with, Lat.) A cross-bow.

It is reported by William Breton, that the *arcubalista*, or *arbalist*, was first showed to the French by our King Richard the First, who was shortly after slain by a quarrel thereof.—*Camden.*

ARBALISTERS, ár-ba-lis'turz, s. pl. A name given to the soldiers who, in ancient times, were armed with crossbows.

ARBITER, ár'be-tur, s. (Latin.) An umpire; a referee; a person to whose decision opposing parties leave the settlement of a dispute; a judge. An *arbiter* can only judge according to usages of the law, while an *arbitrator* is permitted to use his own discretion in accommodating differences.

Next him, high *arbiter*,
Chance governs all.—*Milton.*

—v. n. to judge.—We now use *arbitrate*.

ARBITRAGE, ár'be-trá-hl, s. (French.) Arbitrary; depending upon the will; determinable.

ARBITRAL, ár'be-tral, a. Belonging to arbitration.

ARBITRAMENT—ARBORATOR.

ARBITRAMENT, ár-bit'tra-ment, s. Will; determination; choice.

NOTE.—Dr. Johnson says this word should be written *arbitrement*. Milton spells it so in three lines:—

Stand fast: to stand or fall,
Free in thine own *arbitrement* it lies.

ARBITRARILY, ár'be-tra-re-le, ad. With no other rule than the will; despotically; absolutely.

ARBITRARINESS, ár'be-trar-e-nes, s. Despotism; tyranny.

ARBITRARIOUS, ár-be-tra're-us, a. (*arbitrarius*, Lat.) Arbitrary; depending on the will; despotic.

ARBITRARIOUSLY, ár-be-tra're-us-le, ad. Arbitrarily; according to mere will and pleasure.

ARBITRARY, ár'be-tra-re, a. (*arbitrarius*, Lat.) Despotic; absolute; bound by no law; following the will without restraint; depending on no rule; capricious; bold at will or pleasure; voluntary, or left to our choice.

ARBITRATE, ár'be-trate, v. a. (*arbitror*, Lat.) To decide; to determine; to judge of;—v. n. to give judgment.

It did *arbitrate* upon the several reports of sense.—*South.*

ARBITRATION, ár-be-tra'shun, s. The determination of a cause by a judge mutually agreed on by the parties contending; decision. In Law, a contract by which two or more parties engaged in a dispute agree, by an instrument called a submission, to leave the decision to a third party, called an *arbiter* or *arbitrator*. The proper objects of arbitration are those as to questions of fact. A debt defined by a deed is not a proper subject. When there are more than one arbiter, there is generally authority given to choose an umpire when they cannot mutually come to a decision. If the submission contain a clause of registration, the decree-arbitral can be enforced as if it were a decree of court. To award to a thing that is illegal, or that cannot be done by the parties, is void, otherwise the courts will not relieve a person who has voluntarily submitted his case to arbitration, from the consequences of the decision, except where corruption or mistake is proved. *Arbitration of Exchange*, in Commerce, is the deduction of a proportion or arbitrated rate of exchange, between two places through an intermediate place, in order to ascertain the best method of drawing or remitting.

ARBITRATOR, ár-be-tra'tur, s. An extraordinary judge between party and party, chosen by mutual consent; a *governor*; a president; one who has the power of prescribing to others in a despotic manner, or of acting entirely by his own choice; the determiner.

The end crowns all,
And that old common *arbitrator* Time,
Will one day end it.—*Shaks.*

ARBITRESS, ár'be-tres, } s. (*arbitratrix*,
ARBITRATRIX, ár-be-tra'triks, } Lat.) A female judge.

ARBITREMENT, ár-bit're-ment, s. Decision; determination; compromise.

ARBOR, ár'bor, s. (Latin.) A tree. In Mechanics, the axis or spindle on which a wheel revolves.

ARBORARY, ár'bo-ra-re, a. (*arborarius*, Lat.) Of or belonging to a tree.

ARBORATOR, ár'bor-ay-tur, s. (*arborator*, Fr.) A planter or dresser of trees.—Not used.

Figure 1.11 Araneiform: having the shape of a spider. Substantive plural form: araneiformia. Pages from John Craig, *A new universal etymological and pronouncing dictionary of the English language, embracing all the terms used in art, science and literature,* 1847–49.

I here outline the current generally–accepted scenario of spider formation which is based on the Kieffer model: (1) CO_2 in the atmosphere condenses over the south pole during late fall and winter forming the seasonal CO_2 ice up to 2.5 m thick, a part of the seasonal CO_2 ice is in the form of translucent slab ice (Kieffer, 2000; Smith et al., 2001a; Aharonson et al., 2004; Langevin et al., 2007); (2) in spring, due to basal sublimation of the translucent CO_2 ice, gas is trapped beneath the CO_2 ice (Kieffer, 2007; Piqueux et al., 2003; Hansen et al., 2010; Pilorget and Forget, 2015; Hao et al., 2019; 2020), (3) the overlying ice layer breaks at some point, possibly forming seasonal cracks (Portyankina et al., 2012), so that gas rushes out, mobilizing substrate material into the atmosphere which then deposits onto the surface. When encountering local winds, jetted material may be blown into fan–shaped deposits (dark fans) with uniform or multiple directions (Thomas et al., 2010 and 2011a; Aye et al., 2019), otherwise forming dark spots. These erupted deposits blend into the background when the seasonal ice is gone, but some are still visible as black or dark–toned on images possibly due to the contrast between the CO_2 ice and substrate material. During the jetting process, the substrate beneath the CO_2 ice undergoes erosion; (4) with seasonal repetitions from (1) to (3), dendritic or radial troughs, known as araneiform terrain or "spiders", are cut into the substrate and remain observable into late summer. In winter, we lack images because of darkness due to Mars obliquity of ~25°; but as early as the beginning of spring, we can observe spiders in HiRISE images (McEwen et al., 2007). These hypotheses

were partly confirmed by laboratory experiments (Kaufmann and Hagemann, 2017; de Villiers, et al., 2012; McKeown et al., 2017; Portyankina et al., 2018).

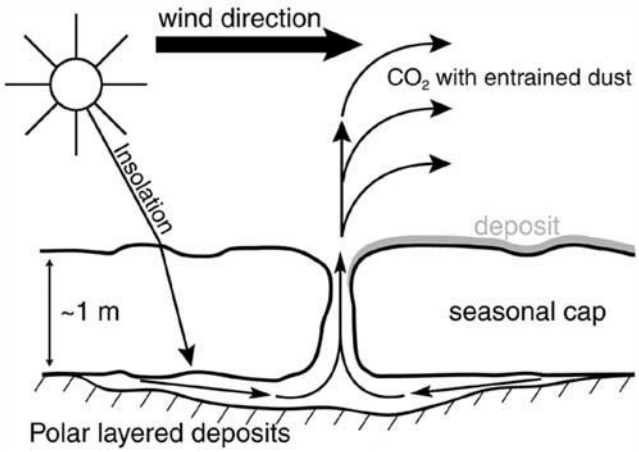

Figure 1.12 Kieffer model (Kieffer, 2000) presented by Piqueux et al. (2003). South polar layered terrain is overlain by the seasonal translucent CO_2 slab ice of ~1 m in thickness (Later data suggested the thickness is up to 2.5 m (Aharonson et al., 2004)). Solar energy reaches the base of the seasonal translucent CO_2 slab ice leading to sublimation from the bottom, and a pressurized CO_2 gas build–up. When the ice ruptures, the gas rushes out entraining dust resulting in dark fan–shaped deposits. This process with repetition from year to year leads to erosion of the underlying polar layered deposits creating spiders (Piqueux et al., 2003).

Based on estimated volumes of spiders and dark deposits in the same area from thermal modeling (Piqueux and Christensen, 2008) and direct volume measurements from HiRISE DTMs (Portyankina et al., 2017), spiders were evaluated to be older than 10^4 years (Piqueux and Christensen, 2008; Portyankina et al., 2017). Recently, some new troughs were observed growing and branching (Portyankina et al., 2017) in the vicinity of dune areas at 69–71°S, which could be the early stage of spider formation (Chapter 3.4).

These CO_2–related processes occur at both poles and give rise to the formation of features either observed at both poles, e.g., dark spots/fans, seasonal cracks, or unique to one pole, e.g., seasonal furrows at the north pole and araneiform terrain (spider) at the south pole (Piqueux et al., 2003; Hansen et al., 2010; 2011; 2013; Pommerol et al., 2011; 2013; Bourke, 2013; Portyankina et al., 2010; 2012; 2013; 2017; Schwamb et al., 2017). Seasonal furrows, produced by a similar mechanism to that of spiders, have only been observed in the north polar area (Bourke, 2013; Hansen et al., 2013). They are ephemeral and form annually (Bourke, 2013), while spiders are perennial and observed with no morphological changes during observation by spacecraft.

1.2 Research motivation and objectives

Mars had long been an enigma to humankind. Only on entering into the telescope age had scientists started to have opportunities to observe Mars in detail. It was at this time, astronomers had noticed the intriguing phenomena of polar caps on Mars: they were bright and seemed to undergo temporal variations, and the south polar cap was misplaced with the rotational pole (Paige and Ingersoll, 1985; Kieffer et al., 1977). Especially, the bright caps and their receding and advancing raised the idea that Mars may host life as these behaviors resembled liquid water. The polar caps were suggested to be composed of water ice, such that its sublimation and condensation contributed to the observed waning and waxing behavior. The establishing work performed by Leighton and Murray 1966 following Mariner 4 predicted that the seasonal polar caps were possibly comprised of CO_2 ice as water ice was thought unstable under current Martian atmospheric pressure and temperature conditions. Infrared radiometer and thermal data from the later missions (e.g., Mariner 7 and 9) confirmed this hypothesis (Herr and Pimentel, 1969; Neugebauer et al., 1971; Larson and Fink, 1972). Since then, our understanding of the poles of Mars has been vastly advanced by analyzing datasets with various bandwidths and resolutions acquired from space missions, e.g., 1996 Mars Global Surveyor (MGS), 2001 Mars Odyssey (MO), 2003 Mars Express (MEx), 2005 Mars Reconnaissance Orbiter spacecraft (MRO), 2007 Phoenix lander, and 2016 ExoMars Trace Gas Orbiter (TGO). The polar areas of Mars are far more intriguing than scientists originally speculated. What followed were new scientific questions and mysteries, in particular regarding the formation of polar features. My work is to try to elucidate pieces of these mysteries.

The polar area of Mars hosts an abundance of landforms that are subject to variation under changing environmental conditions (e.g., Byrne and Ingersoll, 2003; Piqueux et al., 2003; van Gasselt et al., 2005; Carr, 2006; Piqueux and Christensen, 2008; Jian et al., 2009; Thomas et al., 2010; Portyankina et al., 2010 and 2018). Among these polar features, spiders are promising study objects: they have negative topographies and form through basal sublimation of seasonal CO_2 ice and later gas jetting with substrate material mobilization, which are directly linked to CO_2 cycles being a crucial part of Mars global circulation. CO_2 gas jetting is suggested as the key agent for shaping and modifying the polar surface of Mars (Piqueux et al., 2008; Mc Keown et al., 2017); it is directly linked to the seasonal evolution of the poles which are among the most sensitive regions to Mars climate. Studies of spider spatial configuration and formation help understand what is the role of CO_2 and dust in polar surface processes and how spider formation affects the shaping and modification of the past/current polar surface. Thus, better understanding of spider spatial configuration and formation provides insight into the atmosphere–

surface interaction processes and essential implications on the evolution of the polar regions and climates.

The formation mechanism and spatial configuration of araneiform terrain are still not fully understood, , e.g., the thorough schematics of basal–sublimation, subsequent CO_2 jetting and substrate erosion, the detailed process of central pit growth into dendritic or radial troughs instead of others, the causes of their various morphologies (e.g., spider size and trough lengths), the reason why spiders occur in groups, whether their spatial distributions are random or not, the factors controlling the spatial configuration. My research objectives are to address these issues.

1.3 Thesis organization and author contribution

The dissertation is organized in a classic monographic manner. It combines elements taken over from two published/accpeted papers: "*Hao, J., Michael, G., Adeli, S., Jaumann, R., 2019. Araneiform terrain formation in Angustus Labyrinthus, Mars. Icarus 317, 479–490, doi:org/10.1016/j.icarus.2018.07.026*" and *"Hao, J., Michael, G., Adeli, S., Jaumann, R., Portyankina, G., Hauber, E., Millot, C., Zuschneid W., 2020. Variability of araneiform spatial configuration at the Martian south pole. Planetary and Space Science, in press. doi:org/10.1016/j.pss.2020.104848*". As the first authors of the two papers, I accumulated and processed the data, selected research approaches and methodologies, interpreted and analyzed the results, referenced to literature, discussed and concluded the works. During the preparation stage of the manuscripts, all co–authors were consulted.

This monograph dissertation is composed of seven chapters in total. Chapter I is an introductory part including the scientific background, an introduction into the study area–the south pole of Mars, research topics, and followed with research motivations and objectives. It integrates part of the content from the two papers' "Introduction" chapters.

Chapter II describes the data and methods used in this thesis to meet the research objectives. It synthesizes data and methods from the two published/accepted papers.

Chapter III includes the published research paper at Icarus (Hao et al., 2019). As the first author, I selected the area of interest, collected the images and DTM, reviewed the relevant literature, performed detailed mapping, conducted spatial randomness analysis, measured the parameters of spiders, interpreted and discussed the results, and concluded this work. Co–authors participated in discussions and reviews of the draft manuscript. The dataset and methodology subchapters of the paper is synthesized into Chapter II. Other contents are mostly consistent with the original published state. This work is about the in–depth case study in Angustus Labyrinthus (also informally known as "Inca City")

of Mars. The core of this work is the new spider formation model I proposed. This new model provides explanations for several mysteries in spider studies. Another critical finding of this work is the model predicts that spatial distribution of spiders is non–random which has not been reported before; this non-randomness was confirmed by quantified method. In addition, based on detailed spatial mapping, two new spider types (half and elongated) are reported and classified.

Chapter IV contains the accepted paper at Planetary and Space Science (Hao et al., 2020). I selected seven study regions, chose the research approaches, referenced the related literature, collected all the data, analyzed and discussed the results, and concluded the work. Millot Cedric contributed to the calculation of insolation. Co–authors participated in discussions during the preparation of the manuscript. The data and methods and parts of the introduction are synthesized into Chapters I and II, respectively. This work is about case studies in another six regions plus Angustus Labyrinthus (area of interest in Chapter III). The research core of this work is the detailed investigation of spatial configuration of spiders and their troughs at the south pole. Non-random spatial configurations of spiders are found in all the study regions with a regional variation, while spider trough orientations are reported random confirmed by trough orientations mappings and rose diagrams. Relevant parameters of spider formation and spatial configuration are classified and analyzed to explain observations and measurements.

Chapter V introduces the observations of spiders from the newly operating Colour and Stereo Surface Imaging System instrument (CaSSIS; Thomas et al., 2017) on the ExoMars Trace Gas Orbiter. The new observations include new locations for spiders, in which Half and elongated spiders are observed; their formation is discussed. I filtered the CaSSIS images, selected areas of interest, collected all the data, interpreted the observations, analyzed and discussed the results, then I concluded this work.

Chapter VI discusses the results and conclusions of the two resrach papers (Hao et al., 2019; Hao et al., 2020) presented in Chapter III and IV and the research in Chapter V. I discuss research findings of my work and emphasize my contributions to the Mars sciences.

Chapter VII summaries conclusions of my work and research findings. This chapter is concluded with the outlook.

Chapter II. Dataset and methods

Topographic, thermal, radar, hyperspectral, and high–resolution imaging data allow researchers to study Mars in unprecedented detail. The poles of Mars have been monitored with spacecraft instruments for decades, obtained data have provided an excellent opportunity to understand the polar processes and their interaction with climate variations. This chapter contains datasets and methods extracted from the two published/accepted papers, Hao et al., 2019 Icarus, and Hao et al., 2020 PSS, which are presented in Chapters III and IV.

2.1 Dataset

Since no landers or rovers have been landed at the south pole so far, remote sensing data of orbiters is an essential means for observation of spiders: visible images, e.g., High Resolution Imaging Science Experiment (HiRISE; McEwen et al., 2007), High Resolution Stereo Camera (HRSC; Jaumann et al., 2007; 2015; Gwinner et al., 2016), and Colour and Stereo Surface Imaging System (CaSSIS; Thomas et al., 2017); topographic data, e.g., DTM of MOLA (Smith, 2001a), HiRISE and Context Camera (CTX; Malin et al., 2007); and thermal inertia data from Thermal Emission Spectrometer (TES; Christensen et al., 2001) and Thermal Emission Imaging System (THEMIS; Christensen et al., 2004). All the datasets used in this thesis were projected into Polar Stereographic Projection in ArcGIS 10.3.

2.1.1 Imagery data

a. HiRISE

High Resolution Imaging Science Experiment (HiRISE; McEwen et al., 2007) is one of the six instruments onboard the Mars Reconnaissance Orbiter (MRO). It started to acquire data in the year 2006 and has observed the Martian surface with image scale or sampling rate as high as 0.25 m/pix (McEwen et al., 2007, 2010). This image scale points to the highest spatial resolution 0.75 m/pix based on the sampling theorem (McEwen et al., 2007). HiRISE can obtain informative images under poor illumination conditions, e.g., at low solar elevation angles. HiRISE acquires images through an array of 14 staggered CCD arrays, 10 of which observe through red filters (RED) and together cover the full swath. The remaining CCD lines employ blue–green and near infrared filters. The RED images were used in this work. Since the spiders' spatial scale ranges from 45 m to 1 km and their trough widths vary from centimeters to meters, HiRISE's spatial resolution enables detailed observations of spider's morphologies to perform a comprehensive study of spider formation and spatial configuration. HiRISE images used in this thesis were downloaded from *https://www.uahirise.org/* and listed in Table S1.

b. HRSC

High Resolution Stereo Camera (HRSC; Neukum et al., 2004, Jaumann et al., 2007; 2015; Gwinner et al., 2016) operates on Mars Express (MEx) and works as push–broom scanning camera. It has nine CCD line detectors and provides broad and continuous coverage of the Martian surface with a surface resolution as high as 10 m/pix, thus HRSC provides geology context for spider populations. HRSC has the unique ability to acquire near–simultaneous images for one specific site with five phase angles. In this thesis, I used two HRSC nadir (Nd) images which entirely cover one study area complementing observation gaps caused by limited HiRISE images. The HRSC image used in the thesis was provided by the HRSC team of Freie Universität Berlin.

c. CaSSIS

Colour and Stereo Surface Imaging System (CaSSIS; Thomas et al., 2017) is part of the payload onboard the ExoMars Trace Gas Orbiter (TGO) launched in 2016. It acquires images in push–frames way. It is non–sun–synchronous with an orbital inclination of 74° and provides multi–local time observations (obtaining images at a rate of 10–20 images/day), which enables to investigate dynamic surface processes, e.g., seasonal sublimation of CO_2. Due to its orbital characteristics, it focuses on monitoring mid–to–low–latitudes (<±75°).

CaSSIS is a 4–color visible (blue, panchromatic, red, and near–infrared) and near–infrared stereo camera and acquires images at spatial resolution 4.6m/pix. CaSSIS was developed and is operated by University of Bern, and acquires observations in areas which HiRISE or other high–resolution observations have not covered. In this thesis, I used images from the panchromatic channel, which were processed at the Institute of Planetary Research of the Deutsches Zentrum für Luft– und Raumfahrt Zentrum e.V. (DLR).

2.1.2 Topographic data

Topographic data in this thesis refers to a digital terrain model (DTM). The topographic settings for the study area, e.g., elevations, slopes, and aspects or orientations of slopes, can be measured from a DTM.

In this thesis, I used DTMs from MOLA, CTX, and HiRISE. The large–scale MOLA DTM (e.g., global scale) can present the general topographic context allowing to locate local or regional features. CTX and HiRISE DTMs, with limited coverage but higher spatial resolutions, provide more details in the local topography than MOLA DTM.

a. MOLA

The Mars Orbiter Laser Altimeter (MOLA; Smith, 2001a) is aboard the Mars Global Surveyor (MGS). It collected altimetry data and measures the topography globally with a horizontal resolution of kilometers and a vertical accuracy of 1 m.

The global MOLA DTM was produced at the pixel scale of 463 m/pix. Due to the orbital characteristics of MGS, at the poles, the MOLA DTM was gridded to a pixel scale of 115 m/pix. The MOLA DTM for the south pole used in this thesis was downloaded from PDS (*https://pds–geosciences.wustl.edu/mgs/mgs–m–mola–5–megdr–l3–v1/mgsl_300x/polar/*).

b. CTX

The Context Camera (CTX; Malin et al., 2007) operates on MRO and observes Mars surface with the spatial resolution of 6 m/pixel. The CTX DTM was produced based on image pairs at the resolution of 18 m/pix. I used the CTX DTM to calculate local slopes for one study region. The CTX DTM used in the thesis was processed by the Image Understanding team at the University College of London.

c. HiRISE

HiRISE DTM is generated from stereo image pairs. Its major advantage is the high resolution which is up to 1 m/pix (McEwen et al., 2007). However, HiRISE stereo images and DTM cover limited regions. In this thesis, only one HiRISE DTM was available within the study area and it was downloaded from University of Arizona (*https://www.uahirise.org/hiwish/maps/dtms.jsp*).

2.1.3 Thermal inertia data

The thermal inertia (TI) describes the delayed response of a solid material to external heating in its uppermost layers. TI is primarily controlled by the thermal conductivity which is influenced by porosity (Piqueux and Christensen, 2009), thus TI can offer information on surface porosity (Presley and Christensen, 1997). It is usually calculated from day/night surface temperatures (Presley and Christensen, 1997). In this thesis, I used TI derived from thermal infrared bolometer temperatures (Putzig and Mellon, 2007) of the Thermal Emission Spectrometer (TES) (Christensen et al., 2001) onboard MGS. Note that these TI estimations include observations from all seasons, but excluded ones with brightness temperatures below 160 K to avoid the effects of CO_2 frost on the surface, as suggested by Putzig and Mellon (2007). However, the 3 km resolution of the TES TI values (Putzig and Mellon, 2007) is lower than the spatial scale of individual spiders and some study regions.

2.1.4 Water equivalent hydrogen abundance

Water equivalent hydrogen abundance (WEH) is thought to be a measure of water ice content since water ice is the most probable substance containing hydrogen on Mars (Mitrofanov et al., 2002; Boynton et al., 2002; Feldman et al., 2002a). Measuring neutron leakage fluxes from the upper meter of the Martian surface enables WEH calculations. The Neutron Spectrometer (MONS; Feldman et al., 2002b) and Russian High–Energy Neutron Detector (HEND; Mitrofanov et al., 2004) aboard Mars Odyssey provide neutron measurements

which are used to determine the WEH. However, neutron spectroscopy cannot distinguish water ice from hydrous minerals which also contribute to WEH (Feldman et al., 2004; Prettyman et al., 2004; Bandfield and Feldman, 2008). At the south pole, the neutron measurements and the derived WEH are strongly influenced by the contamination from a very large flux of thermal neutrons of the south polar residual CO_2 cap (Feldman et al., 2008), leading to the WEH poleward of 75°S being incorrect (Pathare et al., 2018), I therefore did not use them in my study.

2.2 Methods

2.2.1 Spatial randomness analysis

In order to investigate spiders' spatial configuration, I used the method of spatial randomness analysis which measures the degree of clustering in an observed population relative to a series of randomly distributed populations (Michael et al., 2012). With the aim of performing spatial randomness analysis for a spider population, CraterTools (Kneissl et al., 2011) and Craterstats2 (Michael et al., 2012) were used and repurposed. They were developed to measure craters' distribution and contain functions of spatial mapping and spatial randomness analysis which were revised and applied for spiders in this thesis.

I mapped the boundary of a population of spiders and recorded the spider center positions using CraterTools. In contrast to the clustering analysis of craters which are split into bins by diameter, the diameter of a spider central pit is not considered a relevant parameter in this analysis. Instead, I set all the spiders to the same arbitrary diameter and analyze them as a single group; the reasons are discussed in Chapter III.

The spatial randomness analysis works by adopting a measure for spacings, the value of which varies depending on the degree of clustering–or conversely, separation–of the set of locations, and comparing the value of this measure with the distribution of values found for a series of random spatial configurations. Here I adopt the mean 2nd–closest neighbor distance (M2CND) as the clustering measure in this analysis, which can be understood as relating to the average distance between neighboring points (Michael et al., 2012). The procedure yields an M2CND value for the observed dataset, and a histogram of values for the random Monte Carlo generated spatial configurations. I can evaluate the spatial randomness of the observed spider population based on the actual M2CND value's position relative to the M2CND histogram for random configurations. If the measured M2CND is smaller than for the majority of random configurations, it shows that the spatial distribution is "more clustered than random". If the reverse is true, the configuration may be "more separated than random". Consideration of the measured positions relative to the histogram allows to determine a confidence figure for either of the statements "clustered or separated".

2.2.2 Trough orientation mapping

In order to investigate whether spider troughs have preferred orientations and what factors these may be related to, I performed orientation mapping for each region using HiRISE images. My mapping was performed at a scale of 1:1000.

Spider morphology exhibits noticeable complexity and variability, e.g., troughs often have bifurcations, they are frequently sinuous; a large number of spiders have central depressions with irregular plan–view shapes which are not clearly defined. These varying morphological features of spiders cause difficulties in my mapping, e.g., how to define the trough orientation. Therefore, I chose the following simplified and conservative mapping method, in order to reduce the uncertainties as best as possible.

The spider spatial size is approximately 45 m to 1 km and the length range of segments of spider troughs is proximately ~ 8–35 m. In order to map the troughs, I used one straight line (8m in length) to map only the first straight segment of the trough which emanates from the intersection with the central depression (Figure 2.1). Due to the simplification strategy of my mapping, I did not map the branches or bifurcations of the troughs. After a detailed investigation of the trough widths in the study regions, I observed that troughs wider than 2.5 m are clearly visible in HiRISE images. Therefore, my minimum trough mapping limit is 2.5 m. These settings yield the mapping results which correlate to the general picture of spider trough orientations.

In order to present the trough orientations, I constructed rose diagrams. The bin size of each diagram was set as 5% of the total trough number. The trough orientation mapping and the orientation calculation were conducted using the vector tool and the COGO tool of ArcGIS software, respectively. The rose diagrams were produced using MATLAB.

2.2.3 Insolation

In this work, insolation was computed for each study region by using an IDL program developed by Leyrat et al. (2016). This program used SPICE libraries (Acton, 1996) to retrieve precise relative positions of the Sun and Mars. MOLA DTM was used to extract elevations and compute local slopes and orientations for each MOLA grid. Elevations, slopes, and their orientations were used as input data in the program. Solar fluxes are computed at the top of the atmosphere. I do not include spatial and temporal variations induced by the atmosphere and focus on topographic effects due to Mars atmosphere's low density and current modeling's large scale (degrees in latitudes and longitudes for the global modeling and kilometers for the regional modeling; Sutton et al., 1978; Spiga and Forget, 2008; Spiga et al., 2011).

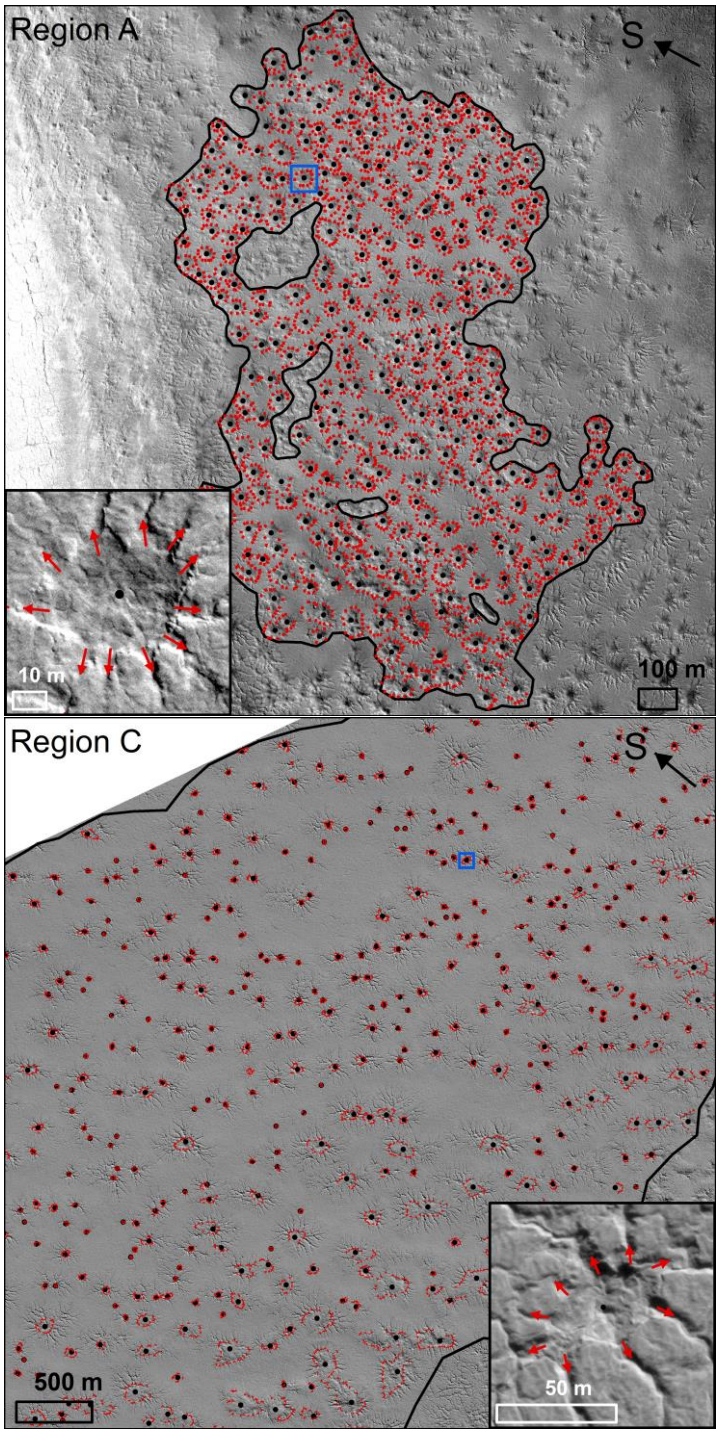

Figure 2.1 Examples of trough orientation mappings (regions A and C, details for the study regions are in Chapter IV). The red arrows indicate the orientations of the troughs of intersections with central depressions outwards to a fixed distance of 8 m. The black points indicate spiders' approximate centers. The black lines delineate the extents of regions A and C. The blue subset frames show examples of trough orientations of two spiders.

Solar fluxes are computed with the following equation:

$$Q = \frac{E}{d^2} \times \cos i \qquad (1)$$

In this equation, Q is the local solar flux in $W \cdot m^{-2}$, E is the solar constant in $W \cdot m^{-2}$, d is the distance to the sun in Astronomical units (AU), and i is the incidence angle in degree. The incidence angle is modified by local slopes and orientations; it is the principal cause of local solar flux variations. I performed 50 iterations/time steps for each sol (sol = a day on Mars, which corresponds to ~24h40m). For each iteration, the increment in time or the time step is 24h40m/50 iterations, i.e., approximately 30 min/iteration. This allows to model insolation values at a given time with an error < 15 minutes. In addition, the great number of time steps used in my work can fully cover diurnal and seasonal cycles and obtain continuous variations of insolation for these time periods. Since one Mars year contains ~669 sols, I thus performed 33450 iterations in total for one Mars year. Mars years (MY) are defined by Clancy et al. (2000). MY 1 with Ls=0 starts from April 11, 1955.

2.2.4 Slopes

In this thesis, slopes were calculated for each grid of MOLA DTM using ArcGIS software. A 3×3 moving window is used to calculate the slope value for this window's central cell. The rate of each cell's elevation change is expressed as slope which takes "degree" as measurement units ranging from 0° to 90°.

Chapter III. Araneiform terrain formation in Angustus Labyrinthus, Mars

This chapter is to introduce the spider formation model I proposed based on the in–depth case study of spiders in one area “Angustus Labyrinthus” of Mars. The key points of this chapter are: (1) A new spider formation model was proposed detailing the mechanism of growth of central pits and radiating troughs; (2) Non–random spatial distributions of spiders are reported for the first time; (3) Half and elongated spiders are newly reported and classified.

The content of this chapter was published as *Hao, J., Michael, G., Adeli, S., Jaumann, R., 2019. Araneiform terrain formation in Angustus Labyrinthus, Mars. Icarus 317, 479–490, https://doi.org/10.1016/j.icarus.2018.07.026.* In this paper, I collected and processed images, mapped the study area, interpreted, and discussed the results. For the co–authors’ contributions, please refer to Chapter 1.3. For the datasets and methods, please refer to Chapter II. Part of “Introduction” of this paper was merged into Chapter I. The rest of the paper Hao et a., 2019 is presented here with additional explanations for several issues.

3.1 Introduction

Araneiform terrain or spider has been studied for decades. However, the detailed growth mechanisms of central pits and troughs, thorough schematics of basal–sublimation, gas jetting, and substrate erosion, remain incompletely understood. The goal of this work is to address these issues. The Angustus Labyrinthus is located at ~81°S and ~296°E (Figure 3.1). It has a wide variation of surface slopes and orientations that form roughly square cells containing prominent geomorphological features including a considerable number of spiders (Piqueux et al., 2003; Hansen et al., 2010; Pommerol et al., 2011), and has since been repeatedly covered by HiRISE images for over four Mars years. These offer an opportunity to investigate the formation mechanism of araneiform terrain in detail. Thus, I performed a case study in Angustus Labyrinthus with increased HiRISE images, particularly the active zones of spring sublimation and surface changes documented by Hansen et al. (2010).

3.2 Study area

Angustus Labyrinthus, ~700 km^2 in area, exhibits a rectilinear pattern of ridges and internal polygons that resembled Incan ruins when first discovered in 1972 (Sharp, 1973) and thus became known colloquially as “Inca City” (Figure 3.1). The rectilinear ridges are up to 100 m in height and several hundred meters in width and enclose polygons around 3 km across (Kerber et al., 2017). The origin of Angustus Labyrinthus is not yet well understood, and possible formation mechanisms include aeolian mantling lithified by cementation (Malin

et al., 1998), ice accumulation (Malin et al., 1998) or linked to the neighboring Dorsa Argentea Formation, which contains many ridge segments interpreted to be eskers (Howard, 1981; Head et al., 2001; Kress and Head, 2015). The Inca City region is close to the south pole (Figure 3.1) and outside the cryptic area defined by TES observation shown in Figure 1.5 (Chapter I). However, it exhibits cryptic behavior during the frosting season (Piquexu et al., 2003). It hosts substantial numbers of spiders (Piqueux et al., 2003; Hansen et al., 2010), thus providing adequate samples to study them in detail.

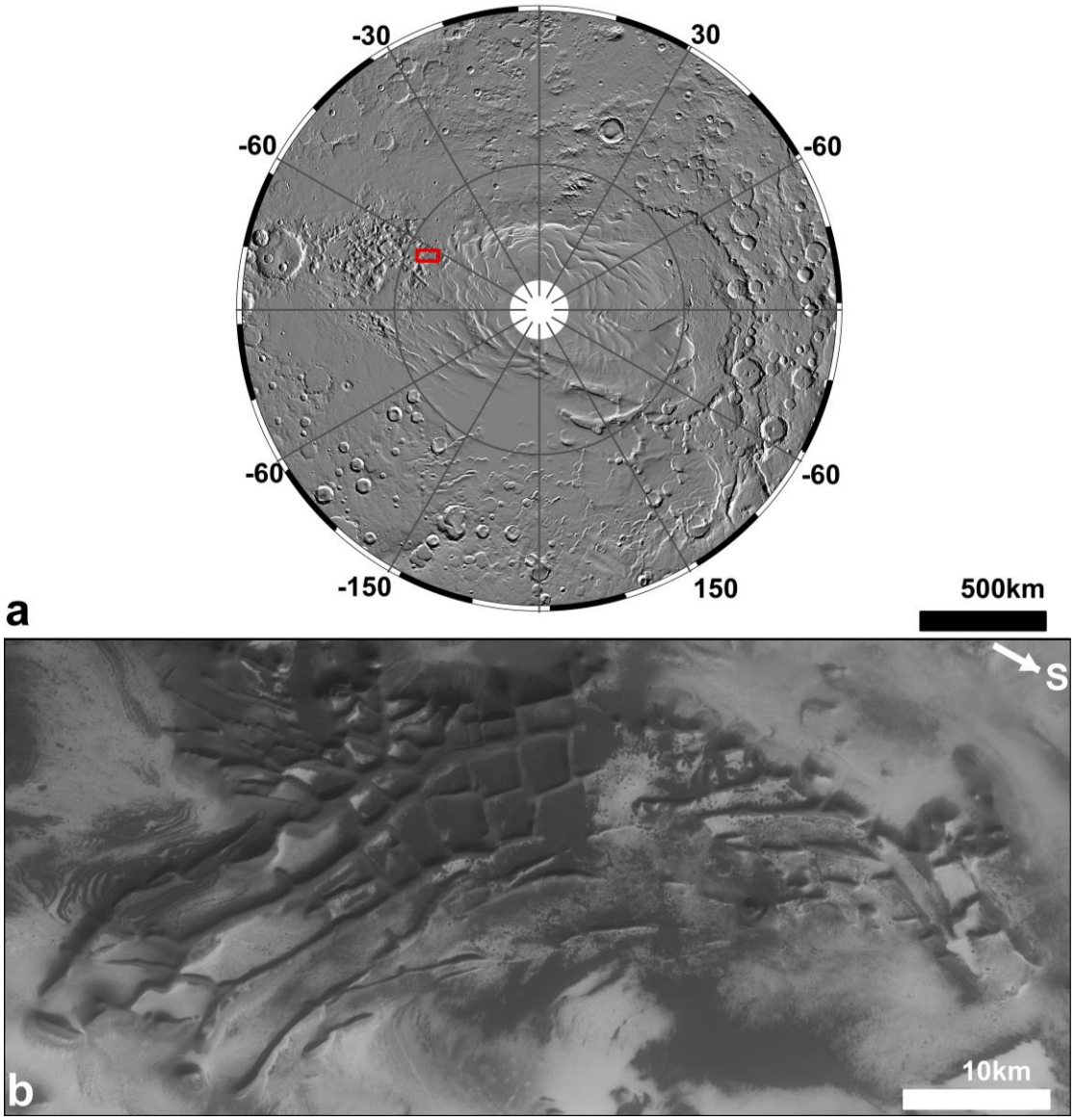

Figure 3.1 (a) The location of the Inca City region indicated by the red box shown in (b), superimposed on a MOLA hillshade with 463 m/pix (Smith et al., 2001b). (b) The close–up of the Inca City region. HRSC (Jaumann et al., 2007) image h6980_0000 is at a resolution of 25 m/pix.

3.3 Results

3.3.1 Types of spiders and their spatial distribution

In order to investigate the spider formation mechanism, I performed a spatial mapping of all spiders in the Inca City region using HiRISE images (McEwen et al., 2007). I mapped spider locations and characterised them based on topography and geomorphology, including central depression and trough morphology, trough spacing and orientation (radial or converging), spider distribution density, trough scale relative to central depression scale, trough tortuosity (for datasets and methods, please refer to Chapter II). Based on this analysis, I classified them into four types: fat, thin, elongated, and half spiders (Table 3.1). Fat and thin spiders correspond to those reported in Hansen et al. (2010); elongated spiders are newly classified; half spiders are reported for the first time in this work.

The distribution of four spider types is presented in Figure 3.2; they are located in relatively planar area confined by ridges (Figure 3.1), which is consistent with Hansen et al. (2010). Table 3.1 shows the classified types, dimensions, and trough widths of spiders. I did not observe any morphological changes of the spiders over the four Mars years' observation period. The counts in Table 3.1 have some uncertainties due to the data resolution constraints; some spiders may be connected by troughs or merged closely, so it is not always clear to determine whether the spiders are distinct individuals.

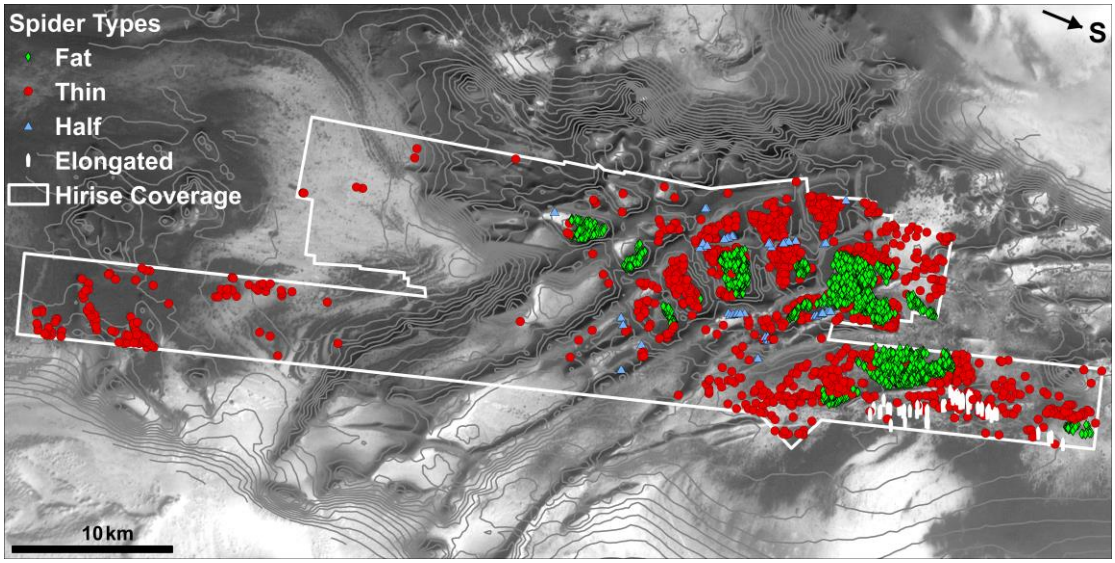

Figure 3.2 Spatial mapping of spiders in the Inca City region overlain a contour map with a contour interval of 50 m derived from MOLA. The white polygon indicates the area covered by HiRISE images. The background is HRSC (Jaumann et al., 2007; 2015; Gwinner et al., 2016) image h6980_0000. The legends with different colors and shapes indicate different types of spiders.

Fat spiders have quasi–circular central pits with diameters from ~25 to 65 m. Their troughs exhibit lengths from ~19 to 50 m and usually show a quasi–

wedge–shape with only few tributaries and the widths narrow away from central depressions significantly (Table 3.1). Troughs have roughly equal lengths in a given spider. Most of them resemble a star (Figure 3.3a). Fat spiders are rarely connected. They are commonly concentrated in clusters (Figure 3.2). Within two polygons of ~3.03 and 11.52 km^2 in area, ~578 and 909 fat spiders exist respectively, corresponding to densities of ~191 and 79 fat spiders/km^2.

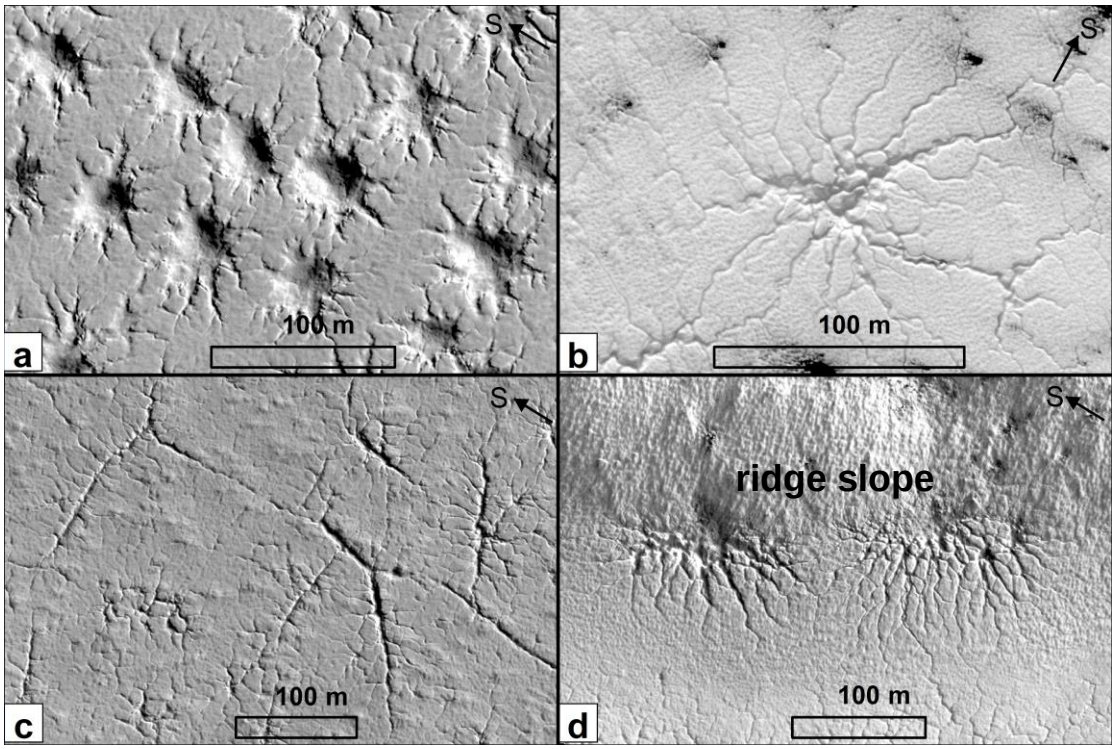

Figure 3.3 Four types of spiders. (a) A field of fat spiders, centered at ~81.62°S, ~296.39°E. HiRISE image PSP_005993_0985 was acquired at Ls=342 with 0.5 m/pix. (b) A field of thin spiders, centered at ~81.44°S, ~295.92°E. HiRISE image PSP_003928_0815 was acquired at Ls=247 with 0.25 m/pix. (c) A field of elongated spiders, centered at ~81.76°S, ~296.02°E. HiRISE image PSP_006204_0985 was acquired at Ls=351 with 0.5 m/pix. (d) A field of half spiders, centered at ~81.56°S, ~295.80°E. HiRISE image PSP_006204_0985 was acquired at Ls=351 with 0.5 m/pix. The upper part is the rising slope of a ridge, and the lower part is horizontal area.

Thin spiders are the most pervasive and common type in this area (Figure 3.2 and Table 3.1). They are characterized by rough central pits which usually have irregular shapes and radially organized dendritic troughs (Figure 3.3b). They are sometimes connected by troughs; it is thus hard to distinguish each individual spider. Thin spiders are variable in size (from ~50 to 500 m) and show various distribution densities (e.g., one region ~10 km^2 contains only one spider while another one ~5 km^2 hosts 72) through the Inca City region (Figure 3.2).

Elongated spiders are located only in one region centered at ~81.79°S, ~295.83°E. They are characterized by quasi–straight troughs emanating from frequently straight linear features which occasionally turn or bend with angles,

resembling centipedes (Figure 3.3c). The linear features are fairly constant in width varying from 3 to 5 m. In most cases, the emanating troughs are nearly parallel with one another. Because of the linear central features, I classify elongated spiders as a distinct species. Similar pre–existing linear features, with few troughs, were observed in this region as well.

Table 3.1 Types of spiders in this work

Type	Number (~)	Extent (~m)	Maximum trough width (~m)
Fat	2513	45–98	6–12
Thin	1044	50–500	3–7
Elongated	53	60–155	1.5–5
Half	59	50–110	3–8
In total	3669		

Half spiders appear with radially organized troughs but with only one half observable (Figure 3.3d). The diameter is from ~50 to 110 m. My observations show that half spiders are distributed along the boundaries of rectilinear ridges (Figures. 3.3d and 3.8a). Not all ridge boundaries host half spiders, but most of half spiders occur along ridge boundaries of quasi east–west direction and only one case was found along one ridge with south–north direction (Table 3.2).

Table 3.2 Approximate facing orientations of half spiders

Aspect of ridges	Numbers of half spiders	Number of Sun–facing	Number of Pole–facing	Notes
South–North	1	–	–	Sun–facing spiders are larger and more well–defined than ones on the other side of one ridge
Southeast–Northwest	12	5	7	
Northeast–Southwest	5	5	0	
East–West	41	22	19	
In total	59	32	27	

Parallel troughs are defined in this work as non–radial troughs with relatively even spacings and observed located only along north–facing ridge boundaries (Figure 3.4) not adjacent to half spiders. In Figure 3.4b, away from ridge boundaries, parallel troughs started to exhibit branching or dendritic form, I attribute this to variability of substrate properties and duration of erosion (Chapter 3.4).

3.3.2 Spatial randomness analysis

Spatial distribution has implications for understanding the properties of the underlying geological processes. Whether the spatial distribution of spiders is random or not can reveal if spider formation is controlled by a mechanism or it is rather a random process on the surface. Based on HiRISE (McEwen et al., 2007) observations, the spatial distribution of fat spiders appeared to be evenly spaced–more than expected for randomly occurring features. I selected a continuous population of fat spiders (Figure 3.5) for a rigorous analysis of spatial randomness. Other regions may show the effect to lesser extent: identification of the phenomenon even in one area, however, is pertinent to our understanding of the formation process.

The specific settings of Monte Carlo sampling in my work are: the sample area is a mapped polygon (~1.24 km^2 in area) with 365 sampling points (mapped spiders) as seen in Figure 3.5, which corresponds to the density of ~294 spiders/km^2 and the nature of the random spatial distribution is uniform.

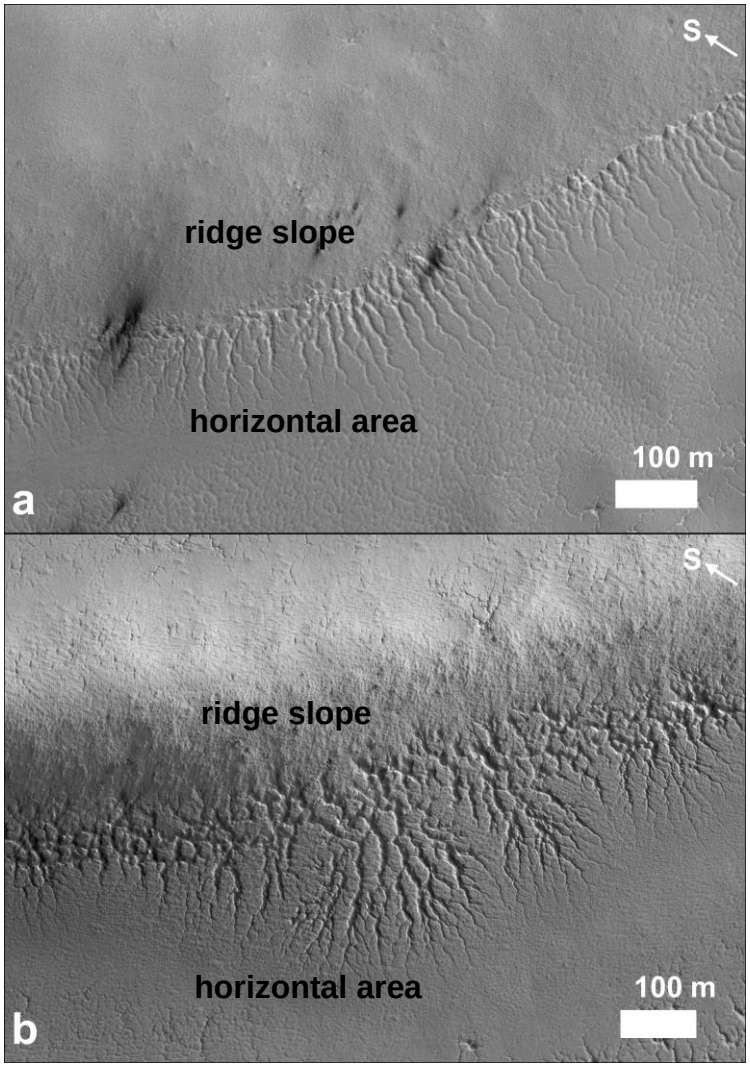

Figure 3.4 Parallel troughs along ridges. (a) centered at ~81.60°S, ~295.92°E. HiRISE image ESP_037626_0985 (Ls=173, 50 cm/pix); (b) centered at ~81.73°S, ~299.97°E. HiRISE image PSP_006204_0985 (Ls=351 with 50 cm/pix).

Figure 3.6 shows the result of our spatial randomness analysis and M2CND measurement with the lines connecting to each spider center's 2nd–closest neighbor (Figure 3.6). The M2CND value is 55 m which corresponds to the average spacing between spiders in the area and is discussed in Chapter 4.4. This value is plotted on the histogram computed from a series of 2000 M2CND values for random configurations in the same area. The M2CND value lies above the histogram at 9σ, indicating that the spatial configuration of the spider center's is more separated than random (Figure 3.6), or non-random.

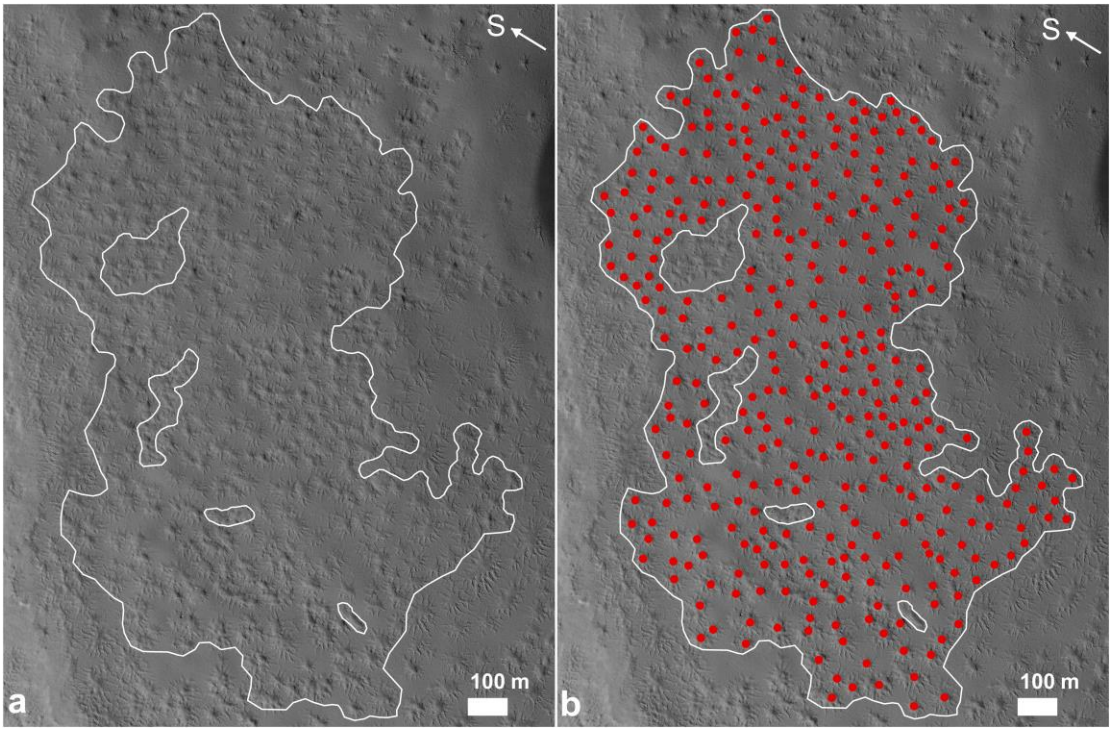

Figure 3.5 Fat spider population selected for spatial randomness analysis (centered at ~81.51°S, ~296.14°E). HiRISE image ESP_040185_0985 was acquired at Ls=295.60 with 0.25 m/pix. (a) The white polygon delineates the extent of the mapped area. The four inner polygons are the areas which were removed due to the irregular terrain. For details about mapping and analysis methods used in this study, please refer to Chapter II. (b) The red points show positions of fat spider centers.

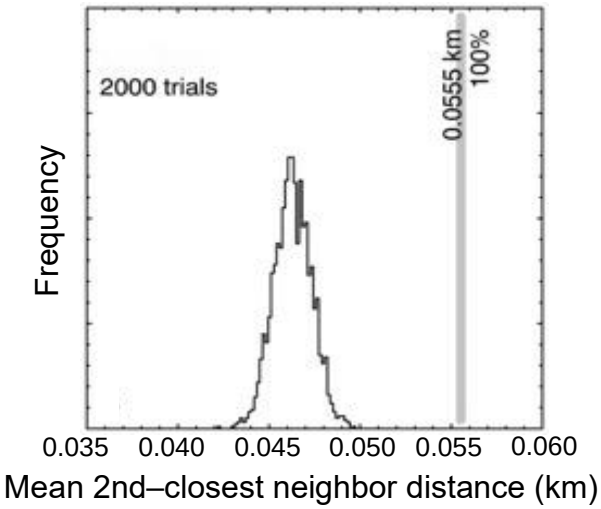

Figure 3.6 Spatial randomness analysis. M2CNDs (the histogram) for 2000 random configurations relative to the M2CND value (grey bar) of chosen observed fat spider population which lies 9σ above the histogram.

3.3.3 Statistics of spider location relative to ridge boundaries

Half spiders, in my study area, are observed along ridge boundaries. Half spiders could either be truncated resulting in the incomplete appearance of

spiders in morphology or form preferentially at the boundaries. If truncated, I would expect to observe partial spiders present in different fractions (e.g., 1/4, 2/4, and 3/4) with equal probability due to no preference of truncated fractions; if they form preferentially at the boundaries, I expect to see more 1/2 spiders (half spiders) than other fractions.

To assess probabilities of their occurrences, I surveyed spiders along ridge boundaries by recording and comparing numbers of these spiders in my work. According to their extent of incompleteness and degree of truncations, I categorized them into three cases: truncation within first 1/4, truncation within middle 1/2 (half spiders), and truncation within last 1/4 (Figure 3.7). For simplicity, I use terms “one quarter spiders” (or 1/4 spiders) and “three–quarters spiders” (or 3/4 spiders) to describe spiders of truncation within first 1/4 and within last 1/4. I identified in total 59 half spiders and no one–quarter spiders; among thin spiders, however, seven 3/4 spiders were identified (Figures. 3.8).

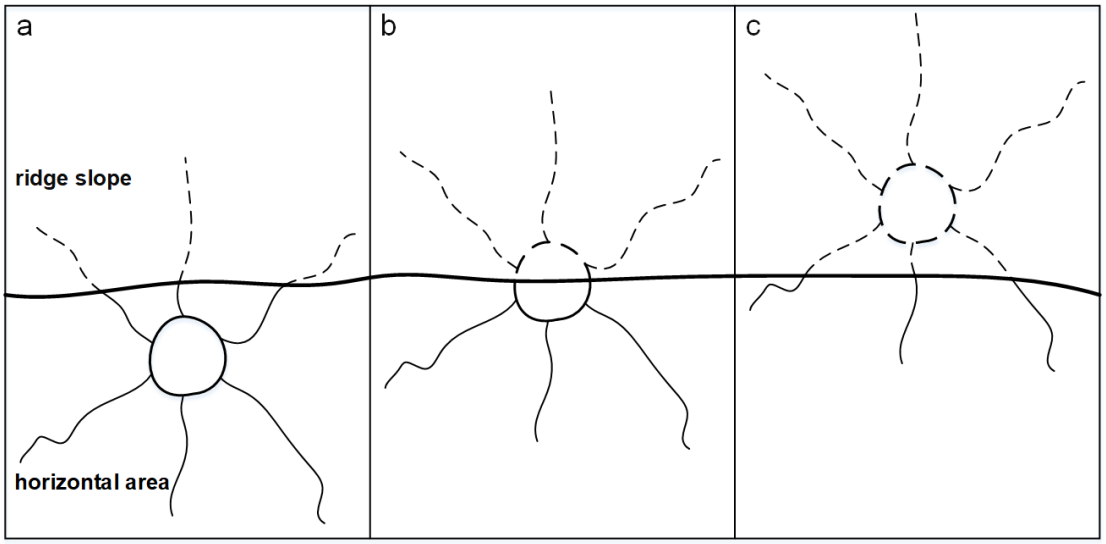

Figure 3.7 Categories of spider locations relative to ridge boundaries. The bold solid line indicates the border between the ridge and the horizontal area. The solid lines show spiders’ observable troughs which are located in the horizontal area. (a) spiders of truncation within last 1/4. (b) spiders of truncation within middle 1/2 (half spiders). (c) spiders of truncation within first 1/4.

The statistic results exhibit significant differences in quantity between half, 1/4, and 3/4 spiders. This suggests that half spiders are a distinct type with a particular forming mechanism (Chapter 3.4) rather than normal spiders cut or interrupted randomly by ridge boundaries. Otherwise, any of fraction truncation spiders should occur.

I surveyed the orientations of half spiders in the Inca City region and documented whether each half spider is sun–facing or pole–facing (Table 3.2). Spiders interrupted by sun–facing or pole–facing slopes receive differing

insolation, which possibly influences their development. North–facing half spiders acquire more sunlight than south–facing ones in the south polar area.

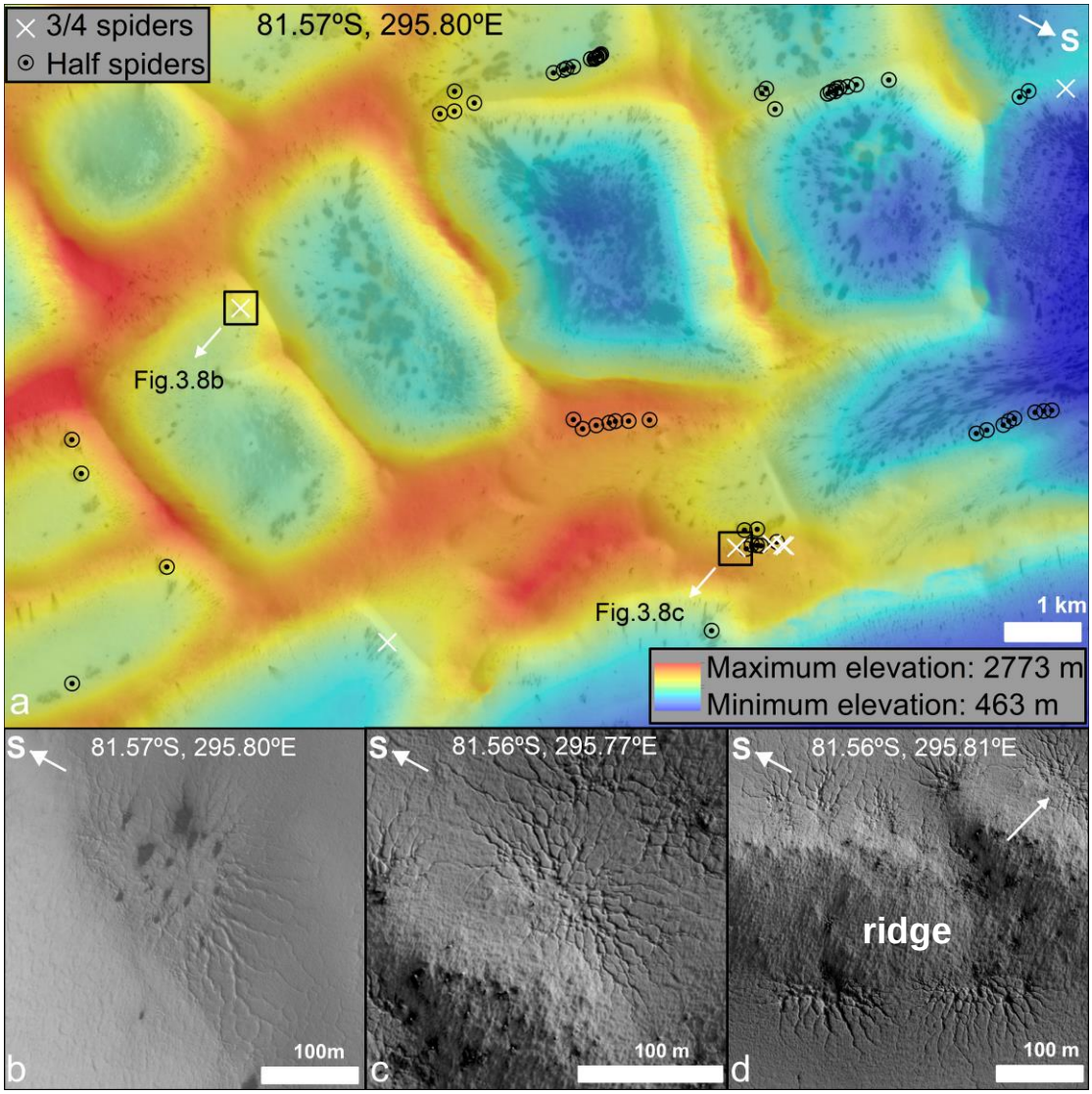

Figure 3.8 (a) Locations of 3/4 spiders and part of half spiders, superposed upon the color–coding elevation map derived from the CTX DTM (based on CTX images B07_012256_0985_XN and B08_012625_0985_XI). Black circles indicate the locations of part of half spiders, and white "×" show the locations of 3/4 spiders. Two black squares indicate 3/4 spiders in Figure 3.8b and 3.8c. The colors in the legend refer to elevations. (b) and (c) Two examples of 3/4 spiders. Backgrounds are HiRISE (McEwen et al., 2007) images ESP_011729_0985 and PSP_006204_0985, respectively. (d) A field of half spiders (Figure 3.3d), located on the two sides of one ridge. Background is HiRISE image PSP_006204_0985. South–facing spiders are relatively smaller in size and simpler poorly–defined in structure than the north–facing ones. The white arrow corresponds to Figure 3.8c.

The survey shows that more than half of half spiders in the Inca City region are sun–facing. I observed that along the same ridge, the south–facing spiders are relatively smaller in size and more poorly–defined in structure than the north–facing ones (Figure 3.8d), likely suggesting solar radiation differences will affect the morphological development of half spiders (Chapter 3.4).

3.4 Discussion

3.4.1 Spider formation process

The current understanding of spider formation rests on the hypothesis that gas produced by basal sublimation of seasonal CO_2 slab ice (Chapter 1.1) is trapped between the substrate and the overlying CO_2 ice. This gas, under growing pressure, escapes through weaknesses in the ice layer leading to gas–jetting (Kieffer, 2000, 2007; Piqueux et al., 2003; Hansen et al., 2010). I, however, suggest the seasonal CO_2 slab ice remains in contact with the substrate due to gravity and the underlying porous substrate, which is consistent with Pilorget et al. (2011). The translucent CO_2 slab ice allows solar radiation to pass through and warm the underlying substrate, which sublimes the base of the CO_2 ice and causes basal sublimation (Figure 3.8a). The gas created by basal sublimation disperses into the porous substrate, building pressure within the substrate (Figure 3.8a). Thus, substrate permeability /porosity and degree of cohesion are crucial parameters of spider erosion. This scenario of spider formation process is illustrated in Figures 3.9 and 3.10.

A rupture appears in the seasonal CO_2 slab ice when pressure within the substrate increases to some point (Figure 3.9b). The growth of a spider structure, formed through venting processes over many seasonal cycles, requires the vent recurs in essentially the same location. A possible cause may be the form of the deposited layer of CO_2 ice is influenced by the presence of the spider's central pit created by gas jetting, and this irregularity in the slab causes either a weakness leading to higher probability of rupture, or enhanced efficiency of basal sublimation due to the inclination of the upper surface of the ice towards the Sun or due to a lensing effect.

As the basal sublimation continues, the trapped gas migrates through the porous substrate towards the rupture along the pressure gradient (Figure 3.9b), accelerating as it passes out of the substrate into free air, and entraining particles which then settle onto the ice surface forming dark spots and fan deposits. As a result, a pit forms in the substrate (Figures. 3.9c and 3.10a). I suggest the pressure may build up within the substrate before the rupture, and the CO_2 ice layer may experience this pressure from beneath without the need of separation between ice and substrate. After the rupture occurs, gas escapes from the pit walls and the spider channels connecting to the pit, which drives more jetting.

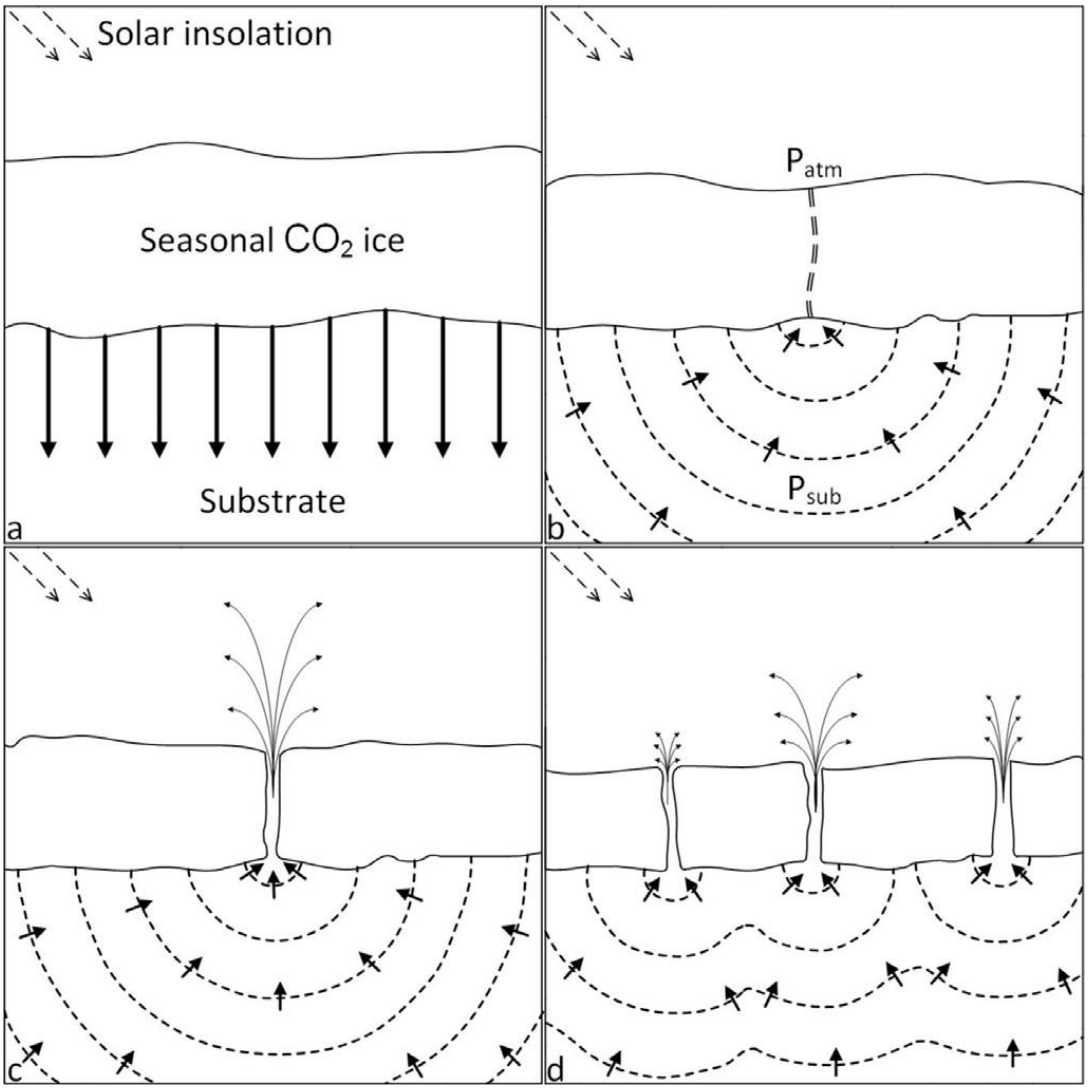

Figure 3.9 The schematic of spider formation. (a) Solar insolation penetrates the translucent CO_2 ice heating the substrate, which warms the base of the CO_2 ice leading to basal sublimation. The sublimating gas is trapped within the substrate. (b) The pressure ruptures the seasonal ice. (c) Due to the low atmosphere pressure, gas eruptions result from pressure gradient between P_{atm} and $P_{sub,}$ leading to rapid escape of gas entraining substrate material and forming a cavity. (d) Beyond a certain distance away from the jet, the rate of lateral flow becomes lower than the local rate of accumulation from basal sublimation. Thus, a new rupture occurs. Below this distance, the local lateral flows act to inhibit accumulation of sufficient pressure to cause a rupture initiating a new spider. The black arrows indicate the pressure gradient. The dashed lines indicate an approximate schematic illustration of pressure gradient contour line. P_{atm} is the pressure of atmosphere, P_{sub} is the pressure inside the substrate.

The pit formed in the substrate has most likely random protrusions in shape. Weaknesses at the substrate–atmosphere boundary may lead to small–scale collapses which enhances the entrainment (Figure 3.10b). Any radial asymmetry in the substrate–atmosphere boundary (Figure 3.9c) will change the

pattern of gas flow through the substrate (Figures 3.10b, c, and d). I expect the flow will be diverted towards any prominence in the evolving eroded depression, which will enhance growth in the prominence and reinforce the irregularity (Figure 3.10d). I suggest this may be the mechanism which leads to the growth of spider 'legs' or troughs (Figure 3.10). The erosive force of the escaping gas is dependent at each point on the substrate accumulating area, allowing gas to escape at that point. The erosive force is maximum where the legs are maximally separated (increasing the likelihood of branching), and likely greater at the extremities than near the center. When the extremities approach those of a neighboring spider, the pressure accumulation becomes shared and split, weakening the erosive force, and thus causing the spider growth to slow down. This furthermore explains why the legs are roughly evenly spaced from one another. For the same reason, I expect that in the vicinity of one spider, the dispersed pressure should inhibit the initiation of a new spider. In other words, the formation of one spider influences the vicinity in such a way that another spider is less likely to occur within a certain distance (inhibited zone).

I have shown that fat spiders are on average more separated than a random spatial configuration (Chapter 3.2 and Figure 3.6), which is consistent with our hypothesis of the formation mechanism. I think, however, that all types of spiders share a similar formation mechanism and their differences arising from the substrate properties (i.e., permeability/porosity and cohesion; Chapter IV). I acquired a value of 55 m from the randomness analysis of a fat spider population which possibly indicates the size of the inhibited zone in our randomness analysis (Figure 3.6). However, I expect that this value is closely associated with substrate permeability/porosity and varies from region to region.

During spider formation, all ruptures are considered to begin with a minimal vent aperture. At time of rupture, the vent is very small, and jetting can only be maintained while there is a strong pressure difference above and below the ice. Later in the season when the ice has retreated to the boundary of the pit, I expect the pressure gradient to be greatly reduced because of the broad exit paths. I suggest the size of the pit relates to how many cycles of jetting have occurred. I do not believe that a large pit necessarily indicates a large jet, the reasons are explained in the following. Jets initiate at a fracture and their power should be determined by the area of ice providing sublimating CO_2 to the jet. Thus, I treat all spider centers as causing an equivalent release of pressure at the time of rupture or, at least, a value uncorrelated with the pit diameter. A jet, when it occurs, causes a local reduction of pressure in the substrate, and the range of this effect is determined by the substrate permeability/porosity. Thus, the cross–sectional area of the pit may not correspond to the size of the vent during jetting. Although I recorded the diameters of the spider central pits in the spatial randomness analysis, corresponding to measurements of crater diameter, this data was therefore not used in the further analysis.

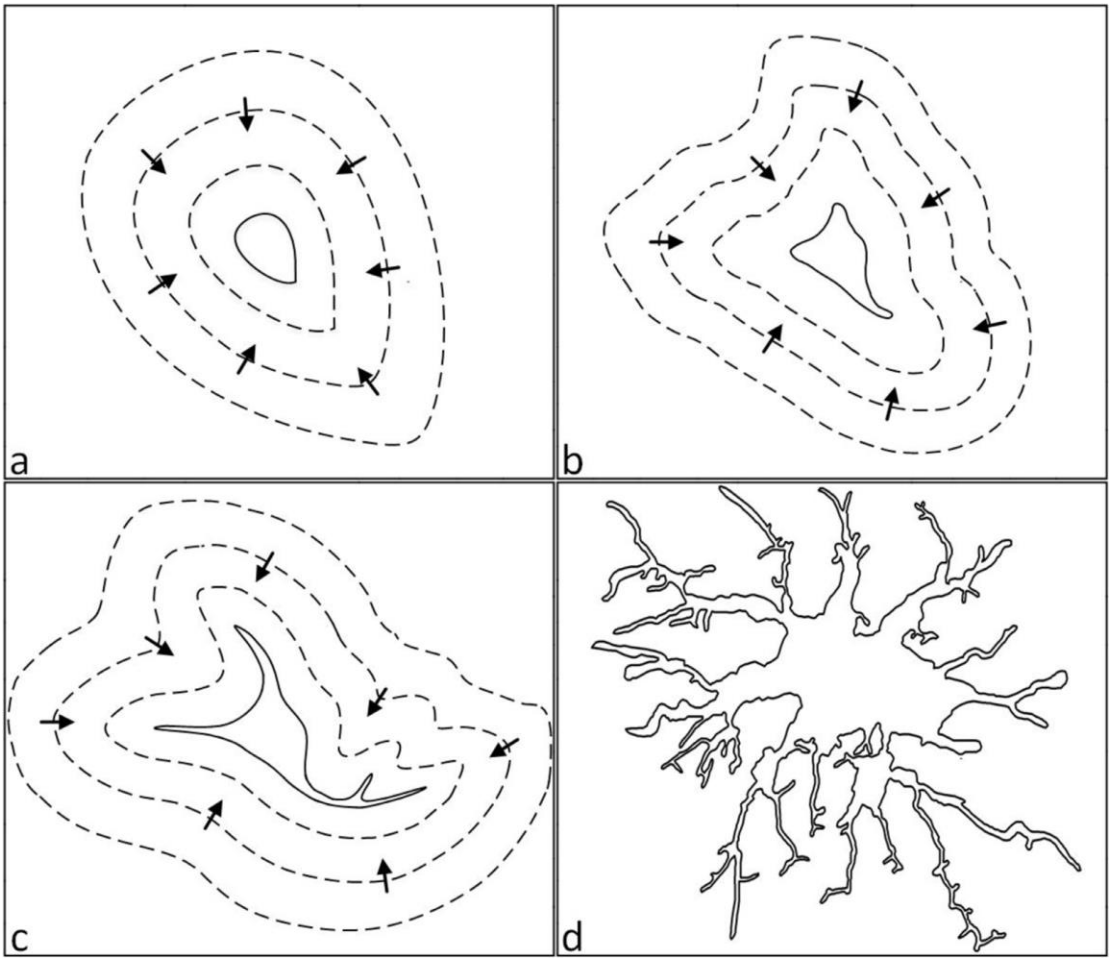

Figure 3.10 The schematic of spider erosion. (a) Gas migration and eruption shown in Figure 9b, c, and d create a pit in the substrate. Collapse at substrate–atmosphere boundary may initiate irregular prominence in a pit. (b) and (c) Pressure gradient diverts gas flow preferentially towards any prominences of a pit, enhancing irregularity, and leading to growth of a trough. (d) After repetitions of seasonal cycles, the above processes eventually result in radiating dendritic troughs, (d) shows a mapping of a real spider in our study area. Note roughly even angular spacing of radial troughs. Black arrows indicate pressure gradient, and dashed lines indicate approximate pressure contours.

When the gas migrates to the vents, the substrate–pit boundary is apt to collapse. Remaining sharp prominences of the substrate are prone to collapse, favoring growth of the pit rather than the carving of long troughs. I, therefore, interpret that one possible reason for fat spiders' short troughs with few tributaries possibly is low cohesion of the surface material.

As discussed above, I suggest that spider growth results from micro–collapses caused by escape of CO_2 from the porous substrate into the spider troughs. Escape occurs both from the trough walls and from the trough floor. Escape from the walls allows material to collapse from the wall to the floor (with a small quantity being entrained in the gas flow to escape through the jet). Escape from the floor cannot induce any collapse, but only entrains a small amount into the

flow. Thus, the growth occurs only along the free surface, and the growth of a downward– directed trough is inhibited by self–infilling.

Elongated spiders are easily recognized by central linear depressions, which I suggest to be formed upon pre–existing features produced by different geological processes, such as thermal contraction mechanisms. The linear depressions offer a ready–made path for gas migration towards a vent (Figure 3.11). Some linear depressions with sparse troughs could express an early stage of elongated spider formation (Figure 3.11).

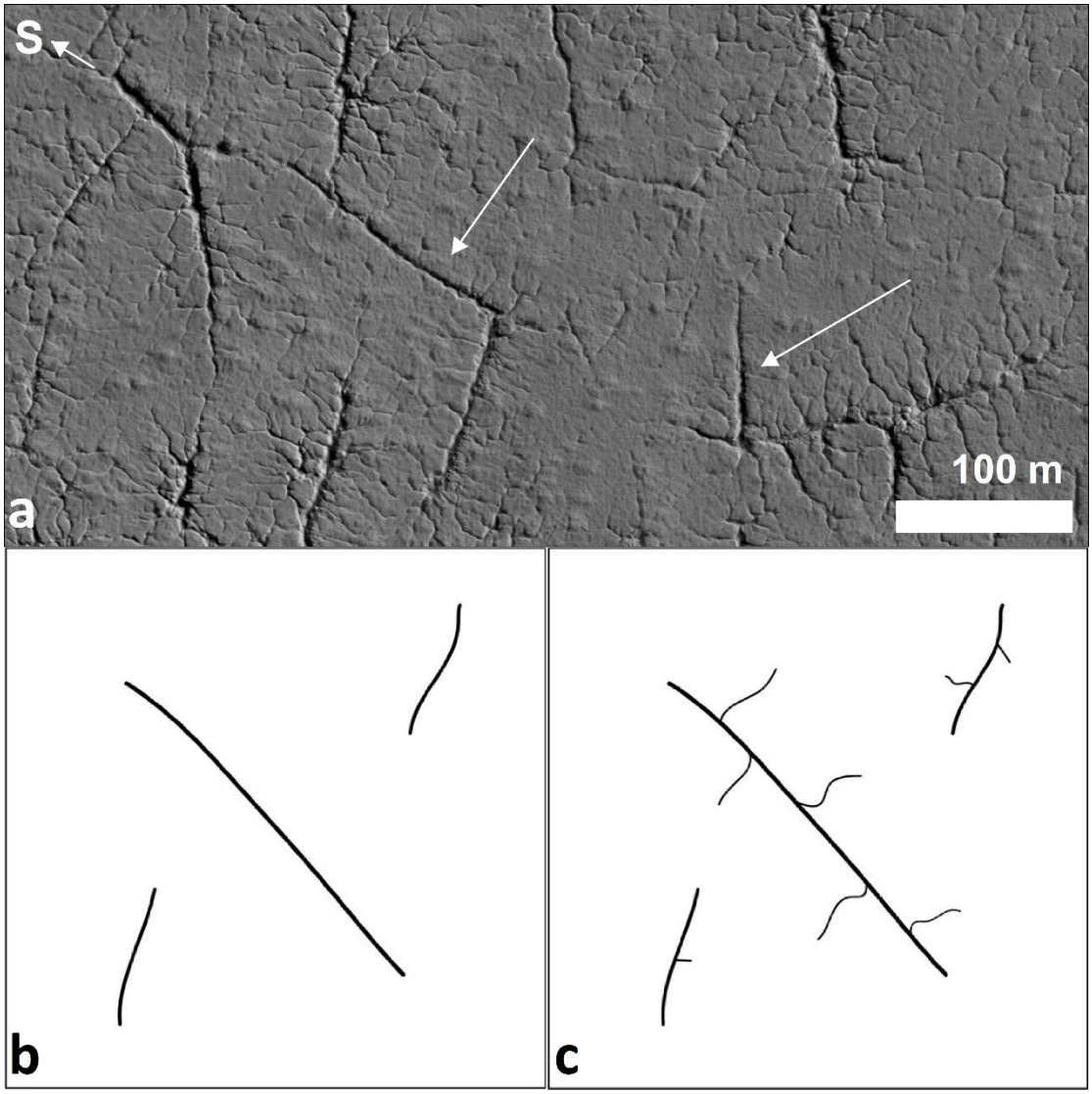

Figure 3.11 Elongated spiders and the formation process. (a) Pre–existing linear depressions in the substrate which may provide a path for spider erosion. White arrows indicate pre–existing depressions possibly undergoing spider erosion. HiRISE (McEwen et al., 2007) image PSP_006204_0985 was acquired at Ls = 351 with 0.5 m/pix, centered at 81.76°S, 296.01°E. (b) Pre–existing depressions exist before spider erosion. (c) These depressions provide paths for gas migration as well as a preferential site for ice rupture. Bold black lines indicate pre–existing depressions; slim black lines indicate troughs due to spider erosion.

Piqueux and Christensen (2008) observed in the Manhattan region (86°S, 95°E) that some spiders may be connected with polygonal networks by troughs. The authors suggested that these polygonal networks share the same origin with spiders and result from substrate erosion of confined gas between the substrate and seasonal ice layer. In our study area, the linear features may have, alternatively, played the same role as the polygonal networks as suggested by those authors. However, I observed linear depressions with few or sparse troughs in the Inca City region which may present an early stage of elongated spiders. I interpret these linear depressions' formation to be unlikely related to the basal sublimation process, and they were formed by a different mechanism (e.g., thermal contraction), and then spider erosion initiates later.

Half spiders occur along the boundaries of ridges, which suggests the break in topography influencing the level of absorbed solar radiation may play a role in their formation. Tilted ridge and flat ground regions receive differing insolation resulting in a temperature discrepancy (Figure 3.12). A warmer slope surface produces a higher local pressure in the substrate, generating a gas flow towards the neighboring flat region. This may enhance the initiation of jetting near the boundary. Additionally, the difference in material properties (e.g., permeability/porosity) between the ridges and flat region exerts an influence. The ridge material is possibly more consolidated with lower permeability/porosity thus leading to the local pressure rising faster than in the flat area. It appears likely the more consolidated material of the ridges prevents the growth of spider “legs” up the slopes. If the ridge material is less consolidated with higher permeability/porosity, spider troughs may form on slope surface, but I do not have such observations. One possible reason is that slopes result in collapses of troughs which prevents their formation (Hansen et al., 2010), or insolation difference is the more dominant reason. All of these together could explain why spiders initiate preferentially along the boundary, producing the separate class of half spiders. At the north pole, on the other hand, the topography–break gives rise to weaker ice at the boundaries, responsible for formation of weak spots on the crests of dunes (Hansen et al., 2013). I, however, have not observed spiders on the ridge slopes. From the formation mechanism, elongated and half spiders could be seen as deviating species from thin spiders.

I found 7 three–quarters spiders (e.g., Figures 3.8b and 3.8c), zero one–quarter spider, and 59 half spiders supporting the idea that spiders are not randomly truncated but their formation process is controlled by slope of ridges which affect received solar insolation. The few three–quarter spiders may be fragments resulting from low insolation angle or insufficient image resolution. The greater numbers and generally larger size of north–facing (sun–facing) half spiders compared to south–facing (pole–facing) ones (Figure 3.8d) indicate that more sunlight causes more intensive erosion. Therefore, my statistics of spider

location relative to ridge boundaries (Table 3.2) confirms my hypothesis that half spiders form preferentially on the boundary rather than being randomly truncated features. Had they been randomly truncated, I would expect roughly equal numbers of 1/4 spiders, 3/4 spiders, and half spiders.

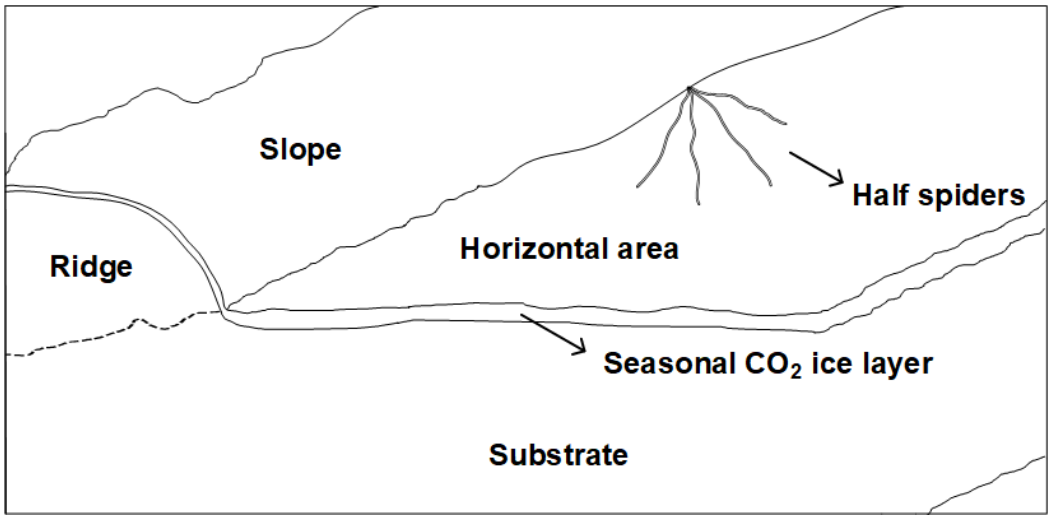

Figure 3.12 A schematic drawing which shows half spiders' initiation locations (Figure 3.3d). Half spiders are initiated along ridge boundaries. The ridge area may have different material properties from the substrate. The physical representations in this graph are not expressed in real proportions.

I observed parallel troughs emanating along the boundaries of ridges (Figure 3.4). I attribute their formation to the same mechanisms as half spiders, but with more frequent ruptures occurring along the ridge. I suggest that inhibited zones around developing troughs cause the growth of neighboring troughs to remain parallel. A deviation in growth brings a path closer to a neighbor on one side, which leads to diminished accumulation area and thus pressure on that side and the opposite on the other side. In combination, this pushes the growth to revert to a parallel path. Variability of substrate material properties (e.g., permeability/porosity) as well as duration of erosion leads to diversity in extent, spacing, and dendritic or parallel form of the troughs (Figure 3.4a and 3.4b). The homogeneity in substrate material properties leads to inhibited zones of similar sizes. For the quasi–parallel troughs (Figure 3.4a), with high degree of homogeneity in the substrate material properties and dense initial venting spots along the ridge boundaries, the inhibited zones of troughs cause a single direction growing, with few bifurcations; if the substrate is not homogenous, troughs would develop bifurcations because of differing (Figure 3.4b) inhibited zones. It is also possible the substrate properties are homogeneous near the ridge boundaries and gradually become heterogeneous away from the ridge leading to bifurcations, resulting in troughs that are originally parallel and later dendritic. I observed that parallel troughs only occur on the north–facing sides of ridges, which supports that more abundant sunlight in north–facing sides triggers more basal sublimation and gas eruptions leading to more active

surface erosion. Another possibility is that parallel troughs may be results of retreating erosion by CO_2 gas jetting initiated at the insulated ridge slope and the morphologies are similar to the one shown in Figure 3.7c. The central pit and other parts of the troughs were possibly removed by collapses. However, so far, I do not have observations of spiders or troughs on ridge slopes.

While spiders have been studied for decades since their identification (Kieffer, 2000), few morphological changes have been observed with current observational capabilities (Portyankina et al., 2017). This indicates that spiders' troughs in the Inca City region have grown less than 0.75 m (the spatial resolution of HiRISE image is 0.75 m/pix) in length during the last 11 years of the HiRISE observations or they do not grow. Portyankina et al. (2017) reported the occurrence of new troughs located at ~70°S, 178°E and ~74°S, 352°E with active growth from MY 30 to MY 32, which could be early–stage spiders. I expect that pre–existing linear features in the elongated spider location region undergo present–day spider formation as well, but there is only one HiRISE image in this region which restricts my investigation of their evolution.

3.4.2 Spatial distribution characteristics of spiders

Piqueux et al. (2003) mapped all spiders in the south polar area using MOC images (Kieffer, 2000) and pointed out the Inca City region hosts an elevated density of spiders. With the improved spatial resolution of HiRISE images, Hansen et al. (2010) performed a detailed study of surface erosion features in two locations, the Inca City region and the Manhattan region, and suggested a classification of erosional features including spiders. The increased observations by HiRISE images of the Inca City region since 2010, provided an opportunity of investigating the spiders' spatial distribution in more detail.

Based on the two dominant factors and criteria in our classification work, the geomorphology and topography, I classified four types of spiders (Figures 3.2 and 3.3). Most spiders are concentrated in the internal polygon–like regions enclosed by ridges shown in Figure 3.2, which implies these "block" regions are very active in CO_2 sublimation and gas jet driven activity that provides conditions for spider formation (Hansen et al., 2010). Hansen et al. (2010) suggested that spiders are rarely located on slopes of ridges which may be a consequence of slope collapse in the region.

Spatial randomness analysis shows that fat spider's spatial distribution is more ordered (Figure 3.6) indicating it is not randomly distributed. This is consistent with the spider formation mechanism I proposed. Fat spiders rarely overlay each other, which could be explained by the existence of inhibited zones inhibiting possibilities of intersecting troughs of neighboring spiders. This lends further support to our hypothesis on spider formation. In one location (84.44°S, 295.92°E), fat spiders are adjacent to thin spiders but do not overlay each other. This likely results from the different substrate material properties (e.g.,

permeability/porosity and cohesion) which affect the resistance of the substrate to spider erosion and is in agreement with Hansen et al. (2010). High cohesive substrate allows spiders to form longer troughs without collapses, thus regions with thin spiders likely have a more cohesive substrate than those of fat spiders. Low cohesion and thus high permeability/porosity induce relatively smaller resistance but susceptible to collapse, which could explain smaller spacing within fat spiders. Local homogeneity of the substrate properties could be responsible for the continuous distribution of fat spiders.

Elongated spiders are concentrated in one area (Figure 3.2) where I observe the presence of linear features with few “legs” or little spider erosion thus being likely pre–existing. Half spiders are located at the boundaries of ridges (Figure 3.8a). They appear to emanate from central points which are located on the boundaries of the ridges. Such a configuration would suggest the boundary influences the initiation of spider formation, providing a preferential site for rupture of the ice cover.

3.5 Conclusions

Based on my observations using HiRISE images (McEwen et al., 2007), I classified spiders in the Inca City region into four types: fat, thin, half, and elongated spiders, the latter two are newly–reported (half) and newly–classified (elongated). Spiders in the Inca City region are generally distributed over regions enclosed by ridges (Hansen et al., 2010; and this study). The spatial locations of half and elongated spiders are concentrated in certain limited regions where ridges and pre–existing linear features play a role in their formation process. Half spiders are initiated along ridge boundaries due to an assumed contrast in substrate properties in combination with the differing insolation on the ridge slope and horizontal area, which is supported by my statistics results of spider location relative to ridge boundaries. I argue this qualifies half spiders to be a distinct type.

I propose a spider formation mechanism, detailing the mechanism of growth of central pits and radiating troughs, and explaining some elements (e.g., trough length) of their morphology. I interpret spider features to show that gas disperses into and pressurizes the porous substrate, in comparison to the postulate of Kieffer (2000 and 2007) that the pressurized gas is confined between the seasonal ice layer and the ground. Spider erosion is triggered by a rupture in the overlying CO_2 ice layer leading to gas jetting. I suggest it is the gas escape from the substrate through rupture of the ice layer, entraining material at the substrate–free space boundary that produces the characteristic forms of spiders. The pressure gradient established around a spider leads to preferential growth of the “legs” or troughs and is responsible for the spacing between legs. The presence of a spider structure inhibits the initiation of a new spider in its vicinity by diminishing the local pressure beneath the ice cover.

Only beyond a certain range, the rate of flow towards the spider's vent(s) can be exceeded by the influx from basal sublimation; at this range, a new rupture and consequent spider erosion can occur. The permeability/porosity and degree of cohesion of the substrate are significant parameters controlling the mechanism of spider formation. The spatial randomness analysis reveals that initiation locations of spiders are more separated than a random distribution or non–random, which is consistent with the proposed spider formation model. My findings on fat, elongated, and half spiders, which deviate from thin spiders, indicate that topography and substrate mechanical properties play important roles in spider formation.

Chapter IV. Variability of spider spatial configuration at the Martian south pole

This chapter is about investigation of the variability of spatial configuration for spiders and their troughs at seven study regions. The key points of this chapter are: (1) Non–random spatial distributions are reported in seven study regions; (2) A regional variation of spider spatial configurations is reported; (3) Spider trough orientation mappings show that orientations of spider troughs appear to be random; (4) Influencing factors for spider spatial configuration and formation are proposed.

The content of this chapter is accepted as "*Hao, J., Michael, G., Adeli, S., Jaumann, R., Portyankina, G., Hauber, E., Millot, C., Zuschneid W., 2020. Variability of araneiform spatial configuration at the Martian south pole. Accepted at Planetary and Space Science (In Press), https://doi.org/10.1016/j.pss.2020.104848*". I performed spatial mappings for the study areas. I interpreted and discussed results and concluded the work. At the preparation stage of the manuscript, all co–authors were consulted. For the introduction of datasets and methods, please refer to Chapter II, part of the introduction of this paper was merged into Chapter I and Chapter 3.1. Other parts of the paper are presented here, I added additional explanations for several issues for better clarity.

4.1 Introduction

Spiders are observed to be unique to the south pole (Hansen et al., 2013; Bourke, 2013; Portankina et al., 2017). One possible reason may be the substrate material in the south polar area which is cohesive and thus able to sustain the spider morphology, unlike the large–area non–resistant sand dune material at the north pole that does not allow spider erosion (Piqueux et al., 2003; Portyankina et al., 2019; Hao et al., 2019). Another reason may be the dominant water ice which is a more erosion resistant surface of the north pole (Brown et al., 2016). It is also likely due to the difference in CO_2 deposition, with snow–like deposition in the north resulting in small grain sizes and non–translucence, and vapor deposition in the south with CO_2 slab ice formation (Smith and Zuber, 2018). The shorter and hotter summer in the south may also contribute because of the more extensive CO_2 ice condensation. In the nearby south polar residual ice cap, the heavily eroded CO_2 ice substrate hosts widespread pits and scarps surrounding which transient bright "halos" were observed (Becerra et al., 2015). The appearance of these halos was closely related to the dust storm that occurred in Mars year 28. Dust settling down would be deflected away from the edges of the pits and scarps by local winds that were induced by local pressure differences caused by relatively higher CO_2

summertime sublimating rates on the slopes. This relative enhancement of the local albedo by the “non–settling” of the dust would be responsible for the observed “halos” (Becerra et al., 2015).

When spiders were first identified, Kieffer (2000; et al. 2000) suggested, and it was later confirmed by Piqueux et al. (2003), that most spiders were only located within the cryptic area (Figure 1.7; Chapter I) due to the existence of a seasonal translucent CO_2 slab ice. Later researchers reported that some regions outside the cryptic area also host spiders (Hansen et al., 2010; Schwamb et al., 2017; this thesis). These do not contradict the work by Kieffer (2000) and Piqueux et al. (2003). As discussed in Chapter III, spider formation is triggered by basal sublimation of the translucent of CO_2 slab ice. The limited spatial resolution and areal coverage of available data at that time (Piqueux et al. (2003) and Kieffer (2000) used CTX and TES) restricted the findings of small–area CO_2 slab ice and more spiders (Chapter I).

The south polar layered deposits (SPLD) are suggested as the major geological host unit for spiders due to their unconsolidated substrate material (Piqueux et al., 2003; Chapter I). However, newly–reported observations of spiders expanding host geological units to “Early Noachian highland unit” and “Hesperian polar unit” (Schwamb et al., 2017) and radial growth of troughs in the vicinity of dunes and crater rims around ~70°S (Portyankina et al., 2017) outside SPLD, have demonstrated alternative candidate locations for spiders. This suggests a variety of settings where spiders can form, as well as variability in the conditions for gas jetting. Often, spiders are observed occurring in groups (Piqueux et al., 2003; Hansen et al., 2010; Hao et al., 2019), and one spider group was reported to exhibit non–random spatial configuration (Hao et al., 2019). My motivations of this chapter are to investigate whether local spatial configurations of spiders have regional variation which should be related to regional variability in spider formation, gas jetting, and substrate properties, and what are the constraints on the spatial configuration. In order to do so, I selected seven study regions at the south pole, mapped their spider spatial distributions, and analyzed each region’s spider spatial configuration. This chapter’s work yields a further understanding of spider formation–one of the key polar processes, and thus to infer past and current climatic conditions of Mars.

4.2 Study area

Based on the availability of HiRISE images (McEwen et al., 2007) with visible spider morphologies, I selected 7 study regions at the south pole labeled from A to G (Table 4.1; Figure 4.1). Note that region A is the study area in Hao et al. (2019). The spider population in each region are shown in Figure 4.1.

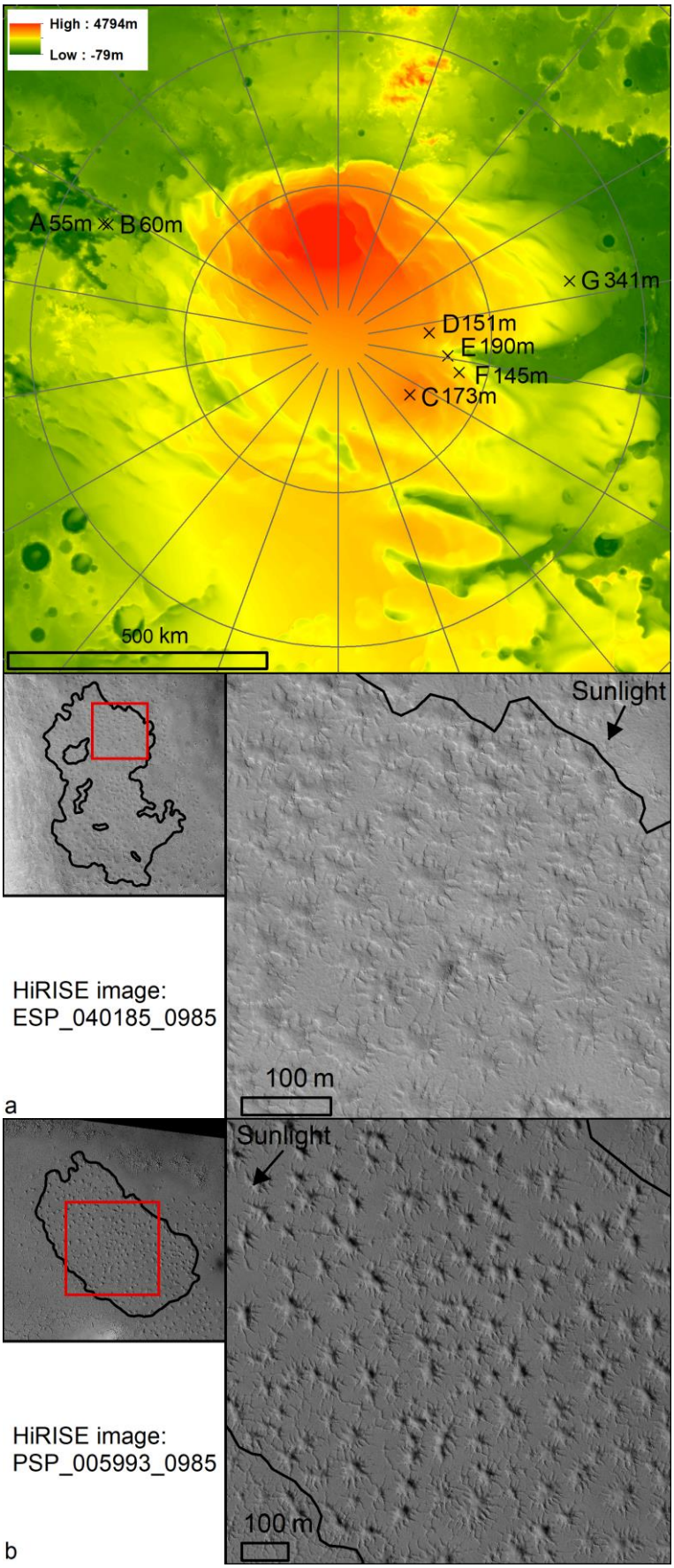
High : 4794m
Low : -79m
A 55m
B 60m
G 341m
D 151m
E 190m
F 145m
C 173m
500 km
Sunlight
HiRISE image:
ESP_040185_0985
100 m
a
Sunlight
HiRISE image:
PSP_005993_0985
100 m
b

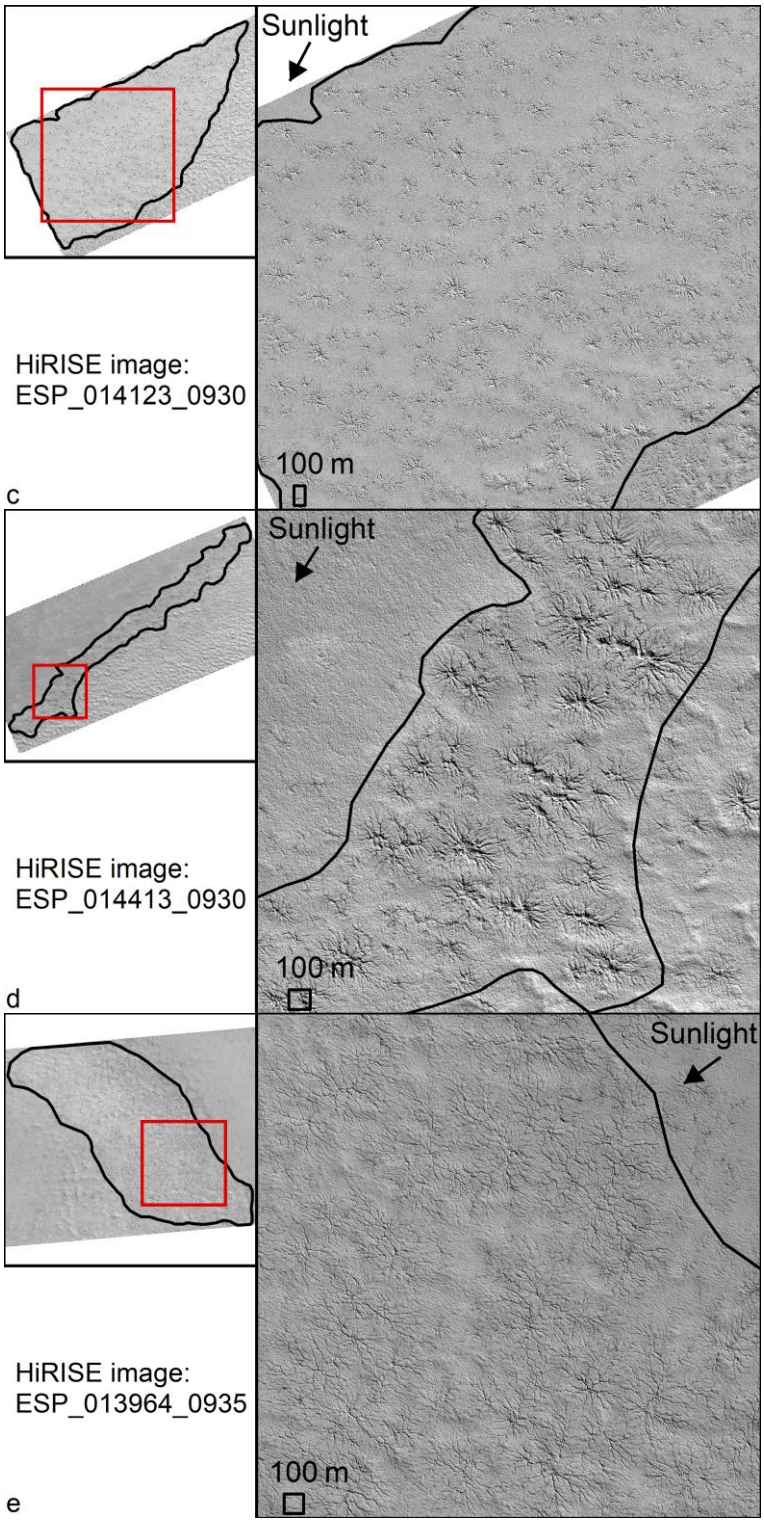
Sunlight
HiRISE image:
ESP_014123_0930
100 m
c
Sunlight
HiRISE image:
ESP_014413_0930
100 m
d
Sunlight
HiRISE image:
ESP_013964_0935
100 m
e

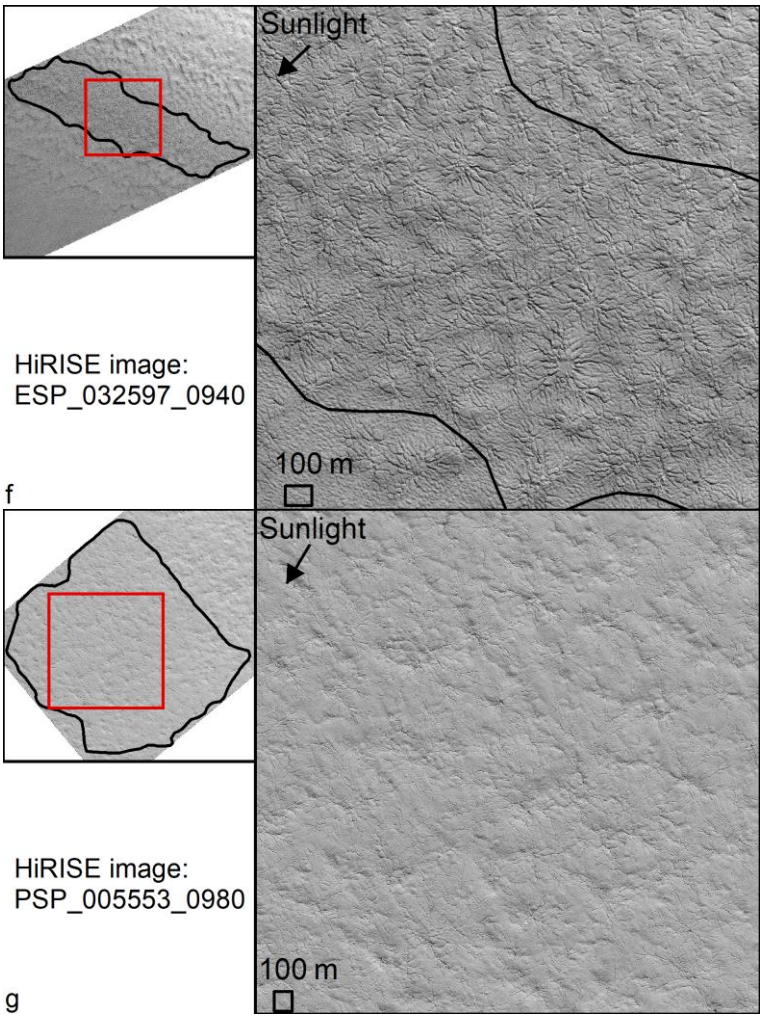

Figure 4.1 Geographical locations and surface details of the seven study regions. The color image shows seven study regions' geographical locations. The numbers after region names indicate the average spacing (M2CND) between spiders. Background is 115 m/pix MOLA DTM. Lines of latitude and longitude are noted every 5° and 20°. Subframes a ~ g correspond to the seven study regions A ~ G. The black lines delineate the extent of each region. The left panels are overviews of each (mapped by black lines) spider population. The right panels are close–ups of spiders indicated by red squares in the left panels.

Regions A and B are located in Angustus Labyrinthus (dubbed "Inca City"; Chapter III) which are characterized by intersecting ridges and polygonal internal areas (Sharp, 1973). Regions C, D, E, F, and G are located inside the cryptic area (for the location of the cryptic area, please refer to Figure 1.5; Paige and Keegan, 1995; Kieffer et al., 2000; Langevin et al., 2007; Brown et al., 2010). This cryptic area was observed to host intense gas jetting (Kieffer, 2000; Kieffer et al., 2006; Hansen et al., 2010). Regions A, B, and G sit at much lower elevations (~ 2 km) than those of regions C, D, E, and F (Table 4.2). The distinctive local environments of these regions (Figure 4.1) provide a unique opportunity to investigate their links with spider morphologies and the variability of spiders' spatial configurations.

Table 4.1 List of regions selected in my work of this chapter

Region	Area (km^2)	Spider observed number	Lat (°S)	Lon (°E)	HiRISE image ID
A	1.26	365	81.50	296.15	ESP_040185_0985
B	1.62	373	81.65	296.33	PSP_005993_0985
C	29.60	700	87.03	127.87	ESP_032597_0940
D	14.60	430	87.01	86.42	ESP_014413_0930
E	22.50	386	86.38	98.98	ESP_014123_0930
F	7.23	301	85.91	105.60	ESP_013964_0935
G	20.62	142	82.24	76.06	PSP_005553_0980

Table 4.2 Measurements at the seven study regions

Region	M2CND (m)	Elevation[*1] (m)	Average slope (degree)	Mean spider size (km^2)	Water ice content[*2] (%)	Thermal inertia[*3]
A	55	1822	1.36	0.00229	33.02	74
B	60	1748	0.63	0.00297	33.02	102
C	173	3730	0.37	0.02460	49.92	–
D	151	3467	1.14	0.03602	48.81	–
E	190	2978	2.01	0.04422	49.42	65
F	145	3035	1.40	0.01820	44.94	90
G	341	2132	0.50	0.12266	38.28	78

[*1] Average elevation and slope for each region were extracted by ArcGIS software.

[*2] Pathare et al., 2018.

[*3] Putzig and Mellon, 2007. Thermal inertia here is dayside.

4.3 Results

The results of spatial randomness analysis are presented in Figure 4.2. I find the M2CND (average spacing between spiders marked on the gray bar in Figure 4.2) lies near or beyond the upper extreme of the simulated histogram in each region. This indicates that spatial configurations of spiders in the seven study regions are non–random (Hao et al., 2019; Chapter III).

The average spacing (inter–spider distances) of spiders differs strongly between the study regions (Figure 4.1; Table 4.2). Regions A and B show the smallest mean distances between individual spiders (55 and 60 m), while region G exhibits the largest (341 m). Intermediate M2CNDs occur in regions C, D, E, and F.

In order to investigate whether the average spacing relates to the spider spatial scale, I mapped the “spider area” to estimate the spider size. The end of each branch of a spider is connected to form a polygon (Figure 4.3), termed a “coverage polygon”. The area of this polygon is taken as the spider area. Histograms for spider sizes on a logarithmic X–axis are shown in Figure 4.4. They indicate that spider sizes correlates with the average spacing (Table 4.2). Some spiders are connected, and it is not always possible to determine whether

they are distinct, thus the measurements in Table 4.2 and Figure 4.4 contain uncertainties which also could be caused by image resolution constraints.

The regional variation of average spacings between the study regions could be related to slope, elevation, and/or latitude. To test this, I extracted each region's average slope, elevation, and latitude (Table 4.2), plotted them against average spacing (M2CND) for each region (Figure 4.5). No obvious relations were observed between them. Note that the seven study regions occur in areas with slopes ranging from 0.37 to 2.01°, which are close to horizontal, thus I did not consider slopes' orientations (Chapter 4.4).

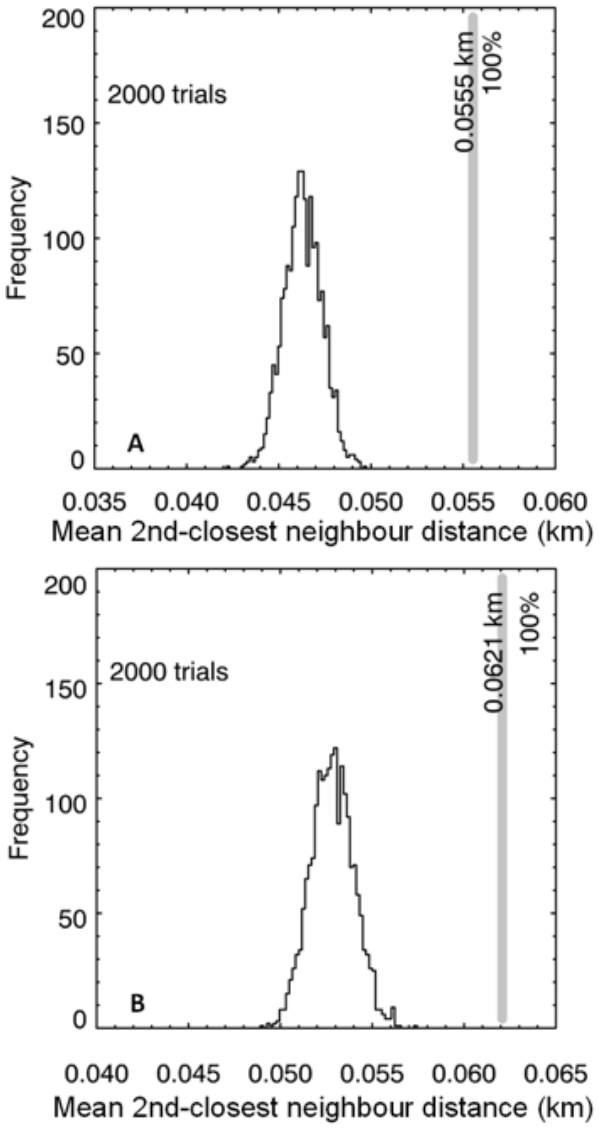

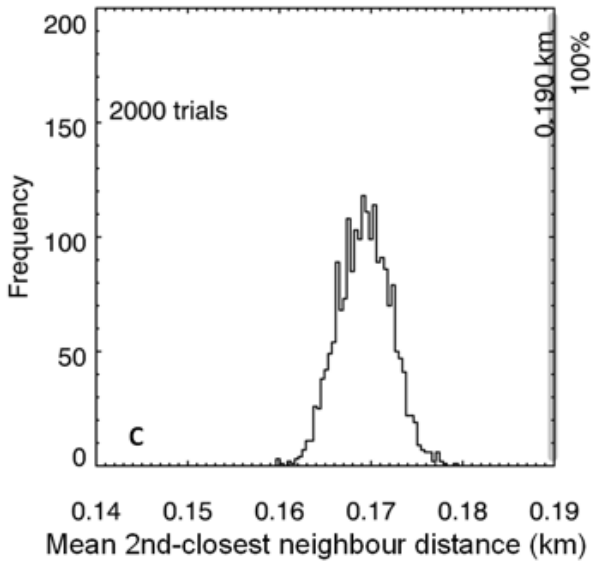
200
150
100
50
0
Frequency
2000 trials
0.190 km
100%
C
0.14
0.15
0.16
0.17
0.18
0.19
Mean 2nd-closest neighbour distance (km)

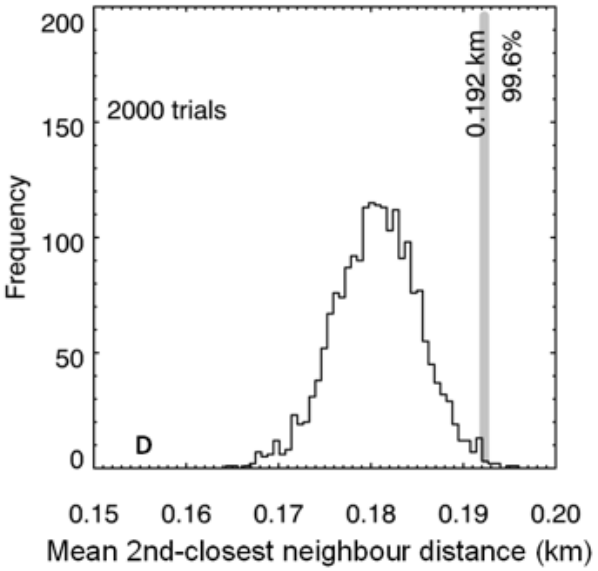
200
150
100
50
0
Frequency
2000 trials
0.192 km
99.6%
D
0.15
0.16
0.17
0.18
0.19
0.20
Mean 2nd-closest neighbour distance (km)

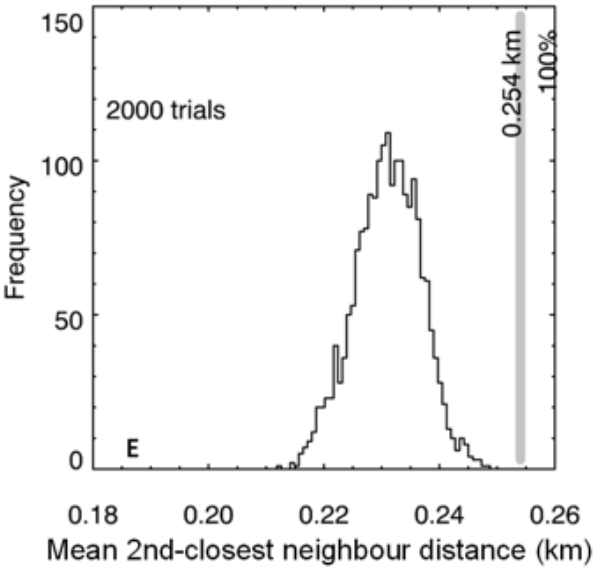
150
100
50
0
Frequency
2000 trials
0.254 km
100%
E
0.18
0.20
0.22
0.24
0.26
Mean 2nd-closest neighbour distance (km)

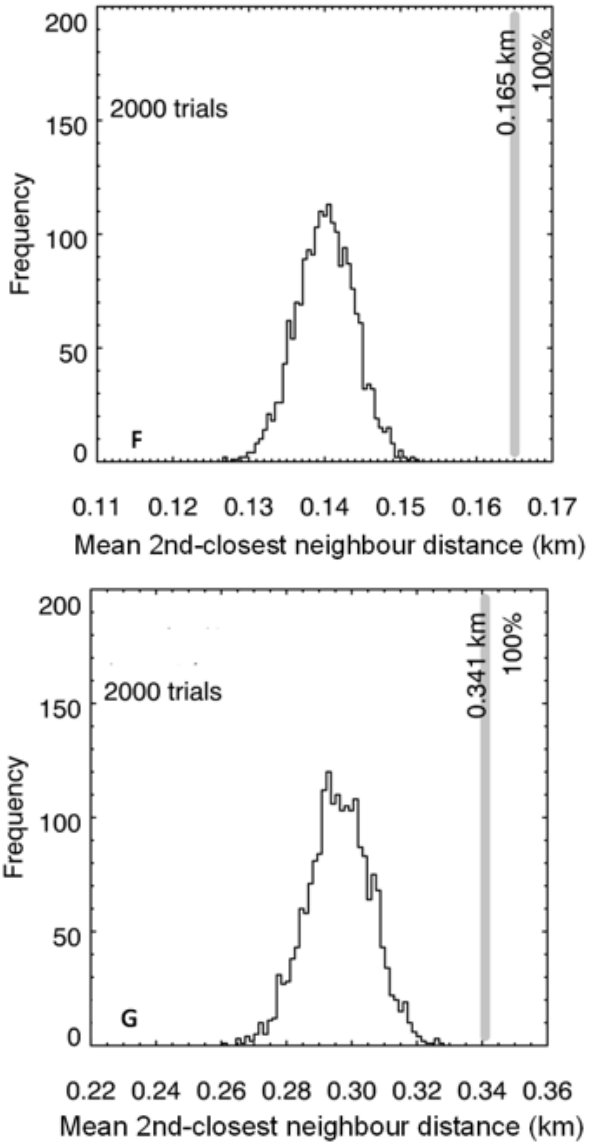

Figure 4.2 The analysis of spatial randomness in seven study regions. The gray bar represents estimated M2CND (the value is marked on the gray bar). The percentages on the gray bars indicate relative positions of observed M2CNDs to the histograms (e.g., in the subfigure A, the observed M2CND lies outside the histogram in the 100th percentile). Each histogram is generated by 2000 random configurations. From regions A to G, the M2CND value lies above the histogram at 9σ, 9σ, 6σ, 3σ, 5σ, 8σ, 4σ respectively.

Rose diagrams are used to visualize the spider trough orientations. Figure 4.6 shows that spider troughs do not have preferred orientations in each region.

I also calculated each region's insolation and checked their possible relations with M2CND (average spacing). At Ls=270, the summer solstice in the southern hemisphere, the incidence angle is lowest, and thus the incoming energy from the sun is the highest. I calculated insolation at Ls=270 and local time ~12:00, the insolation ranges ($W.m^{-2}$) for the 7 study regions are: A 379–400, B 385–394, C 322–338, D 323–344, E 320–354, F 340–354, G 379–395. In Figure 4.7,

the blue “belt” consists of 33450 values from the iterations for one Mars year (Ls from 0° to 360°), each sol includes 50 blue points (Chapter 2.2.3). The insolation at Ls=270 and the daily insolation variations (Figure 4.7) in regions A, B, and G (their latitude range 81.5–82.2°S) are narrow, as well as in regions C, E, D, and F (their latitude range 85.9–87.0°S, Table 4.1 and Figure 4.8). Insolation appears to have no significant correlations with M2CND.

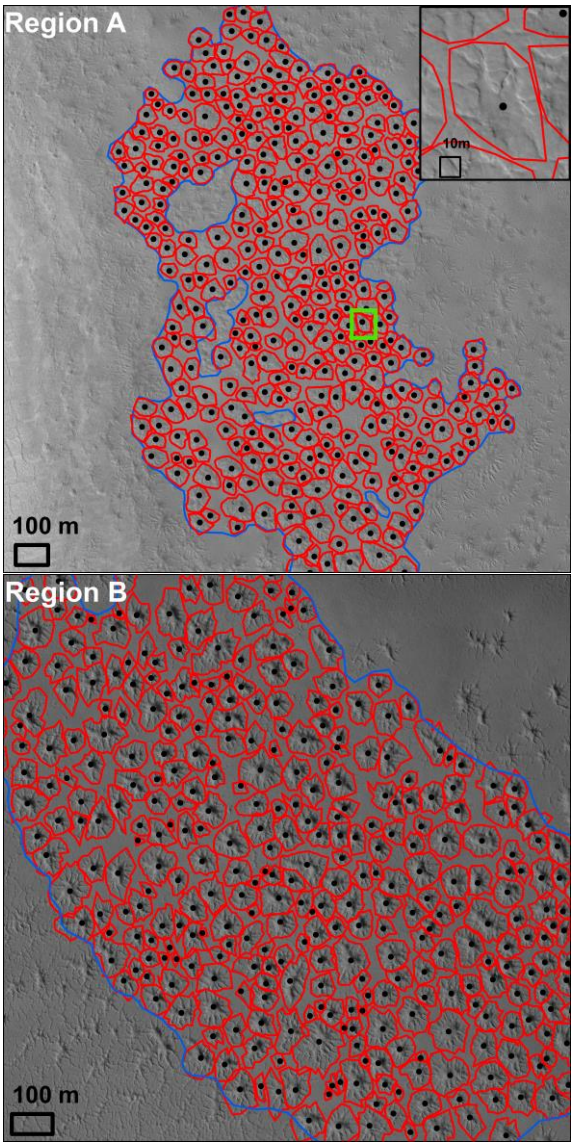

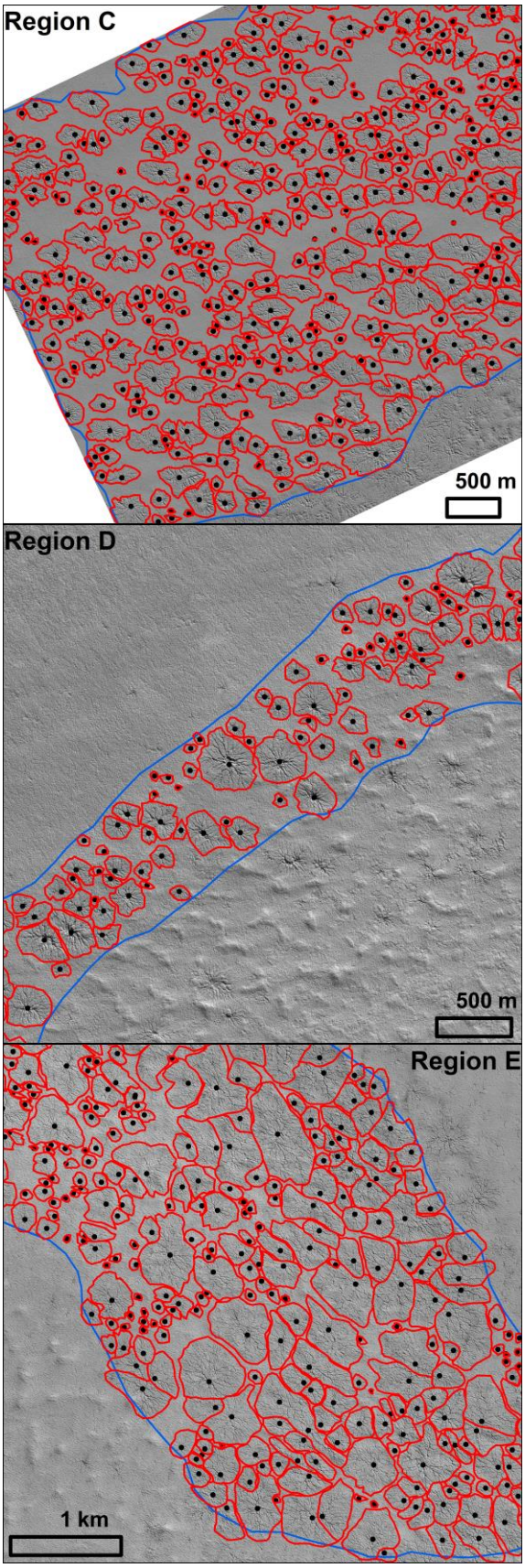
Region C
500 m
Region D
500 m
Region E
1 km

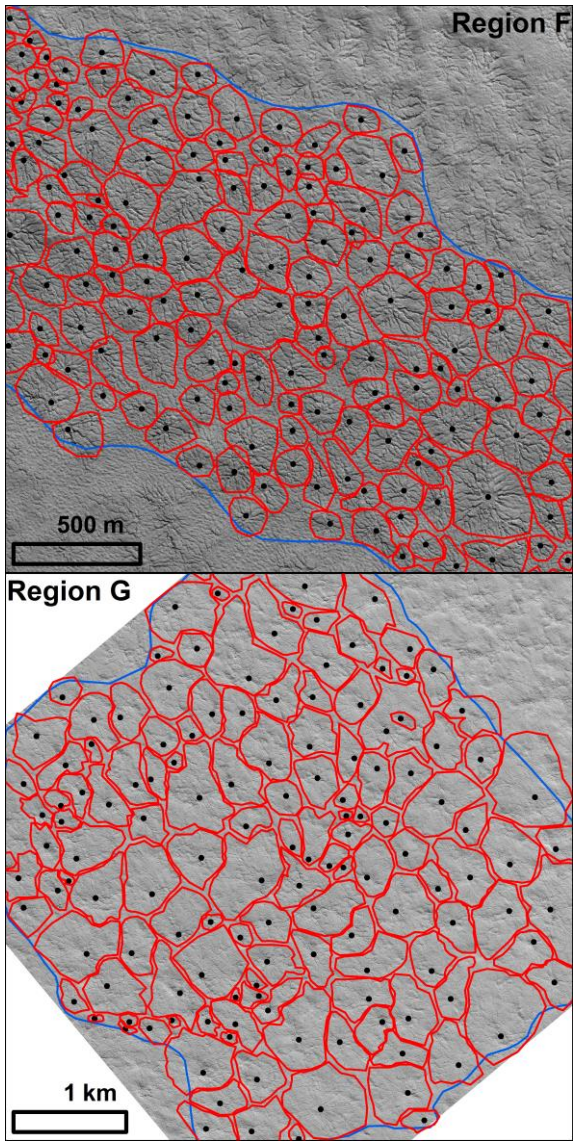

Figure 4.3 Spider areas in regions A–G. The red lines connect each spider's branches to form a polygon. The black points indicate the centers of spiders. The blue lines delineate the extent of each region. In the frame "Region A", the subset frame shows an example of one coverage polygon indicated by the green polygon.

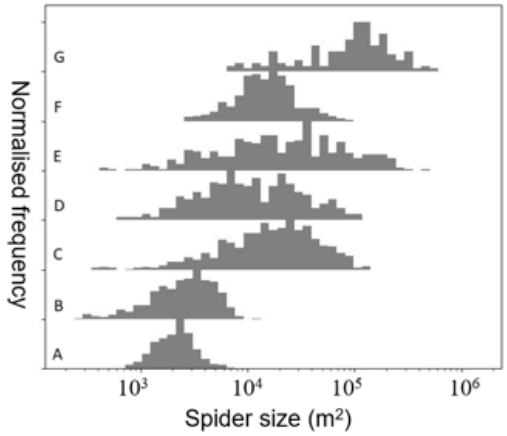

Figure 4.4 Histograms of spider sizes. Regions are marked on the left. The X axis indicates spider sizes, and the Y axis indicates normalized frequencies.

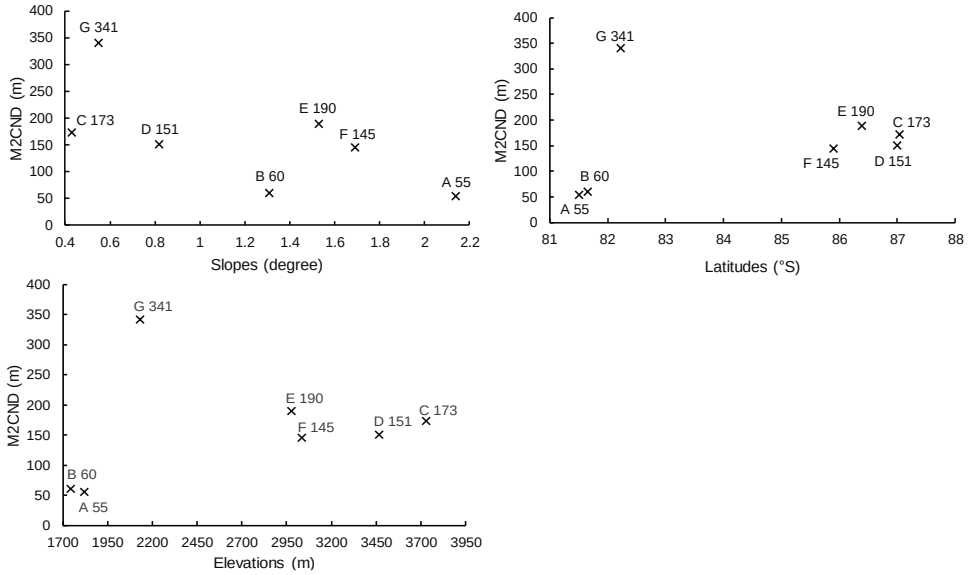

Figure 4.5 Latitude, average elevation, and slope of each region vs. its M2CND. The numbers after "×" symbols are each study region's M2CND.

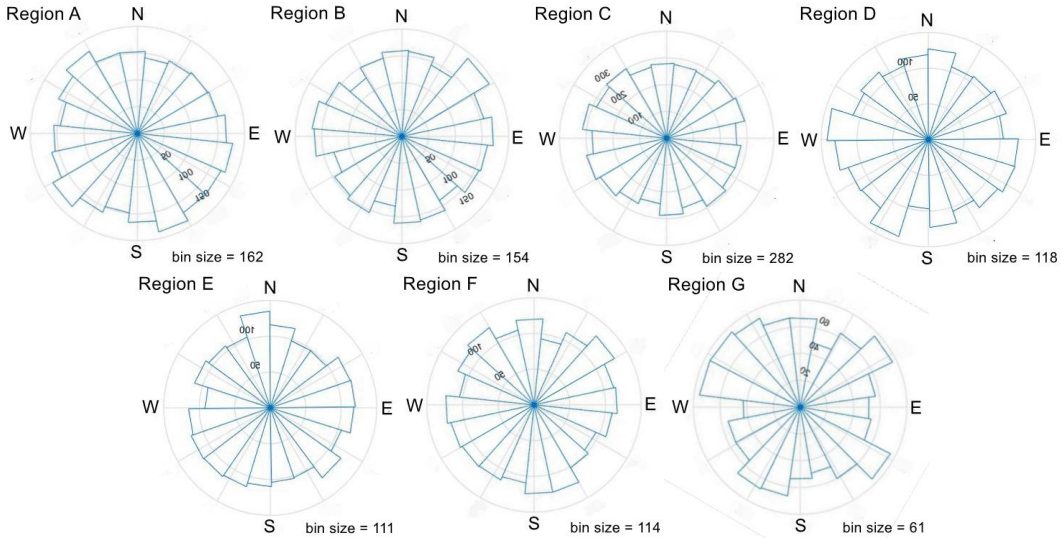

Figure 4.6 Rose diagrams for the spider trough orientations of each region. The radial axis indicates trough numbers of this orientation in each region. The intervals of the radial axis are 20 (region G), 50 (regions A, B, D, E, and F), and 100 (region C). The bin size for each region is 5% of the total trough numbers.

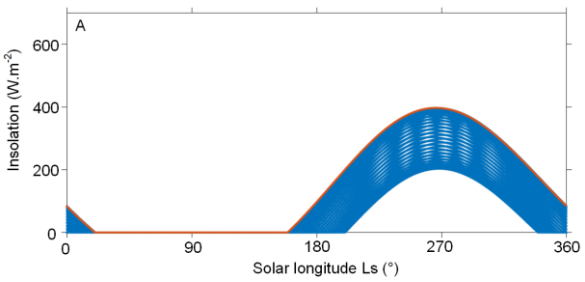

Figure 4.7 Insolation at region A for one Mars year (Ls from 0° to 360°). For other regions, please see Figure S1 in Chapter "Supplementary material". Blue "lines" are discrete points indicating 33450 iteration values. The red line indicates the maximum insolation of each day.

4.4 Discussion

I observed non–random spider spatial distributions in the 7 study regions (Figure 4. 2). This observation of non–randomness is consistent with Hao et al. (2019) that one spider inhibits the formation of a new spider in its vicinity and spider initaiton locations are thus non-random (Chapter III). The spider inter–distances (spacings) or the vicinity sizes are proposed to be linked to substrate properties (Hao et al., 2019). This would mean that average spacing between spiders can change from one region to the other, and this is what I observed and reported in this work: the 7 study regions show regional variation of average spacing; therefore, I believe that substrate properties play a major role in spider formation and spatial distribution.

Thermo–physical numerical modeling (Pilorget and Forget, 2015) confirms that translucent CO_2 slab ice can be formed, sublimating CO_2 gas can be trapped within the substrate, and sufficient pressure can then be accumulated to create gas jetting that mobilizes substrate material (Pilorget and Forget, 2015). Thus, the spider formation process may have been mainly influenced by, (1) properties of the substrate, and (2) properties of the seasonal CO_2 ice layer, e.g., thickness and grain size.

(1) When CO_2 gas moves through the porous substrate (Pilorget and Forget, 2015; Hao et al., 2019), its flow is controlled by permeability, porosity, and cohesion (Muskat, 1937; Bear, 1990; Koponen et al., 1997). Regional differences in these properties will result in differences in pressure gradients and control how CO_2 gas moves through and erodes the porous substrate. The shapes and sizes of particles of the substrate material are closely related to the substrate permeability and porosity (Masch and Denny, 1966; Shepherd, 1989; Ogolo et al., 2015).

(2) The thickness and quality of the seasonal CO_2 ice partly determine the insolation needed to cause basal sublimation and control the ability of the CO_2 slab ice "sealing" layer to retain pressure beneath the CO_2 slab ice layer. The larger the pressure before the jet eruption, the stronger the erosive power of the sub–ice gas flow.

Besides these, other parameters (e.g., insolation and weather) may play roles. In the following, I introduce these parameters and discuss their implications for the spider formation mechanism and spatial configuration.

4.4.1 Properties of the substrate

a. Permeability, porosity, and cohesion

Permeability is the ability of a porous substrate to allow gas (or fluid) to migrate through it (Heijs and Lowe, 1995), controlling the rate of flow (Darcy, 1856; Holst and Aziz, 1972). Permeability is determined by how are pore spaces in the substrate connected to each other. In an extreme case, a material of high

porosity could have pore spaces which are isolated resulting in a low permeability. During spider formation, a lower permeability restricts the gas flow causing a faster rise of local pressure. Sufficient pressure could be accumulated over a shorter distance to initiate gas jetting. Thus, lower permeability possibly leads to reduced spacing of spiders.

Higher permeability allows CO_2 gas to migrate faster with lower resistance, leading to the local pressure being lower as locally produced gas can more easily migrate within the substrate. Gas may migrate over longer distances so that spiders with larger sizes may be formed.

The porosity of a medium is described by its total pore spaces including isolated ones (total porosity) and the fraction of pores that are accessible to gas transport (effective porosity) (Scheidegger, 1958; Heinemann, 2005). In this work, I refer to effective porosity.

The substrate pores serve as gas flow conduits. Higher porosity of the substrate indicates higher capacity for containing sublimating CO_2 gas (Hao et al., 2019). The pressure thus increases more slowly causing a longer build–up to a gas jetting event; if the overlying CO_2 ice is very thin, it may not produce sufficient gas and pressure within the substrate from its basal sublimation to trigger jetting.

Empirical relationships were suggested between porosity and permeability based on simplified conditions, e.g., for particles with uniform shape (Koponen et al., 1997; Beji and Gobin, 1992; Amhalhel and Furmanski, 1997; Miyan and Pant, 2015), permeability generally increases if porosity increases. More spaces between particles lead to a higher permeability in a porous medium.

Porosity can also cause variations in thermal conductivity (Zimbelman, 1986; Piqueux and Christensen, 2009; Presley and Christen, 2010) which is closely associated with thermal inertia (TI) (Kieffer et al., 1977). Lower thermal inertia is possibly associated with lower conductivity which may indicate a higher porosity (Piqueux and Christensen, 2009; Presley and Christen, 2010). However, for the south polar area ($\geqslant$65°latitude), no processed THEMIS (TI) data is currently available for a variety of reasons, such as fine–scale layering, thus no porosity information is deduced from THEMIS observations. For similar reasons, no TES TI data are available for latitudes $\geqslant$ 87°S (Table 4.2). Thus, the porosity of our study regions cannot be inferred from TI.

Cohesion of soil can result from cementation, chemical bonding, or electrostatic attraction (Sullivan et al., 2011). The cohesion of the substrate plays a role in spider formation at the moment when gas jetting occurs. It determines the susceptibility of the material to disintegrate at microscopic scales at the time of gas jetting. Lower cohesion allows fragmentation more easily, leading to the development of a larger central depression rather than the development of

longer troughs. Higher cohesion could reduce the susceptibility to collapse, thus troughs could erode and be sustained over longer distances, leading to spiders with larger sizes.

Hence, I suggest permeability/porosity and cohesion influence not only spider spatial configuration but also morphology. Regional variation of spider average spacings (Figures 4.1 and 4.2) is possibly due to differences of substrate properties (permeability/porosity and cohesion) between the study regions. Regions A and B have smaller average spacings and spiders with smaller sizes (Figure 4.3 and 4.4), suggesting possible lower permeabilities than those of regions C, D, E, F, and G. Another possibility is that regions A and B likely have lower substrate cohesion than those C~G creating smaller spiders (Figure 4.4).

b. Particle size and shape

Normally, larger particles are more difficult to mobilize during gas jetting due to gravity, since the jetting may not be strong enough to lift and transport them (Pilorget et al., 2011). The estimated particle size of the substrate surface layer in the south polar area is 50–200 μm (Paige and Keegan, 1995; Putzig et al., 2005; Fergason et al., 2006). It is not clear whether variation of particle size of the substrate material within this range would affect dust mobilization.

Both particle size and shape are related to the substrate porosity. It is suggested that porosity can increase as particle size decreases (Ogolo et al., 2015), and that, concerning shape, more spherical particles can be more densely packed (i.e., occupy more space), leading to lower porosity (Jackson et al., 1978). Particle size may also affect permeability, as larger particles correspond to higher permeability (Shepherd, 1989).

c. Water ice content

In the south polar area, beneath the seasonal CO_2 ice layer, a dry porous surface layer is generally thought to overlie a water ice–containing layer (Leighton and Murray, 1966; Mellon and Jakosky, 1993; Boynton et al., 2002; Feldman et al., 2002b; Mitrofanov et al., 2002; Tokar et al., 2002; Mellon et al., 2004; Schorghofer and Aharonson, 2005; Demidov et al., 2015). Spider troughs may erode within the dry surface layer, and then extend downward approaching the water ice–containing layer (Figure 4.8). In the latter case, one may speculate that the water ice–containing layer would have a low permeability preventing downward migration of the CO_2 gas. However, when solar insolation is present and the overlying seasonal CO_2 ice has sublimated away, water ice that is close to the trough base would also sublimate and diffuse out to the atmosphere. Consequently, a dry surface lag layer would form that is locally deepened and incised (Figure 4.8), again providing a porous reservoir that can be filled with CO_2 gas. In the end, water ice content or concentration should not act significantly to inhibit spider formation nor influence their spatial configuration.

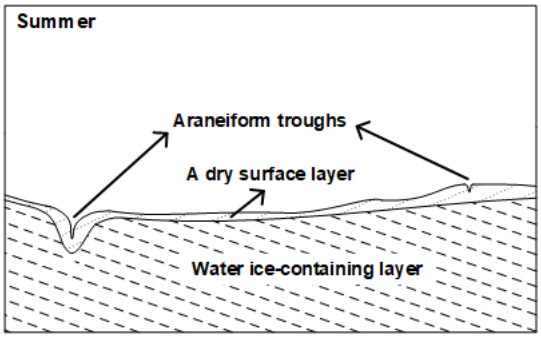

Figure 4.8. Schematic cross–section view of possible positions of spider troughs relative to layers at the Martian south polar region. In spring, the dry surface layer is overlain by the seasonal CO_2 ice (Figure 3.9).

When the water ice sublimates away, it leaves a porous substrate, which could be occupied with sublimated CO_2 gas later. Thus, we can consider the water ice content as being indicative of the potential substrate porosity when dried, with high water ice content suggesting a potential high porosity.

However, the data for WEH (considered to be a measure of water ice content) derived from the MONS instrument poleward of 75°S are usually considered unreliable (Pathare et al., 2018), and the spatial scale of HEND observations is too low to resolve the seven study regions (e.g., HEND estimated the WEH with only one value (=55%) for the whole south polar region; Mitrofanov et al., 2004). Thus, I did not use WEH in my study and estimate porosity.

4.4.2 Properties of the seasonal CO_2 ice

a. Thickness of the seasonal CO_2 ice

The thickness of the seasonal CO_2 ice layer at the south pole was estimated to be up to 2.5 m depending on location (Smith et al., 2001b; Aharonson et al., 2004). Differences in thickness may be due to local surface topography or different mechanisms of condensation, i.e., snowfall or frost. If the CO_2 ice is very thin and thus mechanically weak, the gas cannot be sufficiently pressurized for gas jetting before the layer breaks. On the other hand, a thicker ice layer requires more insolation to penetrate. Therefore, a CO_2 ice layer that is too thick may suppress basal sublimation and resist fracturing.

Thus, if the CO_2 ice is either too thick or too thin, occurrences of basal sublimation and gas jetting can be suppressed thereby reducing the possibility of initiation of spider formation. Thus, only a narrow range of thicknesses of the seasonal CO_2 ice may be optimal for spider formation. This may explain why spider locations are confined to specific locations rather than found everywhere. Within this optimum thickness, a relatively thinner CO_2 slab ice may favor smaller spiders with smaller spacings due to less gas accumulation. Although I do not have observations on local CO_2 ice layer thickness, we suggest the variation of CO_2 ice thickness likely relates to the regional variation of average spacing observed in my work.

b. Grain size of the seasonal CO_2 ice

Variations of CO_2 grain size could contribute to albedo variations of the ice layer (Hansen, 1999; Kieffer et al., 2000; Nolin and Dozier, 2000; Eluszkiewicz et al., 2005; Brown et al., 2008), which in turn will affect the proportion of solar energy reflected or absorbed by the ice. Thermal modeling suggests that solar flux transmitted by the CO_2 ice layer increases as its grain size increases (Pilorget et al., 2011); when the grain size of a CO_2 ice layer with a thickness of 0.6 m is larger than 1 mm, the solar flux is able to reach the substrate below (Pilorget et al., 2011); when the grain size is in the range of about 10 cm or more, solar energy which penetrates the CO_2 ice to the substrate is able to trigger basal sublimation (Moroz, 1964; Kieffer, 1970; Pilorget et al., 2011) possibly leading to the gas jetting to initiate spider formation.

Since only in the presence of a large–grained translucent CO_2 slab ice, does basal sublimation occur (Chapter I; Kieffer et al., 2000; Kieffer, 2000; Langevin et al., 2007; Pilorget et al., 2011), the grain sizes of the seasonal CO_2 ice thus determine whether its condition is favorable for basal sublimation.

4.4.3 Insolation

A locally warmer region could accumulate sufficient solar energy to trigger jetting earlier and faster than in a colder region. Thus, insolation may influence the timing of gas jetting. When the substrate porosity is low and the insolation increase is fast, the rate of gas accumulation may exceed that of migration inside the porous substrate, causing the overlying ice layer to fracture quickly avoiding pressure increase and thus formation of eruption jets. This would weaken the erosive ability of the process, inhibiting the spider formation. In addition to obliquity, insolation at a specific area can be influenced by latitude, elevation, and local topography.

a. Obliquity

Little is known about the obliquity conditions during spider formation, i.e., whether spiders formed synchronously, or whether they have significant age differences, or are remnants produced during a specific obliquity phase. However, it is expected that obliquity has a strong influence on both CO_2 ice thickness and sublimation (Mischna et al., 2003).

The obliquity of Mars is modeled to vary significantly (possible variation range is from 15 to 60 degrees) on timescales of hundreds of thousands to millions of years (Ward, 1973; Laskar et al., 2002 and 2004). At lower obliquity, the sun has higher incidence angles and the polar CO_2 caps react to be larger and thicker (Toon et al., 1980; Laskar et al., 2002 and 2004; Head et al., 2003; Piqueux and Christensen, 2008), this would reduce the amount of insolation reaching the bottom of the CO_2 ice layer and restrain basal sublimation, preventing spider formation (Piqueux and Christensen, 2008). Conversely, higher obliquity could be favorable for spider formation (Piqueux and

Christensen, 2008), or result in CO_2 ice that is too thin to enable spider formation. Thus, obliquity affects insolation on a global scale, determines whether conditions for spider formation are met or not, and variations of obliquity also shift the geographical locations favorable for spider formation. Besides obliquity, the mean insolation of any region is determined by factors like latitude, elevation, and local topography (slope and orientation).

b. Latitude, elevation, and local topography

Both latitude and elevation influence insolation. Latitude affects the timing and seasonal amount of insolation, and thus the rate of insolation increase and the time of initiation of the gas jetting process (Pilorget et al., 2011). Given the thin atmosphere of Mars, variation in absorbing and scattering insolation caused by elevation differences may not be significant.

Slope and orientation of topography influence received insolation. However, my 7 study regions are mostly horizontal based on MOLA data (Table 4.2; Figure 4.5). This is consistent with observations on spider distribution characteristics (Hansen et al., 2010; Hao et al., 2019) that spiders are limited to horizontal areas. Possible reasons for this may be high probabilities of collapses during spider formation (Hansen et al., 2010) or slopes with a more consolidated soil that is too strong to be eroded (Hao et al., 2019). These are supported by observations of half spiders that have only one half carved in the flat ground and formed merely at the interface of slopes and the level ground (Hao et al., 2019). So far, observations suggest slopes are unfavorable for spider formation.

The insolation variation caused by 2° slope differences is on the order of 10 $W.m^{-2}$ when incidence angles higher than 80°. My observations and measurements on spider morphologies and spatial configurations do not appear to be related to this order of slope variation (Figure 4.2 and 4.5).

If scarps were nearby, the shadowed area's exposure time to insolation would be shorter and gas accumulation could be interrupted or discontinuous. Thus, gas jetting would be less efficient with decreasing frequency, possibly creating spiders with smaller sizes and larger spacings; in the margins of the area affected by shadowing effect, spiders with one directional symmetry may be created (Portyankina and Aye, 2018; Figure 5.4). However, I do not observe scarps in the vicinity of all the study regions, causing no shadowing effect.

Latitude, elevation, and local topography, influence insolation for a given area under a certain obliquity condition. I observe no significant relations between latitude, elevation, and local topography and M2CND (spider average spacing) (Figure 4.5). My observations also show that insolation appears to have no relation with M2CND (Figure 4.7). For the daily insolation variation (maximum and minimum values) and the insolation at Ls=270 and local time ~12:00, regions A, B, and G have similar values, as well as for regions C, E, D, and F

(Figure 4.8). This may result from the fact that regions A, B, and G are located at close latitudes, as well as regions C, E, D, and F (Figure 4.1 and Table 4.1). A possible reason why do latitude, elevation, local topography, and insolation appear to have no relation with M2CND from my observations is that my seven study regions occur within a small latitude range from 82 to 87°S (Figure 1; Table 4.1) and on level areas (Figure 4.6; Table 4.2), such that the differences of these parameters between the study regions are not sufficient to significantly differentiate the formation conditions of spiders. Alternatively, their individual influences may be offset by other factors (e.g., substrate properties).

4.4.4 Weather

The dust ejected by the gas jetting is blown leeward, away from the jet, before it settles on the surface. In a more extreme case while a dust storm occurs, dust covers the total surface. This is likely to cause more surface sublimation of the seasonal CO_2 ice layer as the dust absorbs heat (Pilorget et al., 2011; Pommerol et al., 2011), thus only a smaller fraction of solar radiation may reach the substrate surface (Pommerol et al., 2011) to trigger basal sublimation. Basal sublimation may even be impossible in the case of a dust storm as the dust layer absorbs most of the insolation causing the ice layer to sublimate from above (Pilorget et al., 2011).

If regional wind occurs more frequently in one region than others, some surfaces could experience longer periods during which they are covered by dust. This could cause more surface sublimation than basal sublimation (Pilorget et al., 2011), and consequently slow down or block basal sublimation and gas jetting. The dust can be possibly removed by later wind events, re–enabling basal sublimation. Wind occurrence and speed both influence dust transport thereby affecting the rates of surface and basal sublimation.

4.4.5 Spider trough orientations

If preferred orientations were observed in the troughs of spiders, it would indicate a directional control, possibly caused by slope or insolation. As observed from my rose diagrams (Figure 4.6), the spider troughs in my study regions show no preferred orientations. This is consistent with the spider formation mechanism proposed in Hao et al. (2019). The CO_2 jet creates the central depression or pit which has random protrusions. Reinforcement of these protrusions by the gas diversions causes trough formation and growth, leading to their random orientations (Hao et al., 2019).

5. Conclusions

I observed non–random spatial distributions of spiders in the seven study regions at the south pole of Mars and found their average spacings exhibit strong regional variation. These observations indicate that the formation of one spider influences the pressure field such that another spider is less likely to

occur within a certain vicinity (Hao et al., 2019). The regional variation in the spatial configurations likely suggests the regional variability of spider formation and gas jetting.

(1) The study shows that substrate properties (i.e., permeability/porosity and cohesion) directly affect spider formation. Permeability/porosity essentially control spider spatial configuration. Porosity has a role through its influence on permeability. The size and shape of particles of the substrate influence the permeability and porosity. Permeability/porosity and cohesion also influence spider morphology (e.g., trough length). In combination, they contribute to the regional variation of average spacings.

Spider formation occurs within the dry lag surface layer formed through the vertical retreat of water ice, and water ice content of the substrate thus has little effect on spider formation or spatial configuration. However, it may be indicative of a potential increase of substrate porosity after vertical retreat of the ice.

(2) A narrow range of seasonal CO_2 ice layer thickness may be optimal for spider formation, explaining the confined spider distribution to specific locations rather than found everywhere on Mars. Within this range, a relatively thinner CO_2 slab ice may favor smaller spiders, with smaller spacings. Thus, the thickness of the seasonal CO_2 ice layer controls spider spatial distributions on a large scale and its variations affect spider sizes and spacings. The thickness and its variations may be responsible for the regional variation of spider average spacings observed in my work.

(3) Spiders are erosional products of CO_2 basal sublimation and consequent gas jetting. However, basal sublimation and CO_2 jets do not necessarily result in spider formation. Parameters which control elements of basal sublimation and gas jetting thus affect spider formation indirectly. They have effects on spider spatial configuration on a large scale or determine whether regional or local settings are favorable for spider formation. I considered the grain size of seasonal CO_2 ice layer, latitude, elevation, local topography, and weather. The grain size (e.g., insolation can penetrate 0.6 m thick CO_2 ice with grain size larger than 1 mm (Pilorget et al., 2011)) of the seasonal CO_2 ice determines whether the condition of basal sublimation is met. Variations of obliquity, latitude, elevation, and local topography affect insolation. Wind affects the efficiency of basal sublimation through the transport of surface dust which absorbs heat: wind may remove a dust cover to facilitate basal sublimation or deposit a dust cover blocking basal sublimation.

Substrate properties (i.e., permeability/porosity and cohesion) regulate and modify the spatial configuration of a spider population on a regional scale, with insolation and obliquity determining whether general conditions are favorable for spider formation. The obliquity exerts an influence through controlling the

distribution of insolation, and the thickness of the seasonal CO_2 ice and its variations shift the geographical locations favorable for spider formation.

(4) I mapped the spiders' trough orientations and created rose diagrams for each region, and found that spiders troughs show no preferred orientations. Their random orientations are consistent with the spider formation model in Chapter III and Hao et al. (2019)

Chapter V. Spider erosion seen by CaSSIS in comparison with HiRISE

After finishing the work presented in Chapters III and IV, the new ESA mission ExoMars starts to acquire images with the CaSSIS instrument (Thomas et al., 2017). Thus, I analyzed some of these new images and wrote this chapter to introduce the high resolution observations for spiders from CaSSIS and describe how these observations help improve the understanding of spider formation and spatial configurations. CaSSIS has broader high resolution image coverage than that of HiRISE, while HiRISE (McEwen et al., 2007) images were still used when investigating spider morphologies for more detail. I collected the CaSSIS images and other data (HiRISE DTM), selected areas of interests, conducted all the measurements, discussed the observations and measurements, then I concluded the work.

5.1 Introduction

Previous spider observations largely rely on HiRISE images; the newly operating CaSSIS instrument provides an essential complement of high resolution images.

I filtered the CaSSIS images by latitudes from 45° to 75°S to date 2019.05.30, and found 34 images which contain spider features. New locations for spiders were reported to update the spider global mapping of Schwamb et al. (2017).

5.2 CaSSIS observations of spiders

5.2.1 Updated spatial locations for spiders

The latest spider global mapping (Schwamb et al., 2017) shows that spiders were within latitudes higher than 75°S (Figure 5.1) based on CTX, MOC, and HiRISE images. I used new CaSSIS images (Thomas et al., 2017) and reported spiders which are located at latitudes from 68° to 75°S (Figure 5.1).

Spiders were previously observed primarily located within “south polar layered deposits” (Kieffer et al., 2000; Piqueux et al., 2003). Schwamb et al. (2017) reported new geological units as spider hosts, “Early Noachian highland unit” and “Hesperian polar unit”. In addition to these units, I observed that one spider population is possibly within “Middle Noachian highland unit” (Figure 5.2). Spider morphologies are not clearly visible due to the CaSSIS image spatial resolution, thus I cannot exclude the possibility that they might be other features, e.g., seasonal dark deposits. However, troughs appear possibly radially converged to central depressions (Figure 5.2), which are spider characteristics and thus classified as spiders.

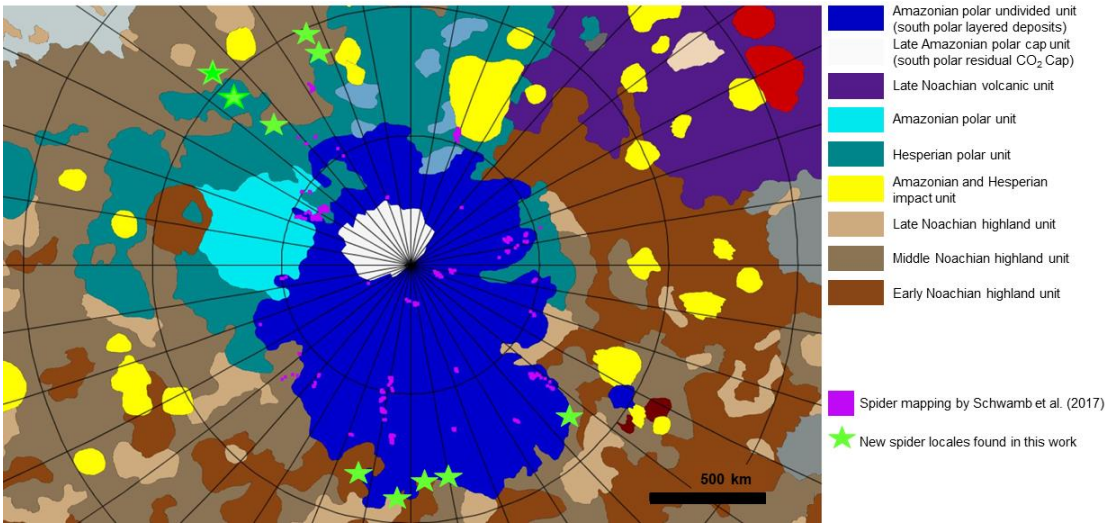

Figure 5.1 Updated spider spatial distributions of Schwamb et al. (2017) overlaid on the geologic map from Tanaka et al. (2014). The pink patches are spider locations mapped by Schwamb et al. (2017) based on CTX, MOC, and HiRISE, and the green pentagrams show new spider locations found in this work by CaSSIS. Latitude and longitude lines are plotted every 10 degrees.

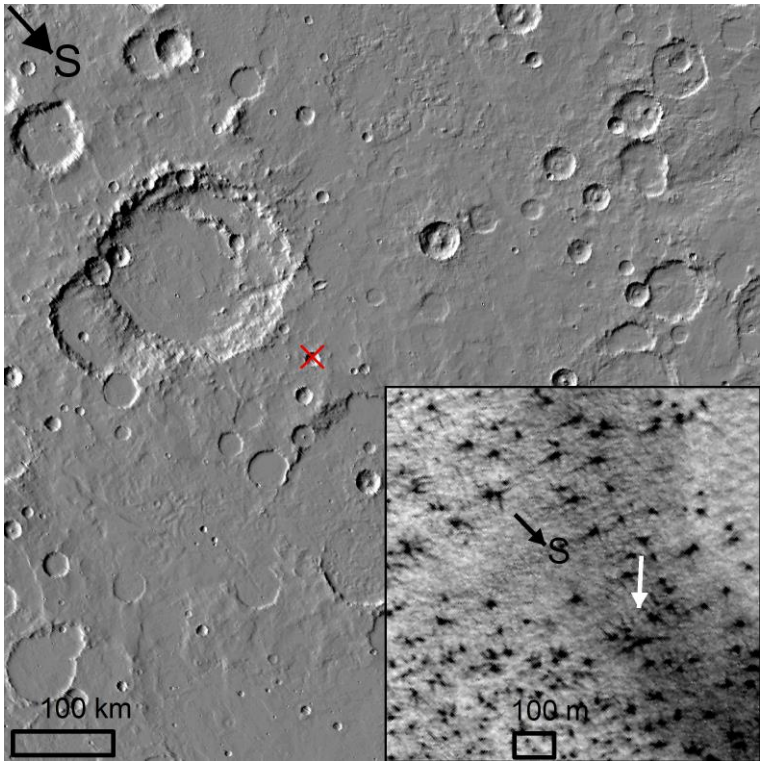

Figure 5.2 A field of possible spiders located in "Middle Noachian highland unit" observed by CaSSIS. The background of the main frame is MOLA hillshade with 463 m/pix. The red symbol "×" indicates the location (centered at ~68.71°S, ~316.02°E) of the spider population". The white arrow in the subframe shows the close–up of the possible spider population. The background of the subframe is CaSSIS image MY34_004137_257_0, imaged at MY=34 and Ls=276.

5.2.2 Spider morphologies at new locations

Half and elongated spiders were newly reported and classified by Hao et al. (2019) (Chapter III) which are located within within Angustus Labyrinthus (centered at ~81°S, ~296°E with the area ~700 km^2), and they have not been reported in other regions so far. Elongated spiders are characterized by linear central depressions, and half spiders are featured by only one–half observable and distributed along ridge boundaries (Hao et al., 2019; Chapter III). I observed the two spider types outside Angustus Labyrinthus, using available HiRISE images in comparison with CaSSIS observations.

a. Half spiders

I first observed that CaSSIS image MY34_003448_267_2 possibly hosts spider–like patterns, parallel troughs likely emanate from dune boundaries (Figure 5.3a). However, the spatial resolution of CaSSIS does not allow me to investigate more detail in morphologies. In order to acquire clear visibility of these features, I looked up HiRISE images and found they were only available for one nearby location (Figure 5.3b).

This HiRISE image covers the area in the vicinity of exposure of south polar layered deposits (the right upper part of Figure 5.3c), ~1 km away from the CaSSIS image (Figure 5.3b). Half spiders were observed at 3 ridge boundaries by this HiRISE image (Figure 5.3c; 5.3d). These ridges have similar orientations of quasi north–south and are ~8 m in height estimated by HiRISE DTM (Figure 5.3). The slope distribution map shows that the slopes of six ridges are up to 45° (the reddish color in Figure 5.3d). The heights of ridges and the slope degree map were measured and generated from 1 m/pix HiRISE DTM. At the east sides of four ridges, radially–organized troughs with no branches or bifurcations were observed at ridge boundaries (Figure 5.3e). Trough lengths range from ~20–50 m (Figures 5.3c and 5.3d). These troughs are radial and show no aprons and alcoves (Malin and Edgett, 2000), thus I classified them as half spiders rather than gullies.

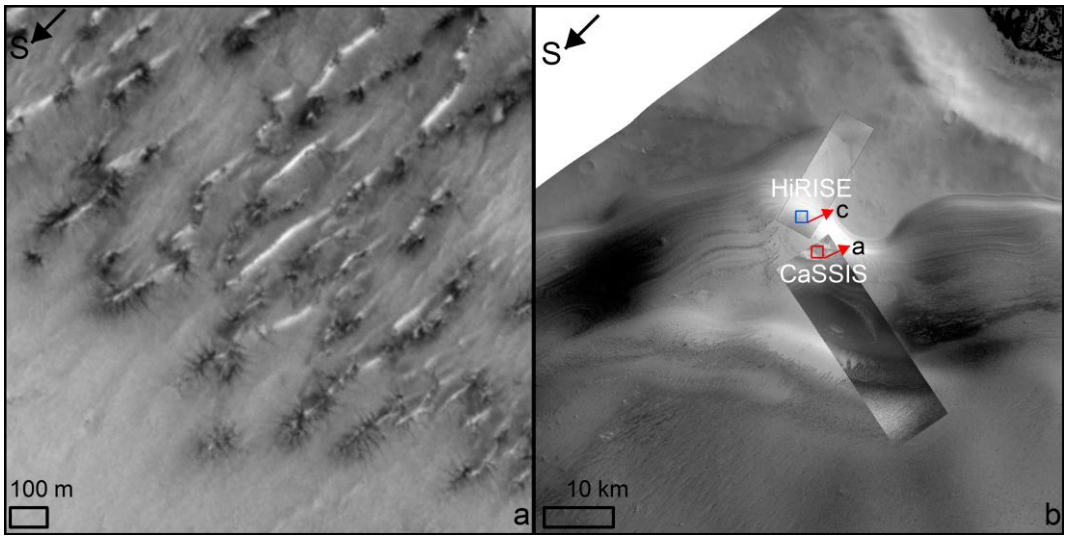

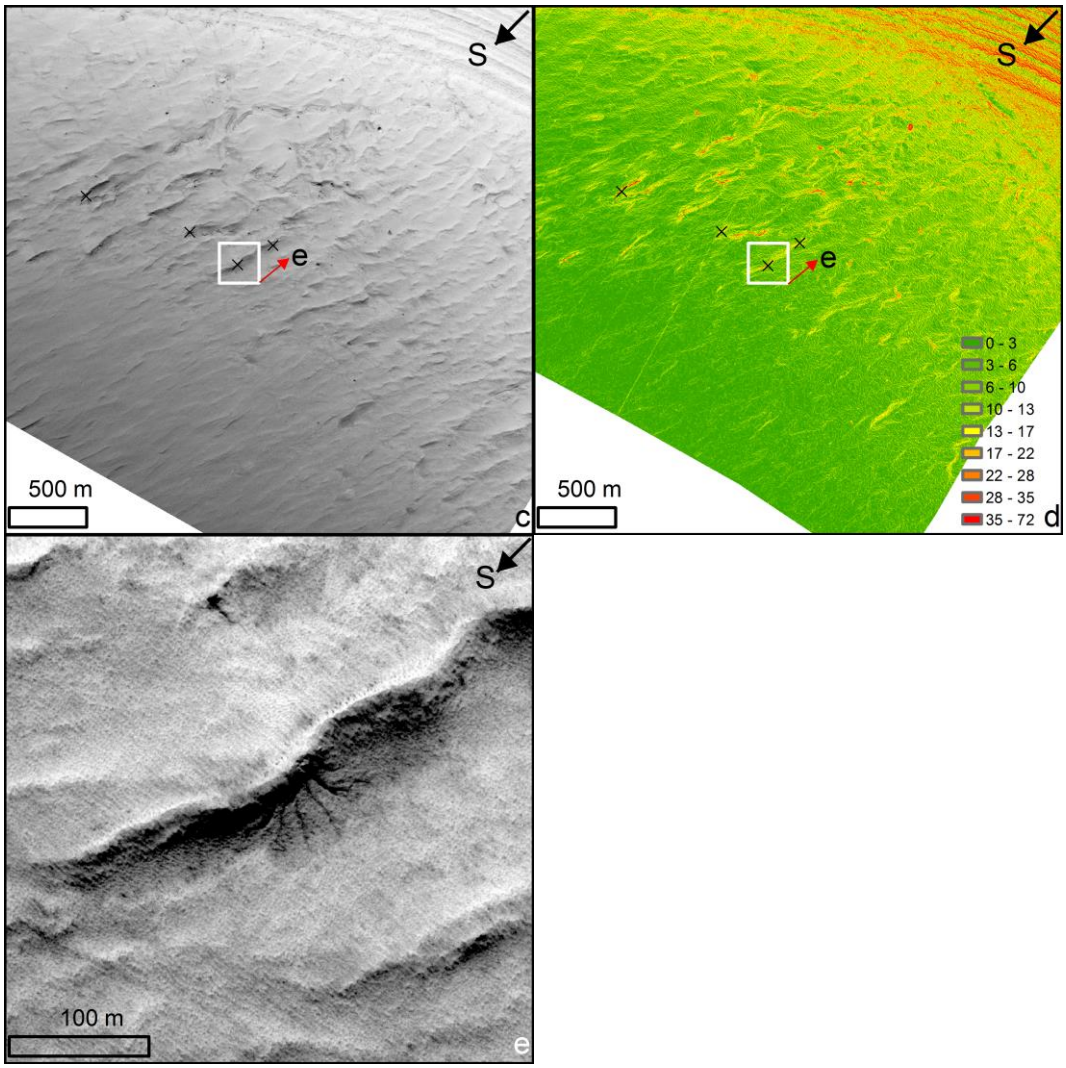

Figure 5.3 Half spiders outside Angustus Labyrinthus. (a) Spider–like patterns on the CaSSIS image MY34_003448_267_2, centered at ~73.21°S, ~133.87°E. (b) The relative locations of spider–like patterns on the CaSSIS image and half spiders on HiRISE image. Background is 25 m/pix HRSC image (Jaumann et al., 2007 and 2015) h8858_0000 showing the polar layered deposits and the exposure of the layering. (c) Four ridges which host half spiders. The image is HiRISE ESP_013277_1070, centered at ~73.18°S, ~133.58°E. (d) Slope degrees of 4 ridges, calculated from 1 m/pix HiRISE DTM DTEPD_013145_1070_013277_1070_A01. (e) Close–up of one half spider at one ridge. Blue and red polygons in (b) show the location of (a) and (c). White polygons in (c) and (d) indicate the location of (e). The black symbols "×" show the locations of half spiders.

b. Elongated spiders

Elongated spiders were observed in 5 regions by CaSSIS and HiRISE images (Figures 5.4, 5.5, and 5.6). Their troughs are radially converged to linear central depressions. Hereafter, I refer other spiders without linear central depressions as non–elongated spiders in order to compare with elongated spiders.

Hao et al. (2019) reported elongated spiders in one horizontal area without scarps or ridges nearby where linear central depressions frequently intersect (Figure 5.4a; Chapter III). As shown in Figure 5.4 and 5.5, elongated spiders in additional 4 regions were located in the vicinity of scarps, having linear central depressions that are quasi–perpendicular to scarps. The slope degrees of these scarps are presented in Table 5.1. Elongated spiders are distributed on the pole–facing sides.

The elongated spiders illustrated in Figure 5.4b were first reported by Portyankina and Aye (2018), described as asymmetric spiders influenced by the scarp. Due to their linear central depressions, I classified them as elongated spiders. These linear central depressions are approximately evenly spaced with an average spacing of 260 m and lengths ranging from 200 to 500 m (Table 5.1). For the other regions shown in Figure 5.4a, c, d, and 5.5, elongated spiders exhibit proximity to non–elongated spiders. In Figures 5.5, closer to the scarps, elongated spiders have fewer branches; with increasing distance from the scarps, spiders have more "legs" and are more well–defined.

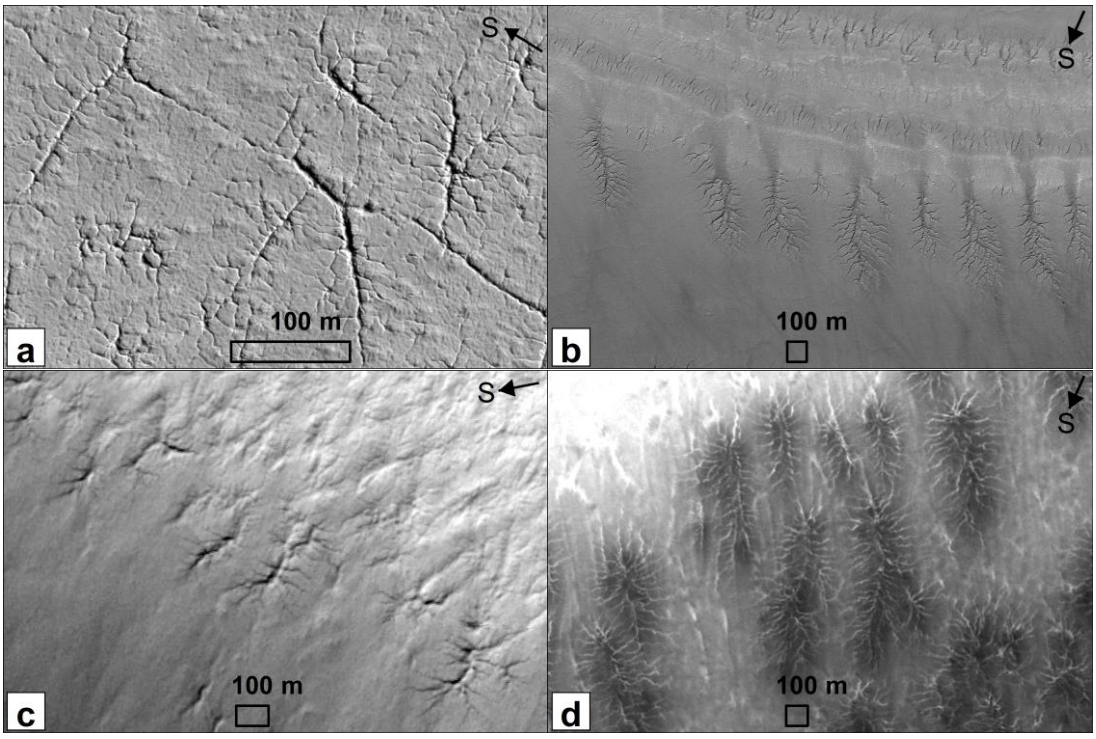

Figure 5.4 Elongated spiders in CaSSIS and HiRISE images. (a) HiRISE image PSP_006204_0985, centered at ~81.76°S, ~296.02°E, reported in Hao et al. (2019) (Chapter III). (b) HiRISE image PSP_005627_1015, centered at ~78.22°S, ~203.22°E. (c) CaSSIS image MY34_004230_266_0, centered approximately at 73.15°S, 169.60°E. (d) CaSSIS image MY34_002116_270_0, centered at ~73.61°S, ~166.94°E.

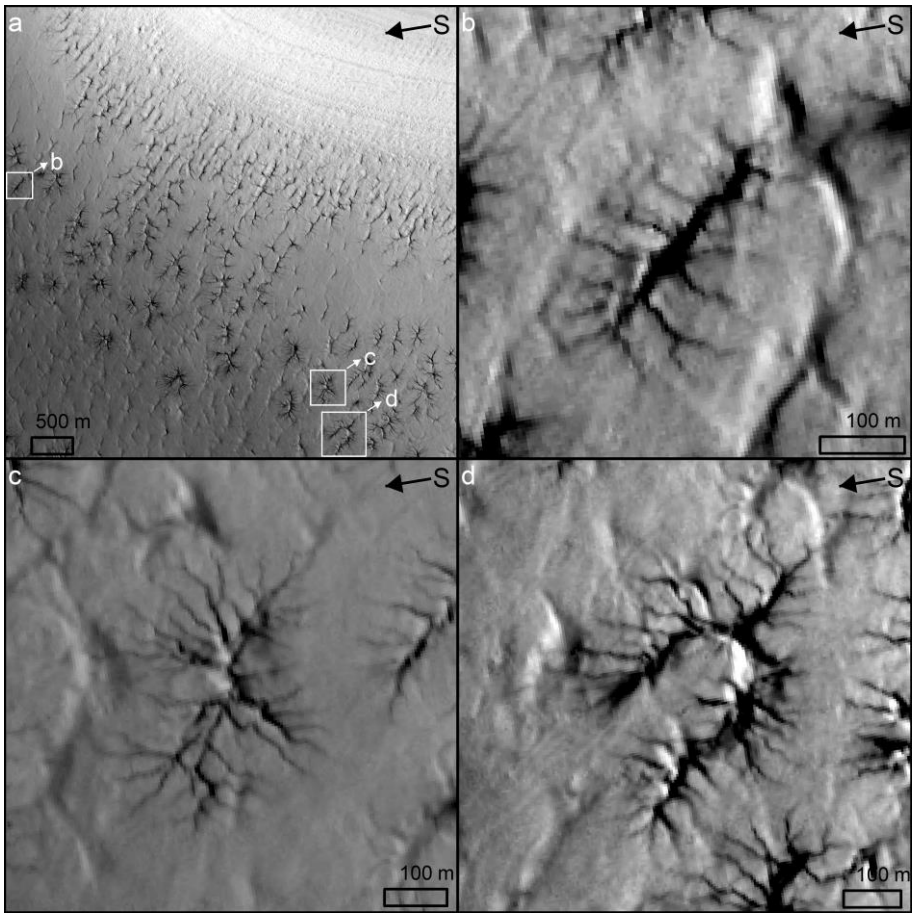

Figure 5.5 A field of elongated spiders. (a) An overview of elongated spiders in the CaSSIS image MY34_004566_269_2, centered at ~73.96°S, ~171.28°E. Squares indicate locations of (b), (c), and (d).

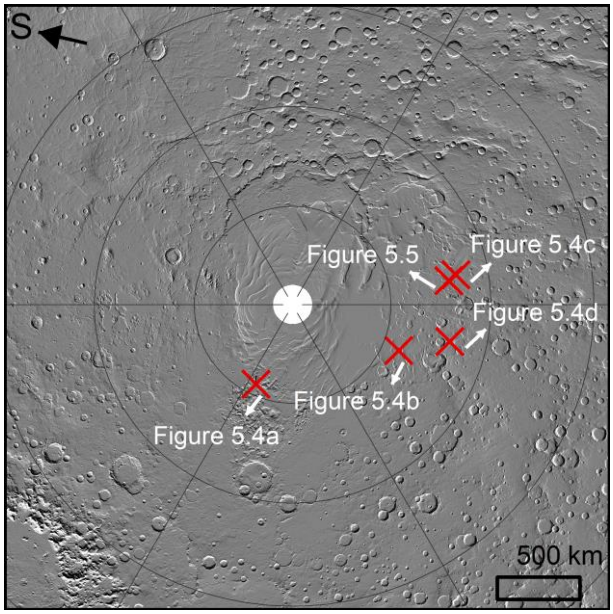

Figure 5.6 The overview of elongated spiders observed in this work. Red "×" symbols indicate approximate locations of elongated spiders in Figures 5.4 and 5.5. Background is MOLA hillshade with 463 m/pix (Smith et al., 2001b). Latitude and longitude lines are plotted every 10 and 60 degrees.

Table 5.1 Measurements for elongated spiders

Locations	Slope (~°)	Orientation	Lengths of linear depressions (~m)	Average spacing (~m)
Figure 5.4b	5–15	Pole–facing	200–500	260
Figure 5.4c	6–8	Pole–facing	120–260	321
Figure 5.4d	6–8	Pole–facing	200–500	398
Figure 5.5	6–9	Pole–facing	200–280	273

5.3 Discussions

5.3.1 Additional geological unit host for spiders

Since spiders occur only in the upper few centimeters or meters of the substrate, while the geological units are classified on a global scale and refer to structures which penetrate much deeper. Thus, spiders are much younger than the host geological units. Thus, I suggest that geological units are likely not necessarily related to spider formation and thereby its spatial distribution (Chapter V; Schwamb et al., 2017).

Spider formation is related to substrate material mobilization. As discussed in Chapter I, Piqueux and Christen (2008) estimated the volume of mobilized soil from the substrate based on thermal modeling (Kieffer et al., 2006) and suggested this mobilization displaces more material than that of each year's global dust devils (Whelley and Greeley, 2008) or one global dust storm (Martin, 1995). Thus, new spider locations reported in this chapter expand the scale of substrate material mobilization. This helps evaluate the budget of global dust and provides insight into the global dust cycle.

5.3.2 Formation of half spiders

As discussed in Chapter III (Hao et al., 2019), I attribute the formation of half spiders to different material properties between horizontal areas and ridges: over winters and autumns, seasonal translucent CO_2 slab ice covers ridges and horizontal areas. In springs, solar insolation penetrates to the substrate and heats CO_2 ice base; the sublimating gas disperses into the substrate, pressure accumulates. More consolidated substrate material on ridge slope with lower permeability and porosity causes faster pressure rising. Thus, gas migrates downwards to ridge boundaries, the topography break of ridges and the horizontal area likely lead the seasonal CO_2 ice at the interface or boundary to rupture more easily. Hence, CO_2 gas jetting occurs along the ridge boundary, initiating spider formation. However, more consolidated and less porous substrate material on ridge slope inhibits the growth of spider troughs up the slopes (Hao et al., 2019; Chapter III) or the collapses of troughs prevent more trough formation on slope (Hansen et al., 2010). Thus, troughs only extend on the horizontal area, leading to the formation of half spiders.

Half spiders in Angustus Labyrinthus are distributed at both sides of ridges and show complex trough structures with more branches and bifurcations (Hao et

al., 2019; Chapter III). At 81°S (Figure 5.3), I only found 4 half spiders at the east sides of ridges with no branches and bifurcations. These differences may be caused by the differing steepness and orientations of ridges and scarps. Ridges which host half spiders in Angustus Labyrinthus have lower slopes ranging from 2° to 6°, only one ridge's orientation is south–north (Table 3.2 and Chapter III). This suggests both sides of these ridges can receive insolation leading to the probability of half spider formation, which is consistent with the observations (Figure 3.2 and Chapter III). As shown in Figure 5.3, half spiders are located at scarps which are steeper than 20°. These scarps result in shadows reducing insolation. However, directions of these scarps have little deviating angles from the south–north direction (Figure 5.3e). This deviating causes the scarps to have equator–facing sides with limited insolation which may initiate the formation of half spiders with poorly–defined trough structures.

5.3.3 Formation of elongated spiders

In Angustus Labyrinthus, in proximity to elongated spiders, linear depressions without troughs were observed (Hao et al., 2019; Chapter III). It is not clear how these linear depressions formed, thermal contraction (Levy et al., 2009; 2010) may be responsible. Elongated spiders were suggested to be formed by exploiting these pre–existing troughs as ready pathways for pressurized gas (Hao et al., 2019; Chapter III).

Regions presented in this chapter host scarps which are mostly perpendicular to the directions of central linear depressions of elongated spiders (Figure 5.4b, c, and d). Portyankina and Aye (2018) suggested the trough patterns of spiders shown in Figure 5.4 were caused by the nearby scarps but without explanations. My formation model (Hao et al., 2019; Chapter III) is able to explain how these elongated spiders form and what is the role of these scarps. As shown in Figure 5.4 and 5.5, elongated spiders are on pole–facing sides of the scarps. Hence, away from the scarps, annual or daily insolation is increasing. Gas accumulating along this direction, i.e., perpendicular to the scarps, is dominant. Thus, protrusions of the same direction in initial central pits are much more strongly reinforced than those of the other directions, linear central depressions are thus created quasi–perpendicular to the scarps. Inhibited zones around linear central depressions should restrain the growths of bifurcations and branches due to their neighboring spiders' "competition" of gas accumulation (Hao et al., 2019; Chapter III). The substrate is possibly not homogenous, thus inhibited zones have different sizes which cause a few bifurcations and branches. In Figure 5.5, I observed that the non–elongated spiders are located farther from the scarp than that of elongated spiders. I suggest that the non–elongated spiders are distributed at the area without shadows or at the margin, thus gas is able to be accumulated possibly equally without dominant directions.

5.4 Summary

In this chapter, I introduce observations from the CaSSIS dataset, which present new locations of spiders. In addition to Angustus Labyrinthus (Chapter III), new host areas for half and elongated spiders are reported. These observations enhance hypothesis of the spider formation model proposed in this thesis (Chapter III) that substrate properties (permeability/porosity) play a key role in spider formation. New spider observations at lower latitudes also provide an insight into the dust mobilization scale from gas jetting.

Chapter VI. Discussion

The south pole of Mars exhibits abundant distinctive and exotic landforms, most of which occur within the region covered by the seasonal CO_2 ice. Araneiform terrain is one of these unusual geomorphic features, resulting from CO_2 sublimation driven erosion. They are so far only known to occur at the south pole and have no earthly analogies. In this thesis, I have investigated spatial configurations for spiders and their troughs, and the spider formation mechanism. This research involves usage of high–resolution images, e.g., HiRISE and CaSSIS.

6.1 Formation of spiders

Both the spider formation model discussed in Chapter III and the Kieffer model (Figure 1.12; Chapter I; Kieffer, 2000 and 2007; Piqueux et al., 2003; Hansen et al., 2010; Portyankina et al., 2017; Hao et al., 2019; Chapter III) attribute spider formation to CO_2 gas jetting caused by basal sublimation of seasonal translucent CO_2 slab ice. The essential difference is, the sublimating gas is trapped within the porous substrate in my model (Figure 3.9) and between the substrate and overlying season CO_2 ice in the Kieffer model, thus I suggest the properties of the substrate, i.e., permeability, porosity, and cohesion, affect spider formation directly. Major issues in spider formation which had not been considered before are well explained by my model, e.g., the detailed formation process of spiders and whether spider spatial distribution is random (Chapter III), and what are responsible for spider sizes and spacings (Chapter IV).

Martian conditions are different from those on Earth (e.g., thin atmosphere and low temperature), therefore testing both models by laboratory experiments or numerical modeling is significantly challenging. Especially, there are few measurements so far for porosity, permeability, and cohesion for the substrate of the south pole. de Villiers et al. (2012) produced spider–like patterns inside granular material by cycled gas–phase jetting, this is consistent with Kieffer and my model that spiders are products of seasonal repetitions of CO_2 gas jetting. However, this experiment (de Villers et al., 2012) did not consider the factor of CO_2 ice and the produced gas jetting occurred through a pre–existing vent in a glass plate. Other laboratory experiments and published numerical modeling mostly focus on the physical properties of CO_2 ice. Dust mobilization could be created from the inside of a pressurized CO_2 slab ice (Kaufmann and Hagermann, 2017). CO_2 condensed from the atmosphere under simulated polar conditions of Mars directly formed translucent slab ice (Portyankina et al., 2018). Pits and furrows were carved into sand–like substrate by sublimating CO_2 ice, but no spiders occur (Mc Keown et al., 2017). The process of cleaning the atmospheric dust embedded in the CO_2 slab ice during condensation was modeled (Portyankina et al., 2010). A thermal model simulated the basal

sublimation of CO_2 ice to investigate the required ice thicknesses and grain sizes of CO_2 ice (Pilorget et al., 2011). Portyankina et al. (2019) applied a two–dimensional Diffusion–Limited Aggregation (DLA) model to produce 2D spider–like shapes. These laboratory experiments or numerical modelings address some aspects (e.g., mobilization of substrate material and the formation of translucent CO_2 slab ice) of spider formation, however, few works are published concerning the whole necessary related factors to create CO_2 gas jetting and spiders. With polar landers or rovers at the south pole, I expect in the future my spider formation model could be partly tested from in–situ drilling data, e.g., permeability, porosity, and cohesion.

Spiders are formed via yearly repetitions of CO_2 gas jetting (Kieffer, 2000; 2007; Hao et al., 2019; Chapter III). Their formation time is therefore at the order of years. Two papers estimated the lower time limits (Piqueux and Christensen, 2008; Portyankina et al., 2017) which are discussed in the following.

Spider formation involves entrainment of substrate material into the atmosphere, which at least partly deposits onto the surface as dark spots and fans under winds (Kieffer, 2007). Piqueux and Christensen (2008) estimated spider formation time based on comparing volumes of these dark deposits to those of spider central depressions. They assumed the darks deposits to be circular: one spot is 50 m in diameter, and the thickness is 1 mm which was estimated from thermal inertial modeling (Kieffer et al., 2006; Kieffer, 2007). Thus the volume of dark spot is ~2 m^3 which points to ~2 m^3 mobilized material from the substrate. Piqueux et al. 2003 adopted 50 m and 5 m as the diameter and depth for one average spider´s central depression. The volume of the spider is therefore ~10^4 m^3. Under the assumption that all ejected material by spider formation forms dark spots, the formation time of one spider was evaluated as at least 0.5 × 10^4 Mars years, i.e., ~ 10^4 years (Piqueux and Christensen, 2008). This estimation assumed that all ejected material deposits as dark spots, however, a small part is probably released into the atmosphere (Piqueux and Christensen, 2008; Portyankina et al., 2017). Piqueux and Christensen (2008) did not consider volumes of spider troughs, but my observations reveal that a large number of spiders (region G; Chapter IV) have deeply eroded troughs and relatively small central depressions (≤ 10 m in diameter) compared with their spatial scales (≥ 400 m), the volumes of troughs are thus not negligible.

Portyankina et al. (2017) directly measured the volume of their observed troughs over 2 Mars years and estimated the minimum average spider erosion is 8 m^3 per Mars year. Thus, the formation time of the spider (~10^4 m^3) adopted by Piqueux and Christensen (2008) would be 1.3 × 10^3 Mars years. It is debatable whether the troughs observed by Portyankina et al. (2017) are or will

be spiders or not, they could be possibly erased or refilled by wind transported dust thus may be similar to seasonal furrows (Bourke, 2013).

Two estimations assumed a constant formation rate for spider formation (Piqueux and Christensen, 2008; Portyankina et al., 2017). According to my model, spiders have different formation rates under different parameters, e.g., a lower permeability causes gas jetting to be more frequent, thus results in a shorter formation time (Chapter IV). HiRISE has observed spiders for nearly 7 Mars years (From MY 28 to 35), however, I did not observe spider growth in my study. The best image or sampling scale of HiRISE is 0.25 m/pix leading to objects larger than 0.75 m being resolved based on sampling theorem (McEwen et al., 2007; Chapter III), thus spider growth may be lower than 0.75 m within the 7 Mars years, or spiders with active growth larger than 0.75 m have not been observed by HiRISE, or HiRISE lacks annual repeating observations for some area (e.g., observed by one single image), or current spiders just do not develop. Therefore, I do not have direct observations to show spider growth to estimate spider formation times. My model does not allow to give precise formation time for spiders; however, it proposes that spiders are formed by seasonal cycles of substrate material mobilization which suggests the smiliar order of the formation times to the two above mentioned estimations (Piqueux and Christensen, 2008; Portyankina et al., 2017).

It is not clear whether currently existing spiders were formed in the same epoch or obliquity phase. Under low obliquity, insolation level would be lower with thicker seasonal CO_2 at the poles (Toon et al., 1980; Piqueux and Christensen, 2008), thus less insolation can reach the substrate and basal sublimation could be impossible or less efficient (Kieffer, 2007; Piqueux and Christensen, 2008). Current spiders were observed at latitudes from 68–88°S (Table 4.2; Chapter V; Schwamb et al., 2017), and it is possible these spiders have significantly differing formation ages due to variations of obliquity. However, it is difficult for detailed quantifications without further information on the substrate permeability, porosity, and cohesion.

6.2 Spatial configurations of spiders

In my model (Chapters III, IV, and V; Hao et al., 2019), sublimating CO_2 gas accumulated from basal sublimation disperses into the substrate. The local rate of CO_2 gas migration or pressure accumulation within the substrate is influenced directly by substrate permeability: lower permeability causes the local pressure to rise faster. Thus, sufficient pressure for a CO_2 jet could be accumulated over a shorter distance. When the local migration rate of gas towards the jet is lower than that of the accumulation from basal sublimation, anther CO_2 jet can occur. This suggests a link between permeability and spacing of spiders (Hao et al., 2019; Hao et al., 2020): lower/higher permeability likely leads to smaller/larger spacings (Chapter IV). This “rate competition”

produces an inhibited zone around one CO_2 jet which later initiates a spider. Inside such a zone, the migrating gas flow acts to inhibit accumulation of sufficient pressure to cause a new CO_2 ice rupture to initiate a new spider. Outside this zone, rate of flow towards the CO_2 jet can be exceeded by the influx from basal sublimation, a new ice rupture and related spider formation can occur. The existence of an inhibited zone suggests that spider spatial configuration is unlikely to be random. From the energy budget view, spider formation is basically an energy and material exchange. One gas jet releases energy so that adjacent area can fail to collect sufficient energy out of pressure accumulation from basal sublimation to initiate gas jetting. Thus, locations of nearby gas jets are certainly not random and determined by energy accumulation condition, e.g., the amount of available gas. This non–randomness is confirmed by the results of spatial randomness analysis at the seven study regions (Figure 4.2). Therefore, in my spider formation model, inhibited zones (Figure 3.9) are proposed to exist around newly developed spiders which restrain the development of new CO_2 jets. Their sizes should vary with regional substrate porosity, permeability, and cohesion and relate with spacings between spiders. Significant regional variation of the spider spacings at the seven study regions (Figure 4.1 and Table 4.2) can be caused by different local substrate permeabilities (Chapter IV).

When CO_2 gas jetting occurs, it produces a cavity or central depression into the substrate (Figure 3.9) which initiates the formation of a spider. The cavity is irregular with random protrusions in shape. These protrusions divert CO_2 gas movement (Figure 3.10), leading to reinforcement of protrusions. Spider troughs are thus formed. Therefore, the spatial configurations of spider troughs should be random. Spider trough orientation mappings and constructed rose diagrams for the seven study regions confirm this randomness (Figure 4.6).

Prior to this thesis, few works had been published on spatial configuration for spiders and their troughs. The Kieffer model does not address these issues. Piqueux et al. (2003) described spider troughs in “seemingly random pattern” and Hansen et al. (2010) thought “the position of their initiation is not a completely random process”, the authors did not explain the reasons and not investigated more in addition to these descriptions. My model considers CO_2 gas activity within the substrate and predicts the characteristics of spatial configurations for spiders and their troughs. The quantitative means, spatial randomness analysis and the trough orientation mappings and rose diagrams, are used for the first time to quantitatively investigate spatial configurations of spiders and troughs.

6.3 Roles of CO_2, water and dust in spider formation and clues for climate

My study shows that spider formation connects a set of processes occurring in the subsurface, at the surface, and in the atmosphere, with annual repetitions, e.g., CO_2 condensation, basal sublimation of seasonal CO_2 ice, gas migration within the substrate, CO_2 gas jetting and mobilization of substrate material or dust (Chapters III and IV; Kieffer, 2000; 2007; Piqueux et al., 2003). Thus, these processes cycle and exchange dust, water, and CO_2 between the subsurface, surface, and atmosphere.

Fine material of the substrate or dust mobilized by gas jetting largely deposits onto the seasonal CO_2 ice surface forming dark spots and fans (Kieffer, 2007; Chapters I and III), A part of the dust may be released into the atmosphere (Kieffer, 2007). Seasonal CO_2 ice condensation may trap dust of the atmosphere which will mostly burrow downwards onto the substrate surface later (Kieffer, 2007; Chapter III). Global or local storms also transport dust from outside of the poles possibly covering the substrate surface (chapter IV; Cantor et al., 2001), ejected dust possibly provides a dust source for dust storms. Thus, a dust recycling process appears to be occurring between the atmosphere, surface, and subsurfacem (Kieffer, 2007). The role of dust in spider formation is still unclear, e.g., dust cumulated from storms may lead to inefficient or no basal sublimation depending on wind speed and frequency (Chapter IV). On the other hand, Piqueux and Christensen (2008) estimated that dust mobilized by gas jetting at the south pole has a mass 100 times that of a global dust storm (Martin, 1995). Dust plays an essential role in atmospheric circulation due to its being a better absorber of visible light than atmospheric CO_2 (Cantor et al., 2001). This property heats the surrounding atmosphere leading to enhanced local circulation and increased surface winds (Cantor et al., 2001), so that more dust can be lifted in the atmosphere. Thus, gas jetting and spider formation are critical in the redistribution of substrate dust, modifying the landscape by extended deposits (Piqueux and Christensen, 2008) of the south pole, and contributing to atmospheric circulation and climate (Cantor et al., 2001).

Water ice in the substrate diffuses or sublimes leaving porosity when exposed at the surface. This may facilitate spider troughs and central depressions developing downwards and into the formerly water ice containing layer (Figure 4.8). This hypothesis is consistent with Piqueux et al. (2008) that atmospheric water vapor in the southern hemisphere may mostly result from water diffusion in soils (Jakosky and Farmer, 1982; Jakosky, 1982). Thus, part of the surface and subsurface of the substrate at the south pole may undergo physical structure changes (e.g., permeability) through spider erosion. Water in the atmosphere is also possibly trapped into the seasonal CO_2 ice through condensation in winter and sublimates back in spring (Kieffer, 2007).

Thus, via the spider formation process, cycles of dust and volatiles (H_2O and CO_2) combine controlling and affecting climate. While Mars' orbital eccentricity and obliquity alter climate partially through their effect on the insolation variation with latitude and time (Forget, 2011), I discussed the detailed consequences on spider formation and spatial configuration (Chapter IV). My work explains most spider observations in detail and expands our current understanding of spider formation and spatial configuration. Relevant parameters are also discussed and classified (Chapter IV), e.g., the reasons for spider size variation and confined locations. Thus, based on spider morphologies and spatial configuration, the substrate and climate conditions under which spiders formed can be deduced.

Chapter VII. Conclusion and outlook

7.1 Conclusion

I surveyed spider formation at the south pole of Mars to understand how interactions of CO_2 in the subsurface, on the surface, and in the atmosphere shapes the polar surface. Spider formation is generally proposed to be triggered by CO_2 jetting driven by basal sublimation of translucent CO_2 slab ice. The pressurized gas was suggested to be trapped between seasonal CO_2 slab ice and the substrate (Kieffer, 2000 and 2007). The essential findings of my work include: (1) I propose a new spider formation model which suggests that sublimating CO_2 gas migrates through the porous substrate towards breaches in the ice cover, rather than being confined between the seasonal CO_2 slab ice and the substrate. (2) This formation model details mechanism of growth of central pits and radiating troughs and explains some characteristics of the growth, e.g., trough length and spider size configuration. (3) I introduce the role of topography in spider formation. (4) I present observations of two new spider types, half and elongated spiders. New spider-like structures' locations which occur further north are observed by CaSSIS. This indicates a broader dust relocation scale by spider formation being an important part of the budget of the global dust. (5) I find spatial distributions of spiders are non–random while the spider trough angular distributions are random, consistent with the abovementioned spider formation model. (6) My work reports a regional variation in spider average spacings, and differences of substrate properties are suggested as primary reasons. (7) I systematically discuss and summarize the effects of relevant parameters on spider spatial configuration as well as spider formation. Substrate properties (permeability, porosity, and cohesion) have a direct influence on both, and others (the seasonal CO_2 ice, insolation, weather, obliquity, latitude, elevation, and slope) affect indirectly or on a large scale. (8) Spiders are confined to specific locations rather than found everywhere. I suggest the possible reason may be due to the strict formation constraints on the thickness of the seasonal translucent CO_2 ice. (9) Some spiders show pronounced central depressions with relatively short troughs. I propose this may be due to low substrate cohesions.

The advances and retreats of the seasonal CO_2 at the south pole lead to CO_2 gas jetting which forms sublimation driven erosional features including araneiform terrain (spider) with various morphologies. CO_2 jetting is the essential agent for shaping and modification the polar surface (Piqueux et al., 2008; Mc Keown et al., 2017) and an essential part of the CO_2 cycle which controls the climate.

My work discusses what environment parameters may be favorable for spider formation and what are their roles in spatial configuration. These parameters

also affect the climate. Thus active/inactive spider formation, or condition of spider formation, or spatial configuration (e.g., slower formation and sparse density) could suggest climate conditions, e.g., which climate parameter may result in inactive spider formation or cause a faster formation, or dense spider configuration. Further, analysis of these parameters on spider formation and spatial configuration could help investigate how the climate evolves from past spider formation epoch to current no spider formation time. The results of my work provide new understanding in the formation process of basal sublimation–driven features and thus offers new insight into the polar surface processes and their effects (influences or implications) in the past and current climatic conditions of Mars.

7.2 Outlook

CO_2 gas jetting and spiders have no terrestrial analogs, thus spider researches are largely dependent on remote sensing missions to provide visible images, topographical, hyperspectral, and thermal data. In the future, I hope that more high–resolution and wider–coverage data would be collected to permit quantitative analyses, e.g., spatio–temporal changes of spiders. Polar landers would be launched so that in-situ data of substrate properties and local topographies would be possible. My study can thus be expanded into broader locales and investigate spider formation and spatial configuration in more detail, e.g., early stages of spider growth or the development of small–spatial scale spiders. I then would be able to address the following scientific questions:

(1) How, and to what extent, do seasonal CO_2 slab ice thickness and grain size, elevation, insolation, water ice content and permeability of the soil, insolation, and weather (wind and dust storms), affect CO_2 jets and spider morphologies and spatial configurations quantitatively?

(2) After addressing (1), answers to the fundamental question will be available: are spiders on Mars still alive? or are spiders still forming today? Products of CO_2 gas jetting, e.g., dark spots and fans deposits, were observed each spring at the south pole (Piqueux et al., 2003; Pommerol et al., 2011), but there have few observations showing growth or new formations of spiders (Portyankina et al., 2017). Either their growth is slower than the current observational limit, or they are presently stagnant. If the former is the case, spiders are an active element in the global atmospheric circulation (CO_2, water, and dust) and indicators of the climate, considering the large amount of dust replacement and CO_2 and water ice transitions (Piqueux et al., 2008). If the latter is the case, why are they not growing or forming now? What environmental parameters favor or suppress their formation? What are the key differences of the current environment and climate from those in the past when they formed?

References

Acton, C. H., 1996. Ancillary data services of nasa's navigation and ancillary information facility. Planetary and Space Science 44 (1), 65–70

Amhalhel, G., Furmański., P., 1997. Problems of modelling flow and heat transfer in porous media. Journal of Power Technologies

Aharonson, O., Zuber, M. T., Smith, D. E., Neumann, G. A., Feldman, W. C., Prettyman, T. H., 2004. Depth, distribution, and density of CO_2 deposition on Mars. Journal of Geophysical Research (Planets) 109, E05004.

Aharonson, O., Schorghofer, N., 2006. Subsurface ice on Mars with rough topography. Journal of Geophysical Research 111, E11007

Appéré. T., Schmitt, B., Langevin, Y., Douté, S., Pommerol, A., Forget, F., Spiga, A., Gondet, B., Bibring, J.–P., 2011. Winter and spring evolution of northern seasonal deposits on mars from OMEGA on mars express. Journal of Geophysical Research 116 (E5), E05001Andrieu, F., Schmidt, F., Douté, S., Chassefière, E., 2018. Ice state evolution during spring in Richardson crater, Mars. Icarus, 315, 158–173

Aye, K.–M., Schwamb, M., Portyankina, G., Hansen, C., McMaster, A., Miller, G., Carstensen, B., Snyder, C., Parrish, M., Lynn, S., Mai, C., Miller, D., Simpson, R., Smith, A., 2019. Planet Four: Probing Seasonal Winds on Mars by Mapping the Southern Polar CO_2 jet deposits. Icarus 319, 558–598

Brooks, R. H., Corey, A. T., 1964. Hydraulic properties of porous media. Colorado state university, Fort Collins, Colorado

Brass, G. W., 1980. The stability of brines on Mars. Icarus 42, 20–28

Bear, J., Bachmat, Y., 1990. Introduction to Modeling of Transport Phenomena in Porous Media, Kluwer, Dordrecht

Beji, H., Gobin, D., 1992. Influence of thermal dispersion on natural convection heat transfer in porous media. Numer. Heat Transfer, Part A (22), 487–500

Byrne, S., Ingersoll, A. P., 2003. A sublimation model for Martian south polar ice features. Science 299, 1051

Byrne, S., Ivanov, A., 2004. Internal structure of the Martian south polar layered deposits. Journal of Geophysical Research 109 (E11)

Barlow, N. G., 2008. Mars: An Introduction to its Interior, Surface and Atmosphere. Cambridge University Press, Cambridge, 264

Bandfield, J. L., 2007. High–resolution subsurface water–ice distributions on Mars. Nature 447, 64–67

Bandfield, J. L., Feldman, W. C., 2008. Martian high latitude permafrost depth and surface cover thermal inertia distributions. Journal of Geophysical Research 113 (E08001)

Boynton, W. V., et al., 2002. Distribution of hydrogen in the near surface of Mars: Evidence for subsurface ice deposits. Science 297, 81–85

Boynton, W. V., and the others, 2003. Constraints on the distribution of hydrogen in the polar regions of Mars and implications for ice formation processes. AGU abstract P32–B05.

Boynton, W. V., et al., 2004. The Mars Odyssey Gamma-Ray Spectrometer Instrument Suite. Space Science Reviews 110, 37–83

Bibring, J–P., Langevin, Y., Poulet F., Gendrin, A., Gondet, B., Berthé, M., Soufflot, A., Drossart, P., Combes, M., Bellucci, G., Moroz, V., Mangold, N., Schmitt B., the OMEGA team, 2004. Perennial water ice identified in the south polar cap of Mars. Nature 428, 627–630

Bellucci, G., Helbert, J., Altieri, F., Reiss, D., Bibring, J.–P., van Gasselt, S., Hoffmann, H., Langevin, Y., Neukum, G., Poulet, F., 2007. Evidence for enhanced hydration on the northern flank of Olympus Mons, Mars. Icarus 192, 361–377

Brown, A. J., Byrne, S., Tornabene, L. L., Roush, T. L., 2008. Louth Crater: Evolution of a Layered Water Ice Mound. Icarus 196, 433–445

Brown, A. J., Calvin, W. M., Murchie, S. L., 2012. Compact reconnaissance imaging spectrometer for mars (CRISM) north polar springtime recession mapping: first 3 mars years of observations. Journal of Geophysical Research 117 (E12), E00J20

Brown, A. J., Calvin, W. M., Mcguire, P. C., Murchie, S. L., 2010. Compact Reconnaissance Imaging Spectrometer for Mars (CRISM) south polar mapping: First Mars year of observations. Journal of Geophysical Research 115, E00D13

Brown, A. J., Piqueux, S., Titus, T. N., 2014. Interannual observations and quantification of summertime H_2O ice deposition on the Martian CO_2 ice south polar cap. Earth and Planetary Science Letters 406, 102–109

Brown, A. J., Calvin, W. M., Becerra, P., Byrne, S., 2016. Martian North Polar Cap Summer Water Cycle. Icarus 277, 401–415

Bourke, M., 2013. The formation of sand furrows by cryo–venting on Martian dunes. 44th Lunar and Planetary Science Conference

Becerra, P., Byrne, S., Brown, A. J., 2015. Transient bright halos on the south polar residual cap of Mars: implications for mass–balance. Icarus 251 (0), 211–225

Bapst, J., Bandfield, J. L., Wood, S. E., 2015. Hemispheric asymmetry in Martian seasonal surface water ice from MGS TES. Icarus 260, 396–408

Bierson, C. J., Phillips, R. J., Smith, I. B., Wood, S. E., Putzig, N. E., Nunes, D., Byrne S., 2016. Stratigraphy and evolution of the buried CO_2 deposit in the Martian south polar cap. Geophysical Research Letters 43, 4172–4179

Bhardwaj, A., Sam, L., Martín-Torres, F. J., Zorzano, M.-P., 2019a. Are slope streaks indicative of global-scale aqueous processes on contemporary Mars? Reviews of Geophysics (57), 48–77

Bhardwaj, A., Sam, L., Martín–Torres, F. J. et al., 2019b. Discovery of recurring slope lineae candidates in Mawrth Vallis, Mars. Scientific Reports 9, 2040

Cutts, J. A., 1973. Nature and origin of layered deposits of the Martian polar region. Journal of Geophysical Research 78, 4231–4249

Cutts, J. A., Lewis B. H., 1982. Models of climate cycles recorded in Martian polar layered deposits. Icarus 50, 216–244

Chase, S. C., Engle, J. L., Eyerly, H. W., Kieffer, H. H., Palluconi, F. D., Schofield, D., 1978. Viking infrared thermal mapper. Applied Optics 17, 1243–1251

Clark, R. N., Fanale, F. P., Zent, A. P., 1983. Frost grain size metamorphism–Implications for remote sensing of planetary surfaces. Icarus 56, 233–245

Carr, M. H., 1986. Mars: A water-rich planet? Icarus 68, 187–216

Carr, M. H., 1996. Water on Mars. New York: Oxford University Press

Colbeck, S., 1997. A review of sintering in seasonal snow (edited by CRREL). U.S. Army Cold Regions Research and Engineering Laboratory, Report 97–10

Clancy, R. T., Sandor, B. J., Wolff, M. J., Christensen, P. R., Smith, M. D., Pearl, J. C., Conrath, B. J., Wilson, R. J., 2000. An intercomparison of ground–based millimeter, MGS TES, and Viking atmospheric temperature measurements: Seasonal and interannual variability of temperatures and dust loading in the global Mars atmosphere. Journal of Geophysical Research 105 (E4), 9553–9572

Clifford, S. M., and the others, 2000. The state and future of Mars polar science and exploration. Icarus 144, 210–242

Cantor, B. A., James, P. B., Caplinger, M., Wolff, M. J., 2001. Martian dust storms: 1999 Mars Orbiter Camera observations. Journal of Geophysical Research 106 (E10), 23653–23687

Christensen, P. R., Bandfield, J. L., Hamilton, V.E., Ruff, S. W., Kieffer, H. H., Titus, T. N., Malin, M. C., Morris, R. V., Lane, M. D., Clark, R. L., Jakosky, B. M., Mellon, M. T., Pearl, J. C., Conrath, B. J., Smith, M. D., Clancy, R. T., Kuzmin, R. O., Roush, T., Mehall, G. L., Gorelick, N., Bender, K., Murray, K., Dason, S., Greene, E., Silverman, S., Greenfield, M., 2001. Mars Global Surveyor Thermal Emission Spectrometer experiment: investigation description and surface science results. Journal of Geophysical Research 106, 23823–23871

Christensen, P. R., et al., 2004. The Thermal Emission Imaging System (THEMIS) for the Mars 2001 Odyssey mission. Space Science Reviews 110, 85–130

Colaprete, A., Barnes, J. R., Haberle, R. M., Robert, M., Hollingsworth, J. L., Kieffer, H. H., Titus, T. N., 2005. Albedo of the south pole on Mars determined by topographic forcing of atmosphere dynamics. Nature 435, 184–188

Carrozzo, F. G., Bellucci, G., Altieri, F., D'Aversa, E., Bibring, J. P., 2009. Mapping of water frost and ice at low latitudes on Mars. Icarus 203 (2), 406–420

Cull, S., Arvidson, R. E., Mellon, M. T., Skemer, P., Shaw, A., Morris, R. V., 2010. Compositions of subsurface ices at the Mars Phoenix landing site, Geophysical Research Letters 37, 24

Chevrier, V. F., Rivera–Valentin, E. G., 2012. Formation of recurring slope lineae by liquid brines on present–day Mars. Geophysical Research Letters 39, L21202

Calvin, W. M., Cantor, B. A., James, P. B., 2017. Interannual and seasonal changes in the south seasonal polar cap of Mars: Observations from MY 28–31 using MARCI. Icarus 292, 144–153

Chinnery, H. E., Hagermann, A., Kaufmann, E., Lewis, S. R., 2018. The penetration of solar radiation into carbon dioxide ice. Journal of Geophysical Research: Planets 123, 864–871

Darcy, H., 1856. Les fontaines publiques de la ville de Dijon

de Villiers, S., Nermoen, A., Jamtveit, B., Mathiesen, J., Meakin, P., Werner, S. C., 2012. Formation of Martian araneiforms by gas–driven erosion of granular material. Geophysical Research Letters 39, L13204

Diniega, S., Hansen, C. J., McElwaine, J. N., Hugenholtz, C. H., Dundas, C. M., McEwen, A. S., Bourk, M. C., 2013. A new dry hypothesis for the formation of Martian linear gullies. Icarus 225, 526–537

Demidov, N. E., Bazilevskii, A. T., Kuzmin, R. O., 2015. Martian Soils: Varieties, Structure, Composition, Physical Properties, Drillability, and Risks for Landers. Solar System Research 49 (4), 209–225

Dundas, C. M., Bramson, A. M., Ojha, L., Wray, J. J., Mellon, M. T., Byrne, S., McEwen, A. S., Putzig, N. E., Viola, D., Sutton, S., Clark, E., Holt, J. W., 2018. Exposed subsurface ice sheets in the Martian mid–latitudes. Science 359, 199–201

Eluszkiewicz, J., 1993. On the Microphysical state of the Martian seasonal caps. Icarus 103 (1), 43–48

Eluszkiewicz, J., Moncet, J.–L., Titus, T. N., Hansen, G. B., 2005. A microphysically based approach to modelling emissivity and albedo of the Martian seasonal caps. Icarus 174, 524–534

Flammarrion, C., 1892. La Planete Mars et ses Conditions d'Habitabilite, v. 1, Gauthier–Villars et Fils, Paris

Farmer, C. B., Davies, D. W, Laporte, D. D., 1976. Mars: northern summer ice cap—water vapor observations from viking 2. Science 194 (4271)

Forget, F., Hourdin, F., Talagrand, O., 1998. CO_2 snowfall on Mars: Simulation with a general circulation model. Icarus 131, 302–316

Forget F., 2011. Obliquity and Obliquity Variations. In: Gargaud M. et al. (eds) Encyclopedia of Astrobiology. Springer, Berlin

Ferris, J. C., Dohm, J. M., Baker, V. R., Maddock, T., 2002. Dark slope streaks on Mars: Are aqueous processes involved? Geophysical Research Letters 29 (10), 1490

Feldman, W. C., et al., 2002a. Fast neutron flux spectrum aboard Mars Odyssey during cruise. Journal of Geophysical Research 107 (A6), 1083

Feldman, W. C., et al., 2002b. Global distribution of neutrons from Mars: Results from Mars Odyssey. Science 297 (5578), 75–78

Feldman, W. C., and 14 colleagues, 2004. Global distribution of near–surface hydrogen on Mars. Journal of Geophysical Research 109 (E09006)

Feldman, W. C., Mellon, M., Gasnault, O., Maurice, S., Prettyman, T., 2008. Volatiles on Mars: Scientific results from the Mars Odyssey Neutron Spectrometer. The Martian Surface: Composition, Mineralogy and Physical Properties. Cambridge: Cambridge University Press, 125–148

Fergason, R. L., Christensen, P. R., Kieffer, H. H., 2006. High–resolution thermal inertia derived from the Thermal Emission Imaging System (THEMIS): Thermal model and applications. Journal of Geophysical Research 111, E12004

Golombek, T. C., Lemoine, M. P., Neumann, F. G., Rowlands, G. A., Aharonson, D. D., Ford, P. G., Ivanov, A. B., Johnson, C. L., McGovern, P. J., Abshire, J. B., Afzal, R. S., Sun, X., 2001. Mars Orbiter Laser Altimeter–experiment summary after the first year of global mapping of Mars. Journal of Geophysical Research 106 (E10), 23689–23722

Giuranna, M., Formisano, V., Grassi, D., Maturilli, A., 2007. Tracking the edge of the south seasonal polar cap of Mars. Planetary and Space Science 55, 1319–1327

Giuranna, M., Grassi, D., Formisano, V., Montabone, L., Forget, F., Zasova, L., 2008. PFS/MEX observations of the condensing CO_2 south polar cap of Mars. Icarus 197 (2), 386–402

Gwinner, K., Jaumann, R., Hauber, E., Hoffmann, H., Heipke, C., Oberst, J., Neukum, G., Ansan, V., Bostelmann, J., Dumke, A., Elgner S., Erkeling, G., Fueten, F., Hiesinger, H., Hoekzema, N. M., Kersten E., Loizeau, D., Matz, K.–D., McGuire, P. C., Mertens, V., Michael, G., Pasewaldt, A., Pinet, P., Preusker, F., Reiss, D., Roatsch, T., Schmidt, R., Scholten, F., Spiegel, M., Stesky R., Tirsch, D., van Gasselt, S., Walter, S., Wählisch, M., Willner, K., 2016. The High Resolution Stereo Camera (HRSC) of Mars Express and its approach to science analysis and mapping for Mars and its satellites. Planetary and Space Science 126, 93–138

Greeley, R., 2013. Introduction to Planetary Geomorphology. Cambridge: Cambridge University Press

Herr, K. C., Pimentel, G. C., 1969. Infrared absorptions near three microns recorded over the polar cap of Mars. Science 166, 496

Hess, S. L., Henry R. M., Tillman J. E., 1979. The seasonal variation of atmospheric pressure on Mars as affected by the south polar cap. Journal of Geophysical Research 84, 2923–2927

Holst, P. H., Aziz, K., 1972. Transient three–dimensional natural convection in confined porous media. International Journal of Heat and Mass Transfer 15 (1), 73–90

Howard, A. D., 1981. Etched plains and braided ridges of the south polar region of Mars: Features produced by basal melting of ground ice? NASA Technical Memorandum 84211, 286–288

Howard, A. D., 2000. The role of aeolian processes in forming surface features of the Martian polar layered deposits. Icarus 144, 267–288

Howard, A. D., Cutts J. A., Blasius K. R., 1982. Stratigraphic relationships within Martian polar cap deposits. Icarus 50, 161–215

Haberle, R. M., Jakosky, B.M., 1990. Sublimation and transport of water from the north residual polar cap on Mars. Journal of Geophysical Research 95, 1423–1437

Haberle, R. M., McKay, C. P., Schaeffer, J., et al., 2001. On the possibility of liquid water on present–day Mars. Journal of Geophysical Research 106, 23317–23326

Heijs, A., Lowe, C. P., 1995. Numerical evaluation of the permeability and the Kozeny constant for two types of porous media. Physical Review E 51 (5)

Houben, H., Haberle, R. M., Young, R. E., Zent, A.P., 1997. Modelling the Martian seasonal water cycle. Journal of Geophysical Research 102 (E4), 9069

Hansen, G. B., 1997. Spectral absorption of solid CO_2 from the ultraviolet to the far infrared. Advances in Space Research 20 (8), 1613–1616

Hansen, G. B., 1999. Control of the radiative behavior of the Martian polar caps by surface CO_2 ice: Evidence from Mars Global Surveyor measurements. Journal of Geophysical Research 104 (E7), 16471–16486

Hansen, G. B., 2005. Ultraviolet to near–infrared absorption spectrum of carbon dioxide ice from 0.174 to 1.8 μm. Journal of Geophysical Research (Planets) 110 (E9)

Herkenhoff, K. E., Plaut, J. J., 2000. Surface ages and resurfacing rates of the polar layered deposits on Mars. Icarus 144, 243–253

Hartmann, W. K., Neukum, G., 2001. Cratering chronology and the evolution of Mars. In Chronology and Evolution of Mars, ed. R. Kallenbach et al. Dordrecht: Kluwer

Head, J. W., Pratt, S., 2001. Extensive Hesperian–aged south polar ice sheet on Mars: Evidence for massive melting and retreat, and lateral flow and ponding of melt–water. Journal of Geophysical Research 106

Head, J. W., Mustard, J. F., Kreslavsky, M. A., Milliken, R. E., Marchant, D. R., 2003. Recent ice ages on Mars. Nature 426, 797–802

Head, J. W., Kreslavsky, M. A., Marchant, D. R., 2011. Pitted rock surfaces on Mars: A mechanism of formation by transient melting of snow and ice. Journal of Geophysical Research 116 (E9)

Hecht, M. H., 2002. Metastability of liquid water on Mars. Icarus 156, 373–386

Hvidberg, C. S., Zwally, H., 2003. Sublimation of water from the North polar cap on Mars. Workshop Mars Atmosphere Modelling and Observations Abstract

Hvidberg, C. S., Fishbaugh K. E., Winstrup M., Svensson A., Byrne S., Herkenhoff K. E., 2012. Reading the climate record of the Martian polar layered deposits. Icarus 221(1), 405–419

Heinemann, Z. E., 2005. Fluid flow in porous media. Montanuniversität Leoben

Hansen, C., Thomas, N., Portyankina, G., McEwen, A., Becker, T., Byrne, S., Herkenhoff, K., Kieffer, H., Mellon, M., 2010. HiRISE observations of gas sublimation–driven activity in Mars' southern polar regions: I. Erosion of the surface. Icarus 205 (1), 283–295

Hansen, C. J., Bourke, M., Bridges, N. T., Byrne, S., Colon, C., Diniega, S., Dundas, C., Herkenhoff, K., McEwen, A., Mellon, M., Portyankina, G., Thomas, N., 2011. Seasonal Erosion and Restoration of Mars' Northern Polar Dunes. Science 331, 575–577

Hansen, C.J., Byrne, S., Portyankina, G., Bourke, M., Dundas, C., McEwen, A., Mellon, M., Pommerol, A., Thomas, N., 2013. Observations of the northern seasonal polar cap on Mars: I. Spring sublimation activity and processes. Icarus 225, 881–897

Hayne, P. O., Paige, D. A., Heavens, N. G., 2014. The role of snowfall in forming the seasonal ice caps of Mars: Models and constraints from the Mars Climate Sounder. Icarus 231, 122–130

Hargitai, H., Kereszturi, A., 2015. Encyclopaedia of Planetary Landforms. Springer, New York Heidelberg Dordrecht London, 87

Hao, J., Michael, G., Adeli, S., Jaumann, R., 2019. Araneiform terrain formation in Angustus Labyrinthus, Mars. Icarus 317, 479–490

Hao, J., Michael, G., Adeli, S., Jaumann, R., Portyankina, G., Hauber, E., Millot, C., Zuschneid, W., 2020. Variability of spider spatial configuration at the Martian south pole. Accepted at Planetary and Space Science

Ivanov, A. B., Muhleman, D. O., 2001. Cloud reflection observations: Results from the Mars orbiter laser altimeter. Icarus 154, 190–206Jackson, P. D., Smith, D. T., Stanford, P. N., 1978. Resistivity porosity particle shape relationships for marine sands. Geophysics 43 (6), 1250–1268

Jakosky, B. M., Farmer, C. B., 1982. The seasonal and global behavior of water vapor in the Mars atmosphere: Complete global results of the Viking Atmospheric Water Detector experiment. Journal of Geophysical Research 87, 2999–3019

Jakosky, B. M., Carr, M. H., 1985. Possible precipitation of ice at low latitudes of Mars during periods of high obliquity. Nature 315, 559–561

Jakosky, B. M., Haberle, R. M., 1992. The seasonal behavior of water on Mars, in Mars, edited by H. H. Kieffer et al., University of Arizona Press, Tucson, 969–1016

Jakosky, B. M., Henderson, B. G., Mellon, M. T., 1995. Chaotic obliquity and the nature of the Martian climate. Journal of Geophysical Research 100, 1579–1584

James, P. B., Kieffer, H. H., Paige, D. A., 1992. The seasonal cycle of carbon dioxide on Mars, in Mars, edited by H. H. Kieffer et al., 934–968, Univ. of Ariz. Press, Tucson

Jaumann, R., Neukum, G., Behnke, T., Duxbury, T. C., Eichentopf, K., Flohrer, J., Gasselt, v. S., Giese, B., Gwinner, K., Hauber, E., Hoffmann, H., Hoffmeister, A., Kohler, U., Matz, K.–D., McCord, T. B., Mertens, V., Oberst, J., Pischel, R., Reiss, D., Ress, E., Roatsch, T., Saiger, P., Scholten, F., Schwarz, G., Stephan, K., Wahlisch, M., the HRSC Co–Investigator Team, 2007. The high resolution stereo camera (HRSC) experiment on Mars Express: instrument aspects and experiment conduct from interplanetary cruise through the nominal mission. Planetary and Space Science 55, 7–8

Jaumann, R., Tirsch, D., Hauber, E., Ansan, V., Di Achille, G., Erkeling, G., Fueten, F., Head, J., Kleinhans, M., Mangold, N., Michael, G., Neukum, G., Pacifici, A., Platz, T., Pondrelli, M., & Raack, J., Reiss, D., Williams, D., Adeli, S., Warner, N., 2015. Quantifying geological processes on Mars–Results of the High Resolution Stereo Camera (HRSC) on Mars Express. Planetary and Space Science 112

Jian, J.–J., Ip, W.–H., Sheu, S.–R., 2009. Spatial distributions and seasonal variations of features related to a venting process at high southern latitudes observed by the MOC camera. Planetary and Space Science 57, 797–803

Kieffer, H. H., 1970. Interpretation of the martian polar cap spectra. Journal of Geophysical Research 75, 510–514

Kieffer, H. H., Chase Jr., S. C., Miner, E., Münch, G., Neugebauer, G., 1973. Preliminary report on infrared radiometric measurements from the Mariner 9 spacecraft. Journal of Geophysical Research 78 (20), 4291–4312

Kieffer, H. H., Chase, S. C., Martin, T. Z., Miner, E. D., Palluconi, F. D., 1976. Martian North Pole Summer Temperatures–Dirty Water Ice. Science 194 (4271), 1341–1344

Kieffer, H. H., Martin, T. Z., Peterfreund, A. R., Jakosky, B. M., Miner, E. D. and Palluconi, F. D., 1977. Thermal and albedo mapping of Mars during the Viking primary mission. Journal of Geophysical Research 82, 4249–4291

Kieffer, K. K., 1979. Mars south polar spring and summer temperatures: A residual CO_2 frost. Journal of Geophysical Research. Res., 84, 8263–8288

Kieffer, H. H., 1990. H_2O grain size and the amount of dust in Mars' residual north polar cap. Journal of Geophysical Research 95, 1481–1493

Kieffer, H. H., 2000. Annual punctuated CO_2 slab–ice and jets on Mars. 2nd International Conference on Mars Polar Science and Exploration abstract, University of Iceland, Reykjavik

Kieffer, H. H., Titus, T. N., Mullins, F., Christensen, P. R., 2000. Mars south polar spring and summer behavior observed by TES: seasonal cap evolution controlled by frost grain size. Journal of Geophysical Research 105 (E4), 9653–9699

Kieffer, H. H., Titus, T. N., 2001. TES mapping of Mars' north seasonal cap. Icarus 154 (1), 162–180

Kieffer, H. H., Christensen, P. R., Titus, T. N., 2006. CO_2 jets formed by sublimation beneath translucent slab ice in Mars' seasonal south polar ice cap. Nature 442, 793–796

Kieffer, H. H., 2007. Cold jets in the Martian polar caps. Journal of Geophysical Research 112 (E8), E08005

Koponen, A., Kataja, M., Timonen, J., 1997. Permeability and effective porosity of porous media. Physical Review E 56 (3)

Koutnik, M. R., et al., 2002. South polar layered deposits of Mars: The cratering record. Journal of Geophysical Research 107 (E11), 5100

Kreslavsky, M. A., Head, J. W., 2002. Mars: Nature and evolution of young latitude–dependent water–ice–rich mantle. Geophysical Research Letters 29, 1719

Kreslavsky, M. A., Head, J. W., 2009. Slope streaks on Mars: A new "wet" mechanism. Icarus 201 (2), 517–527

Kelly, N. J., Boynton, W. V., Kerry, K., Hamara, D., Janes, D., Reedy, R. C., Kim, K. J., Haberle, R. M., 2006. Seasonal polar carbon dioxide frost on Mars: CO_2 mass and columnar thickness distribution. Journal of Geophysical Research 111, E03S07

Kneissl, T., van Gasselt, S., Neukum, G., 2011. Map–projection–independent crater size–frequency determination in GIS environments–New software tool for ArcGIS. Planetary and Space Science 59 (11–12), 1243–1254

Kress, A. M., Head, J. W., 2015. Late Noachian and early Hesperian ridge systems in the south circumpolar dora argentea Formation, Mars: Evidence for two stages of melting of an extensive late Noachian ice sheet. Planetary and Space Science 109–110, 1–20

Kerber, L., Dickson, J. L., Head, J. W., Grosfils, E. B., 2017. Polygonal ridge networks on mars: diversity of morphologies and the special case of the eastern medusae fossae formation. Icarus 281, 200–219

Kaufmann, E., Hagermann, A., 2017. Experimental investigation of insolation–driven dust ejection from Mars' CO2 ice caps. Icarus 282, 118–126

Leighton, R. B., Murray, B. C., 1966. Behavior of carbon dioxide and other volatiles on Mars. Science 153, 136–144

Larson, H. P., Fink, U., 1972. Identification of carbon dioxide frost on the Martian polar caps. Astronomical Journal 171, L91

Leovy, C., 2001. Weather and climate on Mars. Nature 412, 245–249

Laskar, J., Levrard, B., Mustard, J. F., 2002. Orbital forcing of the Martian polar layered deposits. Nature 419, 375–377

Langevin, Y., and the others 2005. Summer evolution of the north polar cap of Mars as observed by OMEGA/Mars Express. Science 307, 1581–1584

Langevin, Y., Doute ´, S., Vincendon, M., Poulet, F., Bibring, J., Gondet, B., Schmitt, B., Forget., F., 2006. No signature of clear CO_2 ice from the ''cryptic'' regions in Mars' south seasonal polar cap. Nature 442, 790–792

Langevin, Y., Bibring, J.–P., Montmessin, F., Forget F., Vincendon, M., Doute´ S., Poulet, F., Gondet, B., 2007. Observations of the south seasonal cap of Mars during recession in 2004–2006 by the OMEGA visible/near–infrared imaging spectrometer on board Mars Express. Journal of Geophysical Research 112 (E08S12)

Levy, J., Head, J., Marchant, D., 2009. Thermal contraction crack polygons on Mars: Classification, distribution, and climate implications from HiRISE observations. Journal of Geophysical Research 114

Levy, J., Marchant, D., Head, J., 2010. Thermal contraction crack polygons on Mars: A synthesis from HiRISE, Phoenix, and terrestrial analog studies. Icarus 206, 229–252.

Levrard B., Forget F., Montmessin F., Laskar J., 2007. Recent formation and evolution of northern Martian polar layered deposits as inferred from a global climate model. Journal of Geophysical Research 112, E06012

Limaye, A. B. S., Aharonson, O., Perron, J. T., 2012. Detailed stratigraphy and bed thickness of the Mars north and south polar layered deposits. Journal of Geophysical Research 117 (E06009)

Leyrat, C., Lorenz, R. D., Le Gall., A., 2016. Probing Pluto's underworld: Ice temperatures from microwave radiometry decoupled from surface conditions. Icarus 268, 50–55

Muskat, M., 1937. The flow of fluids through porous media, Journal of Applied Physics 8, 274

Moroz, V. I., 1964. The infrared spectrum of Mars (λ 1.1–4.1μ). Journal of Sound and Vibration 8, 273–281

Masch, F. D., Denny, K. J., 1966. Grain size distribution and its effect on the permeability of unconsolidated sands. Water Resources Research 2 (4), 665–677

Murray, B. C., Soderblom, L. A., Cutts, J. A., Sharp, R. P., Milton, D. J., Leighton, R. B., 1972. Geological framework of the south polar layered region of Mars. Icarus 17, 328–345

Murray, B. C., Ward W. R., Yeung S. C., 1973. Periodic insolation variations on Mars. Science 180 (4086), 638–640

Mellon, M. T., Jakosky, B. M., 1993. Geographic variations in the thermal and diffusive stability of ground ice on Mars. Journal of Geophysical Research 98 (E2), 3345–3364

Mellon, M. T., Jakosky, B. M., 1995. The distribution and behavior of Martian ground ice during past and present epochs. Journal of Geophysical Research 100, 11781–11799

Mellon, M. T., Jakosky, B. M., Postawko, S. E., 1997. The persistence of equatorial ground ice on Mars. Journal of Geophysical Research 102 (E8), 19357–19369

Mellon, M. T., Phillips, R. J., 2001. Recent gullies on Mars and the source of liquid water. Journal of Geophysical Research 106 (E10), 23165–23180.

Mellon, M. T., Feldman, W. C., Prettyman, T. H., 2004. The presence and stability of ground ice in the southern hemisphere of Mars. Icarus 169, 324–340

Martin, T. Z., 1995. Mass of dust in the Martian atmosphere, Journal of Geophysical Research 100 (E4), 7509–7512

Malin, M. C., and the others, 1998. Early views on the Martian surface from the Mars orbiter camera of mars global surveyor. Science 279 (5357), 1681–1685

Malin, M. C., Edgett, K, S., 2000. Evidence for recent groundwater seepage and surface runoff on Mars. Science 288, 5475

Malin, M. C., Edgett, K. S., 2001. Mars Global Surveyor Mars orbiter camera: Interplanetary cruise through primary mission. Journal of Geophysical Research 106, 23429–23570

Malin, M. C., Edgett, K. S., Posiolova, L. V., McColley, S. M., Noe Dobrea, E. Z., 2006. Present–day impact cratering rate and contemporary gully activity on Mars. Science 314, 1573–1577

Malin, M. C. et al., 2007. Context Camera Investigation on board the Mars Reconnaissance Orbiter. Journal of Geophysical Research 112, E05S04

Mitrofanov, I., Anfimov, D., Kozyrev, A., Litvak, M., Sanin, A., Tret'yakov, V., Krylov, A., Shvetsov, V., Boynton, W., Shinohara, C., Hamara, D., Saunders, R. S., 2002. Maps of subsurface hydrogen from the high energy neutron detector, Mars Odyssey. Science 297 (5578), 78–81

Mitrofanov, I., Litvak, M. L., Kozyrev, A. S., Sanin, A., Tret'yakov, V. I., Grin'kov, V., Boynton, W., Shinohara, C., Hamara, D., Saunders, R. S., 2004. Soil Water Content on Mars as Estimated from Neutron Measurements by the HEND Instrument Onboard the 2001 Mars Odyssey Spacecraft. Solar system research, 38 (4), 253–265

Mangold, N., Forget, F., Peulvast, J.–P., 2002. Narrow gullies over high sand dunes on Mars: Evidence for recent liquid flows. EGU General Assembly Conference Abstract 27, 3080

Mischna, M. A., Richardson, M. I., Wilson, R. J., McCleese, D. J., 2003. On the orbital forcing of Martian water and CO_2 cycles: A general circulation model study with simplified volatile schemes. Journal of Geophysical Research 108 (E6).

Miyamoto, H., Dohm, J. M., Beyer, R. A., Baker, V. R., 2004. Fluid dynamical implications of anastomosing slope streaks on Mars. Journal of Geophysical Research 109, E06008

Montmessin, F., Forget, F., Rannou, P., Cabane, M., Haberle, R. M., 2004. Origin and role of water ice clouds in the Martian water cycle as inferred from a general circulation model. Journal of Geophysical Research (Planets) 109, E10004

McEwen, A. S., and 13 colleagues, 2007. MRO's High Resolution Imaging Science Experiment (HiRISE). Journal of Geophysical Research 112

McEwen, A. S., and 69 colleagues, 2010. The High Resolution Imaging Science Experiment (HiRISE) during MRO's primary science phase (PSP). Icarus 205, 2–37

McEwen, A. S., Ojha, L., Dundas, C. M., Mattson, S. S., Byrne, S., Wray, J., Cull, S. C., Murchie, S. L., Thomas, N., Gulick, V. C., 2011. Science 333, 740–744

McEwen, A. S., Dundas, C. M., Mattson, S. S., Toigo, A. D., Ojha, L., Wray, J., Chojnacki, M., Byrne, S., Murchie, S. L., Thomas, N., 2014. Nature Geoscience 7, 53–58

Milkovich S. M., Plaut J.J., 2008. Martian south polar layered deposit stratigraphy and implications for accumulation history. Journal of Geophysical Research 113 (2008), E06007

Madeleine, J. B., Forget, F., Head, J. W., Levrard, B., Montmesin, F., Millour, E., 2009. Amazonian northern mid–latitude glaciation on Mars: a proposed climate scenario. Icarus 203, 390–405

Michael, G., Platz, T., Kneissl, T., Schmedemann, N., 2012. Planetary surface dating from crater size–frequency distribution measurements: spatial randomness and clustering. Icarus 218, 169–177

Mahaffy, P. R., and the others, 2013. Abundance and Isotopic Composition of Gases in the Martian Atmosphere from the Curiosity Rover. Science 341 (6143), 263–266

Martín–Torres, F. J., and the others, 2015. Transient liquid water and water activity at Gale crater on Mars. Nature geoscience 8, 357–361

Miyan, M., Pant, P., 2015. Flow and Diffusion Equations for Fluid Flow in Porous Rocks for the Multiphase Flow Phenomena. AJER 4 (7), 139–148

Muller, J. P., Tao, Y., Sidiropoulos, S., Gwinner, K., Willner, K., Fanara, L., Waehlisch, M., van Gasselt, S., Walter, S., Steikert, R., Schreiner, B., Ivanov, A., Cantini, F., Wardlaw, J., Morley, J., Sprinks, J., Giordano, M., Marsh, S., Kim, J., Houghton, R., Bamford, S., 2016. EU–FP7–iMARS: analysis of Mars multi–resolution images using auto–coregistration, data mining and crowd source techniques: processed results – a first look. XXIII ISPRS Congress XLI–B4. doi:10.5194/isprsarchives–XLI–B4–453–2016

Mc Keown, L. E., Bourke, M. C., McElwaine, J. N., 2017. Experiments on sublimating carbon dioxide ice and implications for contemporary surface processes on Mars. Scientific reports 7, 14181

Neugebauer, M. G., Kieffer, H. H., Chase, S. C., Miner, E., 1971. Mariner 1969 infrared results: Temperatures and thermal properties. Astronomical Journal 76, 719

Nolin, A., Dozier, J., 2000. A hyperspectral method for remotely sensing the grain size of snow. Remote Sensing of Environment 74, 207–216

Nye, J. F., Durham, W. B., Schenk, P. M., and Moore, J. M., 2000. The instability of a south polar cap on Mars composed of carbon dioxide. Icarus 144, 449–455

Neukum, G., Jaumann, R., the HRSC Team, 2004. HRSC: The High Resolution Stereo Camera of Mars Express. European Space Agency Special Publication 1240, 17–35

Nerozzi, S., Holt, J. W., 2019. Buried ice and sand caps at the north pole of Mars: revealing a record of climate change in the cavi unit with SHARAD. Geophysical Research Letters 46

Ness, P. K., Orme, G. M., 2002. Spider–Ravine Models and Plant–like Features on Mars – Possible Geophysical and Biogeophysical Modes of Origin. Journal of the British Interplanetary Society 55, 85–108

Ohja, L., Wilhelm, M. B., Murchie, S. L., McEwen A. S., Wray, J. J., Hanley, J., Massé, M., Chojnacki, M., 2015. Spectral evidence for hydrated salts in recurring slope lineae on Mars. Nature geoscience 8, 829–832

Ogolo, N. A., Akinboro, O. G., Inam, J. E., Akpokere, F. E., Onyekonwu, M. O., 2015. Effect of Grain Size on Porosity Revisited. Society of Petroleum Engineers

Orosei, R., et al., 2018. Radar evidence of subglacial liquid water on Mars. Science 361 (6401), 490–493.

Paige, D. A., Ingersoll, A. P., 1985. Annual heat balance of the Martian polar caps: Viking observations. Science 228, 1160–1168. doi:10.1126/science.228.4704.1160

Paige, D. A., Herkenhoff, K., Murray, B., 1990. Mariner 9 observations of the south polar cap of Mars: Evidence for residual CO_2 frost. Journal of Geophysical Research 95, 1319–1335

Paige, D. A., Keegan, K. D., 1995. Thermal and albedo mapping of the polar regions of Mars using Viking Thermal Mapper observations. 2 South Polar Region. Journal of Geophysical Research 99, 25993–26013

Pimentel, G. C., Forney, P. B., Herr, K. C., 1974. Evidence about hydrate and solid water in the Martian surface from the 1969 Mariner infrared spectrometer. Journal of Geophysical Research 79, 1623–1634

Presley, M. A., Christensen, P. R., 1997. Thermal conductivity measurements of particulate materials: 2. Results, Journal of Geophysical Research 102, 6551–6566

Presley, M. A., Christensen, P. R., 2010. Thermal conductivity measurements of particulate materials: 4. Effect of bulk density for granular particles. Journal of Geophysical Research 115 (E7)

Piqueux, S., Bryne, S., Richardson, M. I., 2003. Sublimation of Mars's southern seasonal CO_2 ice cap and the formation of spiders. Journal of Geophysical Research 108 (E8), 5084

Piqueux, S., Christensen, P. R., 2008. North and south subice gas flow and venting of the seasonal caps of Mars: A major geomorphological agent. Journal of Geophysical Research 113 (E6), E06005

Piqueux, S., Edwards, C. S., Christensen, P. R., 2008. Distribution of the ices exposed near the south pole of Mars using Thermal Emission Imaging System (THEMIS) temperature measurements. Journal of Geophysical Research 113, E08014

Piqueux, S., Christensen, P. R., 2009. A model of thermal conductivity for planetary soils: 1. Theory for unconsolidated soils. Journal of Geophysical Research 114, E09005

Piqueux, S., Kleinböhl, A., Hayne, P. O., Kass, D. M., Schofield, J. T., McCleese, D. J., 2015. Variability of the Martian seasonal CO_2 cap extent over eight Mars Years. Icarus 251, 164–180

Piqueux, S., Kleinböhl, A., Hayne, P. O., Heavens, N. G., Kass, D. M., McCleese, D. J., Schofield, J. T., Shirley, J. H., 2016. Discovery of a widespread low–latitude diurnal CO_2 frost cycle on Mars. Journal of Geophysical Research (Planets) 121, 1174–1189

Prettyman, T. H., Feldman, W. C., Barraclough, B. L., Capria, M. T., Coradini, A., Enemark, D. C., Fuller, K. R., Lawrence, D. J., Patrick, D. E., Raymond, C. A., Storms, S. A., and Williford, R. L., 2004. Mapping the elemental composition of Ceres and Vesta: Dawn's gamma ray and neutron detector. Proc. SPIE 5660, Instruments, Science, and Methods for Geospace and Planetary Remote Sensing

Picardi, G., and the others, 2005. Radar soundings of the subsurface of Mars. Science 310, 1925–28

Putzig, N. E., Mellon, M. T., Kretke, K. A., Arvidson, R. E., 2005. Global thermal inertia and surface properties of Mars from the MGS mapping mission. Icarus 173, 325–341

Putzig, N. E., Mellon, M. T., 2007. Apparent thermal inertia and the surface heterogeneity of Mars. Icarus 191, 68–94

Plaut, J. J., and the others, 2007. Radar Sounding of Subsurface Layers in the South Polar Plains of Mars: Correlation with the Dorsa Argentea Formation. 38th Lunar and Planetary Sciences Conference 38th, abstract 2144

Portyankina, G., Markiewicz, W. J., Thomas, N., Hansen, C. J., Milazzo, M., 2010. HiRISE observations of gas sublimation–driven activity in Mars southern polar regions: III. Models of processes involving translucent ice. Icarus 205, 311–320

Portyankina, G., Pommerol, A., Aye, K.–M., Hansen, C. J., Thomas, N., 2012. Polygonal cracks in the seasonal semi–translucent CO_2 ice layer in Martian polar areas. Journal of Geophysical Research 117, E02006

Portyankina, G., Pommerol, A., Aye, K.–M., Thomas, N., Mattson, S., Hansen, C. J., 2013. Influence of small scale topography on early spring activity in Martian polar areas. An example study based on DEM of Inca City region. 2013 European Planetary Science Congress Abstract 2013–410

Portyankina, G., Hansen, C., Aye, K., 2017. Present–day erosion of Martian polar terrain by the seasonal CO_2 jets. Icarus 282, 93–103

Portyankina, G., Merrison, J., Iversen, J., Yoldi, Z., Hansen, C. J., Aye, K.–M., Pommerol, A., Thomas, N., 2018. Laboratory investigations of the physical state of CO_2 ice in a simulated Martian environment. Icarus 322, 210–220

Portyankina, G., Aye, K.–M., 2018. Chapter 6–CO_2–driven geomorphological processes: landscape evolution. Dynamic Mars. Elsevier

Portyankina, G., Hansen, C. J., Aye, K.–M., 2019. How Martian araneiforms get their shapes: Morphological analysis and diffusion–limited aggregation model for polar surface erosion. Icarus

Pommerol, A., Portyankina, G., Thomas, N., Aye, K.–M., Hansen, C. J., Vincendon, M., Langevin, Y., 2011. Evolution of south seasonal cap during Martian spring: Insights from high–resolution observations by HiRISE and CRISM on mars reconnaissance orbiter. Journal of Geophysical Research (Planets) 116 (E8), 0148–0227

Pommerol, A., Thomas, N., Jost, B., Beck, P., Okubo, C., McEwen, A., 2013. Photometric properties of Mars soils analogs. Journal of Geophysical Research: Planets 118

Phillips, R. J., et al., 2011. Massive CO_2 ice deposits sequestered in the south polar layered deposits of Mars. Science 332 (6031), 838–41

Pilorget, C., Forget, F., Millour, E., Vincendon, M., Madeleine, J. B., 2011. Dark spots and cold jets in the polar regions of Mars: New clues from a thermal model of surface CO_2 ice. Icarus 213 (1), 131–149

Pilorget, C., Forget, F., 2015. Formation of gullies on Mars by debris flows triggered by CO_2 sublimation. Nature Geoscience 9 (1), 65–69

Pottier, A., Forget, F., Montmessin, F., Navarro, T., Spiga, A., Millour, E., Szantai, A., Madeleine J., 2017. Unraveling the Martian water cycle with high–resolution global climate simulations. Icarus 291, 82–106

Pathare, A. V., Feldman, W. C., Prettyman, T. H., 2018. Maurice, S., Driven by Excess? Climatic Implications of New Global Mapping of Near–Surface Water–Equivalent Hydrogen on Mars. Icarus 301, 97–116

Richardson, M. I., Wilson, R. J., 2002. A topographically forced asymmetry in the Martian circulation and climate. Nature 416 (6878), 298–301

Scheidegger, A. E., 1958. The Physics of Flow Through Porous Media. Soil Science 86 (6)

Spinrad, H., Munch G., Kaplan, L. D., 1963. The detection of water vapor of Mars. The Astrophysical Journal 137, 1319–1321

Sharp, R. P., 1973. Mars: Troughed terrain. Journal of Geophysical Research 78 (20), 4063–4072

Shepherd, R. G., 1989. Correlations of Permeability and Grain Size. Groundwater 27, 633–638

Smith, D. E., Zuber, M. T., Frey, H. V., Garvin, J. B., Head, J. W., Muhleman, D. O., Pettengill, G. H., Phillips, R. J., Solomon, S. C., Zwally, H. J., Banerdt, W. B., Duxbury, T. C., 1998. Topography of the northern hemisphere of Mars from the Mars Orbiter Laser Altimeter. Science 279 (5357)

Smith, D. E., et al., 1999. The global topography of mars and implications for surface evolution. Science 284, 1495–1503

Smith, D. E., Zuber, M. T., Neumann, G. A., 2001a. Seasonal variations of snow depth on Mars. Science 294, 2141–2146

Smith, D. E., and the others, 2001b. Mars Orbiter Laser Altimeter–experiment summary after the first year of global mapping of Mars. Journal of Geophysical Research 106 (E10), 23689–23722

Smith, M. D., 2002. The annual cycle of water vapor on Mars as observed by the Thermal Emission Spectrometer. Journal of Geophysical Research 107, 1–19

Schorghofer, N., Aharonson, O., 2005. Stability and exchange of subsurface ice on Mars. Journal of Geophysical Research Planets 110

Schorghofer, N., Edgett, K. S., 2006. Seasonal surface frost at low latitudes on Mars. Icarus 180, 321–334

Spiga, A., Forget, F., 2008. Fast and accurate estimation of solar irradiance on Martian slopes. Geophysical Research Letters 35, L15201

Spiga, A., Forget, F., Madeleine, J. B., Montabone, L., Lewis, S. R., Millour, E., 2011. The impact of martian mesoscale winds on surface temperature and on the determination of thermal inertia. Icarus 212 (2), 504–519

Schmidt, F., Douté, S., Schmitt, B., Vincendon, M., Bibring, J.–P., Langevin, Y., 2009. Albedo control of seasonal south polar cap recession on mars. Icarus 200 (2), 374–394

Smith, I. B., Holt, J. W., Spiga, A., Howard, A. D., Parker, G., 2013. The spiral troughs of Mars as cyclic steps. Journal of Geophysical Research: Planet 118 (9), 1835–1857

Smith, I. B., Spiga, A., Holt, J. W., 2015. Aeolian processes as drivers of landform evolution at the South Pole of Mars. Geomorphology 240, 54–69

Smith, D. E., Zuber, M. T., 2018. Depth, volume and density of Mars' seasonal polar caps. 2018 EPSC, abstract No. EPSC2018–429

Sullivan, R., R. Anderson, J. Biesiadecki, T., Bond, Stewart, H., 2011. Cohesions, friction angles, and other physical properties of Martian regolith from Mars Exploration Rover wheel trenches and wheel scuffs. Journal of Geophysical Research 116, E02006

Schwamb M. E. et al., 2017. Planet Four: Terrains – Discovery of araneiforms outside of the South Polar layered deposits. Icarus 308, 148–18

Smith, D. E., Zuber, M. T., 2018. Depth, volume and density of Mars' seasonal polar caps. 2018 EPSC, abstract No. EPSC2018–429

Shaposhnikov, D. S., Medvedev, A. S., Rodin, A. V. V., & Hartogh, P., 2019. Seasonal water "pump" in the atmosphere of mars: Vertical transport to the thermosphere. Geophysical Research Letters 46, 4161–4169

Sutton, J. L., Leovy, C. B., Tillman, J. E., 1978. Diurnal variations of the martian surface layer meteorological parameters during the first 45 sols at two Viking lander sites. Journal of the Atmospheric Sciences 35, 2346–2355

Toon, O. B., Pollack J. B., Ward W., Burns J. A., Bilski K., 1980. The astronomical theory of climatic change on Mars. Icarus 44 (3), 552–607

Tillman, J. E., Johnson N. C., Guttorp P., Percival D. B., 1993. The Martian annual atmospheric pressure cycle: Years without great dust storms. Journal of Geophysical Research 98, 10963–10971

Tanaka, K. L., Kolb, E. J., 2001. Geologic history of the polar regions of Mars based on mars global surveyor data. I. Noachian and Hesperian Periods. Icarus 154, 3–21

Tanaka, K. L., Skinner, J. A., Jr., Dohm, J. M., Irwin, R. P., III, Kolb, E. J., Fortezzo, C. M., Platz, T., Michael, G., Hare, T. M., 2014, Geologic map of Mars: U.S. Geological Survey Scientific Investigations Map 3292, scale 1:20,000,000, pamphlet 43

Tokar, R. L., Feldman, W. C., Prettyman, T. H., Moore, K. R., Lawrence, D. J., Elphic, R. C., Kreslavsky, M. A., Head III, J. W., Mustard, J. F., Boynton, W. V., 2002. Ice concentration and distribution near the south pole of Mars: Synthesis of Odyssey and Global Surveyor analyses. Geophysical Research Letters 29, 1904

Thomas, P. C., Squyres, S., Herkenhoff, K., Howard, A., Murray, B., 1992. Polar deposits of Mars, edited by H. H. Kieffer et al., in Mars, pp. 767–798, Univ. of Arizona Press, Tucson, Ariz

Thomas, P. C., et al., 2000. North–south geological differences between the residual polar caps on Mars. Nature 404, 161–164

Thomas, P. C., Malin, M. C., James, P. B., et al., 2005. South polar residual cap of Mars: features, stratigraphy, and changes. Icarus 174, 535–559

Thomas, P. C., James, P. B., Calvin, W. M., Haberle R., Malin, M. C., 2009. Residual south polar cap of Mars: Stratigraphy, history, and implications of recent changes. Icarus 203, 352

Thomas, P. C., Calvin, W. M., Gierasch, P., Haberle, R., James, P. B., Sholes, S., 2013. Time scales of erosion and deposition recorded in the residual south polar cap of mars. Icarus 225 (2), 923–932

Thomas, P. C., Calvin, W., Cantor, B., Haberle, R., James, P. B., Lee, S. W., 2016. Mass balance of Mars' residual south polar cap from CTX images and other data. Icarus 268, 118–130

Titus, T. N., Kieffer, H. H., Mullins, K. F., 2001. Slab ice and snow flurries in the Martian polar night. Journal of Geophysical Research 106 (E10), 23181–23196

Titus, T. N., Kieffer, H. H., and Christensen, P. R., 2003. Exposed water ice discovered near the south pole of Mars. Science 299, 1048–1050

Titus, T. N., Calvin, W. M., Kieffer, H. H., Langevin, Y., Prettyman, T. H., 2008. Martian Polar Processes in the Martian Surface: Composition, Mineralogy, and Physical Properties, edited by J. F. Bell, Cambridge University Press, New York, 578–598

Thomas, N., Hansen, C. J., Portyankina, G., Russell, P. S., 2010. HiRISE observations of gas sublimation–driven activity in Mars' southern polar regions: II. Surficial deposits and their origins. Icarus 205 (1), 296–310

Thomas, N, Portyankina, G., Hansen, C. J., Pommerol, A., 2011a. HiRISE observations of gas sublimation–driven activity in Mars' southern polar regions: IV. Fluid dynamics models of CO_2 jets. Icarus 212, 66–85

Thomas, N, Portyankina, G., Hansen, C. J., Pommerol, A., 2011b. Subsurface CO_2 gas flow in Mars' polar regions: Gas transport under constant production rate conditions. Geophysical Research Letters 38 (8), L08203

Thomas N., et al., 2017. The Colour and Stereo Surface Imaging System (CaSSIS) for the ExoMars Trace Gas Orbiter. Space Science Reviews 212, 1897–1944

Tao, Y., Muller, J. P., 2016. Quantitative assessment of a novel super–resolution restoration technique using HiRISE with Navcam images: how much resolution enhancement is possible from repeat–pass observations. XXIII ISPRS Congress XLI–B4

van Gasselt, S., Reiss, D., Thorpe, A. K., Neukum, G., 2005. Seasonal Variations of Polygonal Thermal Contraction Crack Patterns in a South Polar Trough, Mars. Journal of Geophysical Research (Planets) 110, 8002

Vago, J., Witasse, O., Svedhem, H., Baglioni, P., Haldemann, A., Gianfiglio, G., Blancquaert, T., McCoy, D., de Groot, R., 2015. ESA ExoMars program: The next step in exploring Mars. Solar System Research 49, 518–528

Ward, W. R., 1973. Large–Scale Variations in the Obliquity of Mars. Science 181 (4096), 260–262

Wood, S. E., 1999. Nucleation and growth of CO_2 ice crystals in the Martian atmosphere, Ph.D. thesis, University of Calif. Los Angeles, Los Angeles

Whelley, P. L., Greeley, R., 2008. The distribution of dust devil activity on Mars. Journal of Geophysical Research Atmospheres 113 (E7)

Zimbelman, J. R., 1986. The role of porosity in thermal inertia variations on basaltic lavas. Icarus 68, 366–369

Zuber, M. T., and the others, 1998. Observations of the north polar region of Mars from the Mars Orbiter Laser Altimeter. Science 282, 2053–2060

Supplementary material

Table S1 HiRISE images used in this thesis

Regions	Image ID	Ls*	MY*	Incidence Angle (°)
A (Angustus Labyrinthus)	PSP_002380_0985	174	28	89.9
	PSP_002868_0985	196	28	81.3
	PSP_003092_0985	206	28	76.4
	PSP_003158_0985	209	28	75.5
	PSP_003237_0985	213	28	73.5
	PSP_003448_0985	223	28	70.0
	PSP_003593_0985	230	28	67.5
	PSP_003770_0815	239	28	75.4
	PSP_003804_0985	241	28	64.6
	PSP_003928_0815	247	28	74.4
	PSP_004081_0985	254	28	62.2
	PSP_004371_0985	269	28	60.3
	PSP_004714_0985	285	28	61.4
	PSP_004925_0985	295	28	62.8
	PSP_005070_0985	302	28	64.0
	PSP_005281_0985	312	28	66.5
	PSP_005426_0985	318	28	68.4
	PSP_005993_0985	342	28	77.5
	ESP_011491_0985	187	29	84.2
	ESP_011544_0985	189	29	84.2
	ESP_011557_0985	190	29	83.3
	ESP_011623_0985	193	29	82.3
	ESP_011702_0985	197	29	80.3
	ESP_011728_0985	198	29	78.4
	ESP_011729_0985	198	29	82.3
	ESP_011900_0985	206	29	77.4
	ESP_012256_0985	223	29	70.9
	ESP_012322_0985	226	29	70.2
	ESP_012467_0985	233	29	67.7
	ESP_012691_0985	244	29	64.2
	ESP_012744_0985	247	29	64.6
	ESP_012889_0985	254	29	63.1
	ESP_013034_0985	261	29	61.8
	ESP_013113_0985	265	29	61.0
	ESP_013601_0985	289	29	62.1
	ESP_013759_0985	296	29	62.5
	ESP_013812_0985	299	29	63.8
	PSP_006204_0985	351	29	81.2
	ESP_020049_0985	176	30	89.0
	ESP_020115_0985	179	30	88.1
	ESP_020128_0985	179	30	87.1
	ESP_020194_0985	182	30	86.1
	ESP_020339_0985	188	30	83.4
	ESP_020748_0985	207	30	76.5
	ESP_020827_0985	211	30	74.6
	ESP_020959_0985	217	30	72.7
	ESP_021460_0985	242	30	65.0
	ESP_021526_0985	245	30	64.5
	ESP_021605_0985	249	30	63.3
	ESP_021671_0985	253	30	63.0
	ESP_021684_0985	253	30	62.2

	ESP_021829_0985	260	30	61.0
	ESP_022027_0985	270	30	60.9
	ESP_022607_0985	298	30	62.5
	ESP_022699_0985	302	30	62.5
	ESP_023385_0985	332	30	73.0
	ESP_028752_0985	171	31	90.6
	ESP_028884_0985	176	31	88.8
	ESP_028910_0985	178	31	86.9
	ESP_028911_0985	178	31	90.8
	ESP_029095_0985	186	31	85.0
	ESP_029108_0985	186	31	84.1
	ESP_029227_0985	192	31	83.0
	ESP_029240_0985	192	31	82.0
	ESP_029596_0985	209	31	75.3
	ESP_029662_0985	212	31	74.5
	ESP_029741_0985	216	31	72.6
	ESP_029807_0985	219	31	71.7
	ESP_029886_0985	223	31	69.9
	ESP_030084_0985	232	31	67.6
	ESP_030163_0985	236	31	66.2
	ESP_030229_0985	240	31	65.5
	ESP_031020_0985	278	31	60.4
	ESP_031086_0985	282	31	60.9
	ESP_032009_0985	324	31	70.3
	ESP_032352_0985	339	31	76.4
	ESP_032444_0985	343	31	77.0
	ESP_037626_0985	173	32	89.2
	ESP_037811_0985	181	32	87.3
	ESP_037877_0985	184	32	86.2
	ESP_037956_0985	188	32	84.3
	ESP_038022_0985	191	32	83.3
	ESP_038154_0985	197	32	81.3
	ESP_038299_0985	203	32	78.2
	ESP_038444_0985	210	32	75.1
	ESP_038510_0985	213	32	74.0
	ESP_038972_0985	236	32	67.4
	ESP_039275_0985	251	32	62.9
	ESP_039407_0985	257	32	62.3
	ESP_039473_0985	261	32	62.3
	ESP_039552_0985	265	32	61.4
	ESP_039565_0985	265	32	60.7
	ESP_039631_0985	268	32	60.7
	ESP_039684_0985	271	32	61.6
	ESP_039763_0985	275	32	61.0
	ESP_039776_0985	276	32	60.4
	ESP_040185_0985	295	32	63.0
	ESP_041016_0985	332	32	73.8
	ESP_041029_0985	333	32	74.3
	ESP_041121_0985	337	32	74.8
B	PSP_005993_0985	342	28	78.0
C	ESP_014123_0930	313	29	72.0
D	ESP_014413_0930	326	29	75.0
E	ESP_013964_0935	306	29	68.0
F	ESP_032597_0940	349	31	84.0
G	PSP_005553_0980	324	28	72.0
Others	PSP_005627_1015	327	28	69.0
	ESP_013277_1070	273	29	56.0

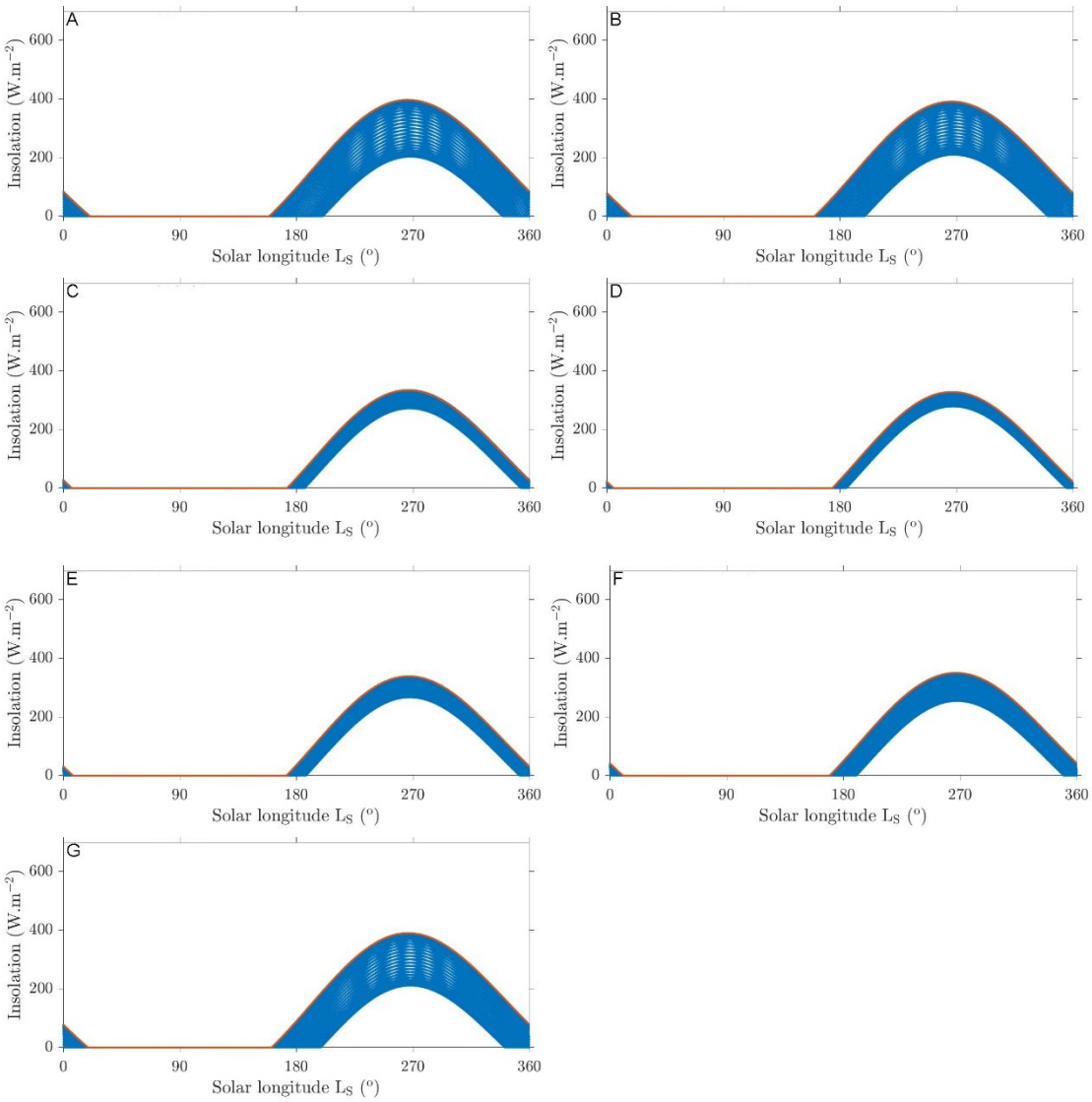

Figure S1 Insolation of regions from A to G for one Mars year (Ls from 0° to 360°). Note that blue "lines" are discrete points indicating 33450 values from iterations. Red line indicates the maximum insolation of each day.

Publications (the latest five years)

J. Hao, G. Michael, S. Adeli, R. Jaumann, 2019. Araneiform terrain formation in Angustus Labyrinthus, Mars. Icarus 317, 479–490. doi:org/10.1016/j.icarus.2018.07.026

J. Hao, G. Michael, S. Adeli, R. Jaumann, G. Portyankina, E. Hauber, C. Millot, W. Zuschneid. Variability of spider spatial configuration at the Martian south pole. Accepted at Planetary and Space Science. doi:org/10.1016/j.pss.2020.104848

J. Hao, G. Michael, S. Adeli, R. Jaumann, 2019. Survey of sublimation Landforms at the South Pole of Mars–A Case Study of Angustus Labyrinthus. Lunar and Planetary Science Conference (LPSC). Abstract 1401

J. Hao, G. Michael, S. Adeli, G. Portyankina, E. Hauber, C. Millot, W. Zuschneid, R. Jaumann, 2019. Variability of araneiform spatial patterns at the Martian south pole (***Oral***). LPSC. LPI Contrib. No. 2132

J. Hao, G. Michael, S. Adeli, R. Jaumann, 2018. An Investigation of Araneiform Terrain in Angustus Labyrinthus, Mars (***Oral***). European Planetary Science Congress (EPSC). Abstract EPSC2018–1019

J. Hao, G. Michael, S. Adeli, R. Jaumann, 2017. Araneiform terrain in the south pole of Mars–its formation mechanism and spatial pattern. Mars Express (MEx)/HRSC annual meeting (***Oral***)

J. Hao, S. Adeli, G. Michael, G. Portyankina, R. Jaumann, 2018. Investigation of regional settings for formation of Araneiform Terrain, Mars. EPSC (***Oral***). Abstract EPSC2018–929

J. Hao, G. Michael, R. Jaumann, S. Adeli, 2018. Araneiform terrain formation in Angustus Labyrinthus, Mars. European Geosciences Union (EGU) (***Oral***). Abstract 16624

J. Hao, G. Michael, S. van Gasselt, R. Jaumann, 2017. An Integrated study of Mars Polar Processes and Landforms–Seasonal activities in Inca City. MEx/HRSC annual meeting (***Oral***)

J. Hao, G. Michael, S. van Gasselt, R. Jaumann, J. Lanz–Kröchert, 2017. Analysis of Spiders in Inca city: Spatial Distribution and Types. LPSC. Abstract 1712

J. Hao, G. Michael, R. Jaumann, S. Adeli, 2017. Observations of south polar landforms, Mars: a case study in Angustus Labyrinthus. EPSC. Abstract EPSC2017–224

J. Hao, S. van Gasselt, A. Neesemann, 2016. Observations of seasonal variability of landforms in the Martian South Polar region. 6th International Conference on Mars Polar Science and Exploration. Abstract 6107

J. Hao, S. van Gasselt, G. Michael, 2016. HiRISE observations of Spiders in South Polar regions–A case study in Inca City. SFB TRR 170 Integrated Research Training Program Late Accretion onto Terrestrial Planets (abstract).

J. Hao, S. van Gasselt, A. Neesemann, 2016. An Integrated study of Seasonal Changes of Martian South Polar Landforms–A Case Study in Angustus Labyrinthus. EPSC. Abstract 2566185

J. Hao, S. van Gasselt, 2016. A Systematic Survey of Transient Landforms at the South Pole of Mars–A Case Study of the Cavi Angusti Area. Asia Oceania Geosciences Society (AOGS). Abstract PS02–D5–PM2–P–009

J. Hao, S. van Gasselt, 2016. Observation and Assessment of Seasonal Change, Cavi Angusti, Mars. EGU. Abstract 9681

S. van Gasselt, **J. Hao**, 2015. Systematic High–Resolution Remote–Sensing Investigation of Martian South Polar Landforms: Thermal Contraction Polygons. EGU. Abstract 2015–7819–2.